

UNIVERSITY of CALIFORNIA
Santa Barbara

Observations and Theory of Pulsating Helium White Dwarfs

A dissertation submitted in partial satisfaction of the
requirements for the degree of

Doctor of Philosophy

in

Physics

by

Justin D. Steinfeldt

Committee in charge:

Professor Lars Bildsten, Chair
Professor Tim Brown
Professor Omer Blaes

March 2011

The dissertation of Justin D. Steinfadt is approved:

Professor Omer Blaes

Professor Tim Brown

Professor Lars Bildsten, Chair

University of California, Santa Barbara

March 2011

Observations and Theory of Pulsating Helium White Dwarfs

Copyright 2011

by

Justin D. Steinfadt

Acknowledgments

First, I must thank my advisor, Lars Bildsten, without whom this dissertation and research would have been impossible. I thank him for shaping my development as a scientist and teaching me how to think as one. He has been generous, patient, and always seemed to know when to bring me back on track or prod me in the right direction. He is a better advisor than I ever thought possible. Here at the end, I must thank him for the endless number of real world contacts that have increased my job prospects infinitely.

At UCSB, the astro group has been incredibly supportive and friendly. I always looked forward to Astro Tea and will look fondly on these unique gatherings. I thank all of the faculty as both teachers and mentors, including Omer Blaes for serving on my committee and joining many of the postdocs and grad students for numerous lunches, and also Tim Brown for serving on my committee and accepting every director's discretionary time proposal I ever submitted to LCOGT providing many of the telescope resources used in this dissertation and my research. Many of the postdocs have in their time here been both friends and colleagues to me: special thanks to Avi, David, Dawn, Eli, Marusa, Matt, Matt, Phil, Randy, Sebastian, and Vardha. My office-mates, Anna, Ken H, Ken S, Kevin, and Michael, receive special thanks for creating an environment that made me want to come in to the office every day.

My research was helped in large part by my collaborations with David Kaplan,

Steve Howell, and Phil Arras. Bill Paxton provided MESA and Tioga, integral components to my research.

My friends here in Santa Barbara have made my time as a grad student the best time of my life. I must thank my housemates, Anthony, James, Jeremy, Matt, and Ted who along with Jen and Nammon provided many memorable adventures. When I was not doing research, it was a good bet that I was dancing. Here in Santa Barbara I started competitive ballroom dance and hope I will continue dancing forever. Many have contributed to my absolute enjoyment of this activity and I mention only a few here, Anne, Benedikt, Em, Eric, François, Kat, Kelly, Matt, Marie, Marissa, Max, Michael, Minna, Nancy, Nigel, Ryan, Ryan, Scott, and Susanna. However, perhaps most importantly I thank Ingrid, my girlfriend and dance partner. We have gone from Newcomer to Championship in only three years and without her I do not believe I would have developed the love I have for dancing.

And finally, I thank my family. Without their love and support this dissertation would never exist. They encouraged me to pursue my passions even if they had no idea what I was doing or where I was heading. They made this possible.

Justin D. Steinfadt

March 2011

Curriculum Vitae

Justin D. Steinfadt

Education

- 2011 Ph.D. in Physics, University of California, Santa Barbara
- 2008 M.A. in Physics, University of California, Santa Barbara
- 2005 B.S. in Physics and Astronomy, The University of Arizona

Publications

- “Pulsations in Hydrogen Burning Low-mass Helium White Dwarfs,” **Steinfadt, J. D. R.**, Bildsten, L., & Arras, P. 2010, ApJ, 718, 441
- “Discovery of the Eclipsing Detached Double White Dwarf Binary NLTT 11748,” **Steinfadt, J. D. R.**, Kaplan, D. L., Shporer, A., Bildsten, L., & Howell, S. B. 2010, ApJ, 716, L146
- “Pulsations of the Low-Mass ZZ Ceti Star HS 1824+6000,” **Steinfadt, J. D. R.**, Bildsten, L., Ofek, E., & Kulkarni, S. R. 2008, PASP, 120, 1103
- “Discovery of the Partially Eclipsing White Dwarf Binary SDSS J143547.87+373338.5,” **Steinfadt, J. D. R.**, Bildsten, L., & Howell, S. B. 2008, ApJ, 677, L113
- “A Unique Dust Formation Episode in the SC-Type Star UY Centauri,” **Steinfadt, J. D. R.**, Clayton, G. C. Lloyd Evans, T., & Williams, T.. 2005, PASP, 117, 950

Abstract

Observations and Theory of Pulsating Helium White Dwarfs

by

Justin D. Steinfadt

Average C/O-core white dwarf stars pulsate in observable normal modes of oscillation with amplitudes of a few percent and periods of 100–1,000 seconds. As of this dissertation, no WD of less than $0.5 M_{\odot}$ has been observed to pulsate. White dwarfs of this low mass likely possess a He core and are products of very different stellar evolution. In this dissertation, we have constructed very low mass He-core WD models and predict the parameter space in which they may be observed to pulsate. We have also observed 13 stars, most of which are He-core WDs, in a search for the first He-core WD pulsator. While we were unsuccessful in discovering a pulsator, our detection limits offer unique constraints on He-core WD pulsation parameter space. As a fortuitous result of our pulsation search, we have discovered two unique eclipsing binary systems. One of these is the first eclipsing detached double white dwarf binary system offering the first opportunity to make model independent constraints on He-core WD models and evolution.

Contents

1	Introduction	1
1.1	Formation and Evolution of Helium White Dwarfs	3
1.2	Pulsations	9
2	Pulsations on Helium White Dwarfs	12
2.1	Introduction	13
2.2	Hydrogen Burning Models	16
2.3	Non-Radial Pulsation Analysis	20
2.3.1	WKB Approximation	20
2.3.2	Numerical Analysis	22
2.4	Conclusions	26
3	Pulsation Candidates and Null Detections	29
3.1	Finding Candidates	31
3.2	Observational Strategy	34
3.2.1	Aperture Photometry	36
3.2.2	Periodograms and Detection Limits	39
3.3	Summary of Observations and Results	42
3.3.1	SDSS J0822+2743	44
3.3.2	SDSS J0849+0445	45
3.3.3	SDSS J0917+4638	46
3.3.4	SDSS J1300+5904	48
3.3.5	SDSS J1330+0127	48
3.3.6	SDSS J1435+3733	49
3.3.7	SDSS J1448+0112	51
3.3.8	SDSS J2049+0005	52
3.3.9	SDSS J2240-0935	53
3.3.10	LP 400-22	56
3.3.11	NLTT 11748	58
3.3.12	PSR J1012+5307	58

3.3.13	PSR J1911-5958A	59
4	Observations of a Pulsator	61
4.1	Introduction	62
4.2	Observations	66
4.2.1	Data Reduction	67
4.2.2	Differential Photometry	69
4.3	Lomb-Scargle Timing Analysis	70
4.4	Final Light Curves and Periodograms: Results	73
4.5	Conclusions	79
5	Discoveries of Two Eclipsing Binary Systems	83
5.1	Discovery of the Partially Eclipsing White Dwarf Binary SDSS J143547.87+373338.5	84
5.1.1	Observations and Data Reduction	86
5.1.2	Eclipse Analysis	89
5.1.3	Discussion	95
5.2	Discovery of the Eclipsing Detached Double White Dwarf Binary NLTT 11748	98
5.2.1	Observations	99
Faulkes Telescope North Photometry	102	
Keck Spectroscopy	103	
5.2.2	Binary Parameter Analysis and Results	105
5.2.3	Conclusions	111
6	Conclusions	114
A	Very Low Mass Helium White Dwarf Models:	
	Code Description	119
A.1	Goal	119
A.2	Physics	121
A.2.1	Equations of Stellar Structure	121
A.2.2	Microphysics: Opacity and Equation of State	122
A.2.3	Convection	123
A.2.4	Nuclear Energy Generation	124
A.2.5	Composition Profile	126
Partial Pressure Equations and the Electric Field	127	
Ionic Equation of State	128	
Electron Equation of State	128	
A.3	The Code	134
A.3.1	The Grey Atmosphere	135
A.3.2	Surface toward Core: Outer Layer	137
A.3.3	Surface toward Core: Inner Layer	138

A.3.4	Core toward Surface	139
A.3.5	Iterating to a Solution	139
B	Adiabatic Pulsations	141
B.1	Derivation Framework	141
B.2	The Energy Equation	142
B.2.1	Aside: The Brunt-Väisälä Frequency	144
B.3	Linearized Fluid Equations	147
B.4	Boundary Conditions	150
B.5	The WKB Approximation	151
	Bibliography	153

Chapter 1

Introduction

The final evolutionary stage for the majority of stars is an electron degenerate core with only the remaining thermal energy available to maintain the star's diminishing luminosity. These white dwarf (WD) stars are born when all other sources of nuclear and gravitational energy have been exhausted. However, some stars reach this final stage prematurely when abnormal processes interrupt their course of evolution. When evolving red giant stars are interrupted by binary interactions or excessive stellar winds, they may never reach the required mass for helium core ignition and instead are diverted onto a WD track of evolution with a degenerate helium core. The subject of this dissertation is helium-core white dwarfs (He WDs) and probing how their interior structure differs from their more common carbon/oxygen-core (C/O WD) counterparts. This interior structure is investigated by understanding pulsations on their surfaces that are observable in

their radiated light. In this introduction, we review the formation channels and subsequent evolution of He WDs as well as how pulsations can be used as an observational tool to constrain these theories. In Chapter 2 (adapted from Steinfadt et al. 2010a)¹, we use very low mass He WD models to derive their pulsational properties to highlight the parameter space of observed properties (gravity and surface temperature) where time-series observations may uncover pulsating He WDs. Using these results, in Chapter 3 we select He WD pulsation candidates from a variety of sources and observe several objects in a search for the first He WD pulsator. In Chapter 4 (adapted from Steinfadt et al. 2008b)², we summarize observations of a low gravity, but non-He core, known pulsator. Finally, in Chapter 5 (adapted from Steinfadt et al. 2008a, 2010b)¹ we highlight a fortuitous side-effect of our pulsation search, the serendipitous discovery of two unique eclipsing binary systems. A detailed description of our low mass He WD modeling code as well as notes on calculating linearized pulsation eigenfunctions and eigenmodes can be found in the Appendix.

¹Steinfadt et al. (2008a, 2010b,a) are adapted and reproduced with the permission of the American Astronomical Society.

²Steinfadt et al. (2008b) is adapted and reproduced with the permission of the Astronomical Society of the Pacific and the University of Chicago Press.

1.1 Formation and Evolution of Helium White Dwarfs

The canonical C/O-core WDs are formed when a star of less than $\approx 6\text{--}8M_{\odot}$ evolves beyond the main sequence (MS), ascends the red giant branch (RGB), ignites and commences core helium burning, ascends the asymptotic giant branch (AGB), and is then unable to ignite the C/O in its core. The remnant of the AGB star gradually cools, contracts, and is finally supported by electron degeneracy pressure to become a C/O WD (Shapiro & Teukolsky 1983). The majority of C/O WDs cluster in mass around $0.6M_{\odot}$ with an extended tail out to $1.4M_{\odot}$, illustrated in the number distribution of WDs as determined by Kepler et al. (2007) and reproduced in Figure 1.1. However, there is a significant clustering of WDs at a mass of $\approx 0.4M_{\odot}$ that cannot have formed in single star evolution as the necessary progenitors would have required greater than a Hubble time to evolve off the MS. These WDs are the He WDs.

On the RGB, the growing He core ignites when the core reaches $\approx 0.45\text{--}0.47M_{\odot}$ (D’Cruz et al. 1996; Dominguez et al. 1999; Pietrinferni et al. 2004; Vandenberg et al. 2006; Panei et al. 2007). To form a He WD, a process removes mass from the H envelope, quenching the H-shell burning that grows the He core to ignition and effectively truncates the RGB. Two modes of evolution have been proposed to truncate RGB evolution: mass loss due to binary interaction and mass loss due

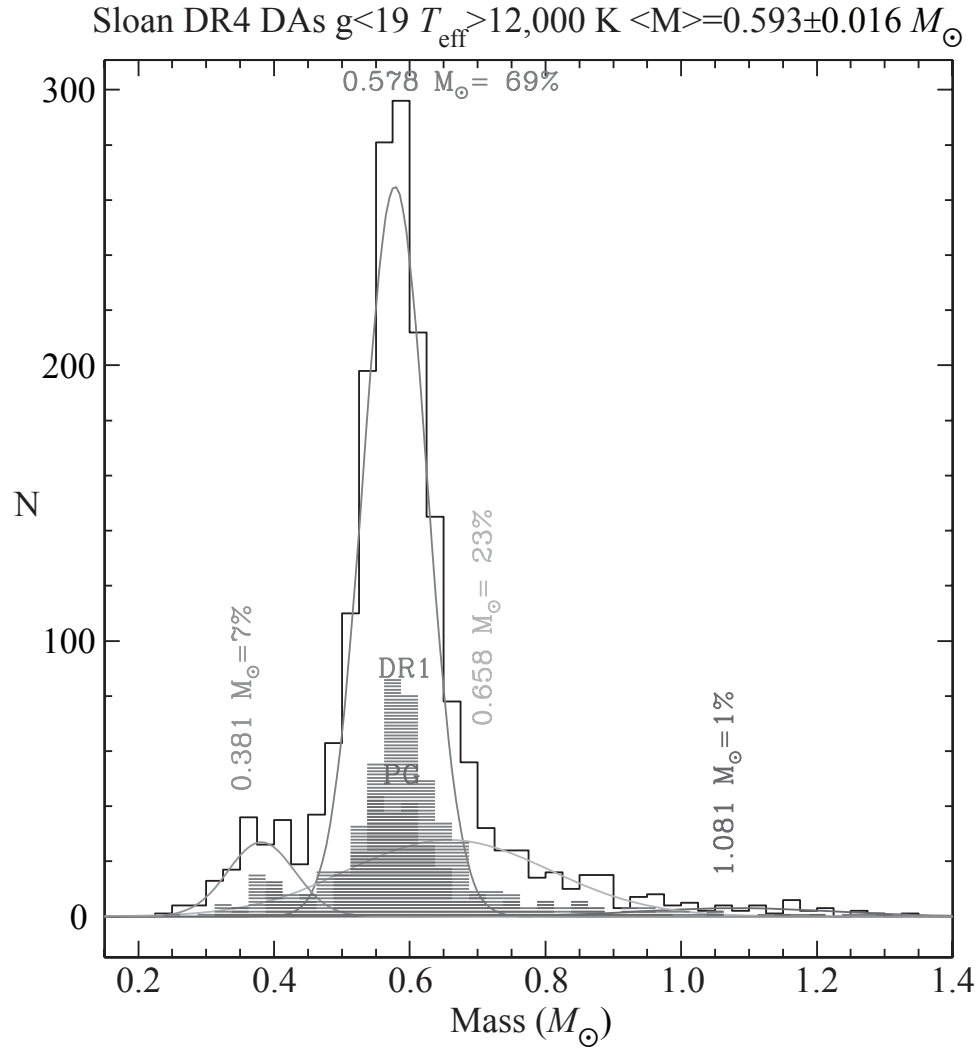


Figure 1.1: The white dwarf number-mass distribution reproduced from Kepler et al. (2007). Here we note the clustering of $0.6 M_{\odot}$ C/O WDs with their tail out to $1.4 M_{\odot}$. Clustering around $0.4 M_{\odot}$ are the He WDs.

to stellar winds.

As a progenitor star ascends the RGB, its radius increases rapidly. Eventually, if it is in a binary system, as its radius expands it will reach the gravitational equipotential surface that is bound to neither binary component, the Roche Lobe, and mass transfer from He WD progenitor to companion begins. For binary systems of sufficiently high mass ratio ($M_{\text{Progenitor}}/M_{\text{Companion}}$) and a red giant of sufficiently extended convective envelope, the mass transfer will be dynamically unstable (Hjellming & Webbink 1987). This instability causes the He WD progenitor to transfer mass faster than its companion can accept and envelops the binary system (He core of progenitor and companion) in a common envelope (Paczynski 1976; Iben & Livio 1993). As these two components orbit within their common envelope, the binary angular momentum and binding energy is transferred to this envelope and expelled in processes that are not well understood (Taam & Sandquist 2000; Deloye & Taam 2010; Ge et al. 2010), leaving a close binary system with a He WD. It is this reason that led many to believe that He WDs should be in binary systems (Marsh et al. 1995; Kilic et al. 2007b; Agüeros et al. 2009). However, several surveys have uncovered significant numbers of He WDs that do not appear to be in binary systems (Agüeros et al. 2009; Brown et al. 2010, 2011). To explain these surveys, other formation channels are required, such as binary interaction with brown dwarfs or planets (Nelemans & Tauris 1998) or high mass loss rates due to stellar winds. It is clear that the entire mass range of He

WDs ($\approx 0.1\text{--}0.45M_{\odot}$) can be formed with this channel depending on how early in the RGB phase binary interaction is initiated. Two eclipsing binary systems are examined in detail in Chapter 5 and offer direct evidence of binary interaction.

In stars of high metallicity, the increased opacity in the envelope due to metallic opacity can drive very strong stellar winds that cause mass loss in excess of $0.5M_{\odot}$ during the RGB phase (Lee et al. 1994; Catelan 2000; Hansen 2005). Therefore, it is possible that high metallicity stars may lose enough mass on the RGB due to stellar winds to avoid helium core ignition and thus leave He WDs as remnants. Evidence for this scenario is difficult to determine since metals sediment quickly in the atmospheres of He WDs and so are not directly observable. In the high metallicity ($[\text{Fe}/\text{H}]=0.4$) globular cluster NGC 6791 the main sequence turn-off age is $\approx 8\text{--}9$ Gyrs while the WD cooling age appeared to be ≈ 2.4 Gyrs and the WD luminosity function appeared over-bright (Bedin et al. 2005). It was thought that a high fraction of He WD formation via stellar winds could solve this discrepancy (Hansen 2005; Kalirai et al. 2007), however, García-Berro et al. (2010) have shown quite convincingly that normal C/O WD evolution including ^{22}Ne sedimentation (Bildsten & Hall 2001) and phase separation of C/O through crystallization (Segretain et al. 1994) match both the luminosity function and the turn-off age accurately. However, Kalirai et al. (2007) have discovered that some of the brightest WDs in NGC 6791 are He WDs with masses $\approx 0.43M_{\odot}$ and were likely formed via the strong stellar wind channel. It appears that only high mass

He WDs ($\gtrsim 0.3\text{--}0.4M_{\odot}$) can be produced through this channel.

Once formed, He WD evolution is different from that of C/O WDs because nuclear burning may still play a significant role. Studies of millisecond pulsars suggest that many He WDs are born with thick $\sim 10^{-3}\text{--}10^{-2}M_{\odot}$ H envelopes (Alberts et al. 1996; van Kerkwijk et al. 2005; Bassa et al. 2006a,b). These thick H envelopes develop long diffusive tails into the He core where the higher densities and temperatures can cause them to ignite (Driebe et al. 1999; Serenelli et al. 2002; Panei et al. 2007). This ignition highlights a dichotomy in the evolution of He WDs. For He WDs of $\gtrsim 0.18\text{--}0.20M_{\odot}$ (dependent upon metallicity) the H envelopes are radially thin enough that thin-shell instabilities develop and a series of rapid thermonuclear flashes occur. These flashes burn away the envelope leaving only a thin layer of H which allows for rapid cooling on timescales of 10s–100s of Myrs. For He WDs of $\lesssim 0.18\text{--}0.20M_{\odot}$, the nuclear burning is stable and provides a dominant energy source that slows the cooling evolution of the WD to timescales of several Gyrs (Serenelli et al. 2002; Panei et al. 2007). From an observational standpoint, very low mass He WDs ($< 0.2M_{\odot}$) may spend significantly more time in a ZZ Ceti like instability strip than the higher mass He WDs. However, it is likely that there are many more higher mass He WDs than very low mass WDs.

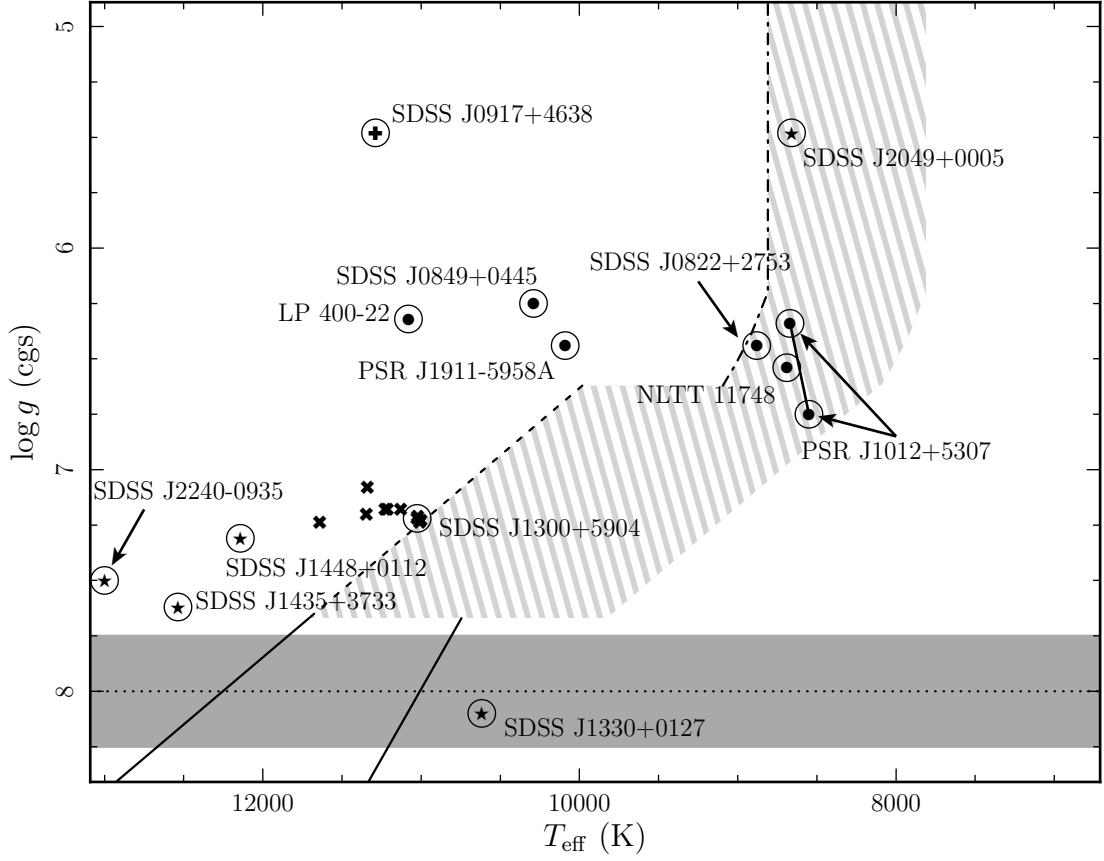


Figure 1.2: The $\log g$ - T_{eff} plane. The dark-grey horizontal strip illustrates the location of the C/O WDs. The solid lines represent the fitted boundaries of the empirical ZZ Ceti instability strip as determined by Gianninas et al. (2007) with the dashed line merely being the naive extension of the blue edge. The dash-dotted line represents the theoretical blue edge highlighted for very low mass He WDs by Steinfadt et al. (2010a) (see Chapter 2) and vertically extended at constant temperature. The light-grey hatched region represents the area of high priority used to guide our observations (see Chapter 3). We plot only objects we have observed or have firm T_{eff} and $\log g$ measurements. SDSS J1330+0127, SDSS J1435+3733, SDSS J1448+0112, SDSS J2049+0005, and SDSS J2240-0935 are from Eisenstein et al. (2006) (corrected by Silvestri et al. 2006 and Heller et al. 2009). SDSS J0822+2753 and SDSS J0849+0445 are from Kilic et al. (2010b). SDSS J0917+4638 is from Kilic et al. (2007a). SDSS J1300+5904 and the x's are from Mukremin Kilic (private communication). NLTT 11748 is from Kawka & Vennes (2009), Steinfadt et al. (2010b), and Kilic et al. (2010a). LP 400-22 is from Kawka et al. (2006). PSR J1012+5307 is from van Kerkwijk et al. (1996) and Callanan et al. (1998). PSR J1911-5958A is from Bassa et al. (2006a). The circled objects have been observed for this dissertation (Chapter 3).

1.2 Pulsations

White dwarf asteroseismology offers the opportunity of directly constraining mass, core composition, envelope composition and stratification, spin rate, and magnetic field strength (Castanheira & Kepler 2008). Asteroseismology is accomplished by observing pulsations in the light curves of stars and analyzing and identifying the specific modes of pulsations and comparing them to models. White dwarfs pulsate in three distinct classes: GW Vir (or PG 1159) stars are hot, $T_{\text{eff}} \approx 75,000\text{--}200,000$ K, and are often considered pre-WDs (Quirion et al. 2007); DBV stars are He-atmosphere WDs at $T_{\text{eff}} \approx 25,000$ K (Winget et al. 1982a; Koester & Chanmugam 1990); DAV (or ZZ Ceti) are H-atmosphere WDs at $T_{\text{eff}} \approx 12,000$ K. This dissertation is concerned with the ZZ Ceti stars.

The ZZ Ceti H-atmosphere white dwarfs pulsate in normal modes of oscillation (g -modes) where buoyancy is the restoring force (Winget & Kepler 2008). These stars exhibit pulsations when they enter the instability region, a discrete strip in the $T_{\text{eff}}\text{--}\log g$ plane that spans $11,000 \lesssim T_{\text{eff}} \lesssim 12,250$ K at $\log g = 8.0$. This strip has been extensively observed and constrained by numerous sources (Wesemael et al. 1991; Mukadam et al. 2004a; Castanheira et al. 2007; Gianninas et al. 2007) and is shown schematically in Figure 1.2. It is thought to be pure, meaning that all WDs as they cool evolve through the instability strip and exhibit pulsations, and so offers insight into the evolution of WDs (Fontaine et al. 1982; Cassisi et al. 2007).

The observability of ZZ Ceti type pulsations requires that they be driven. One type of mechanism requires that a portion of the escaping heat flux in a star be converted to mechanical motion. An example of this mechanism is the κ -mechanism where rapidly increasing opacity caused by an ionization zone bottlenecks the heat transport (Dziembowski 1977; Dziembowski & Koester 1981; Dolez & Vauclair 1981; Winget et al. 1982a). In the ZZ Ceti stars, this mechanism occurs in the middle of a convection zone and is thus not expected to be the dominant driving mechanism. Brickhill (1983) proposed that the response of this convection zone could drive pulsations in the ZZ Ceti stars. If the convection zone is unable to respond thermally on a timescale approximately faster than the pulsation mode, then the mode will grow unstably and saturate (Brickhill 1991; Wu & Goldreich 1999). Wu & Goldreich (1999) showed this criterion to be quite accurate in the high T_{eff} limit (the “blue” edge). However, this criterion had not been applied to the low gravity He WDs until Steinfadt et al. (2010b) and is highlighted in detail in Chapter 2.

As of this dissertation, no WDs have been found to pulsate for masses $<0.5M_{\odot}$. The lowest mass WD known to pulsate is HE 0031-5525 at $\log g = 7.65$ and $T_{\text{eff}} = 11,480$ K and a mass of $\approx 0.5M_{\odot}$ (Castanheira et al. 2006). The work in this dissertation set out to highlight where in the $T_{\text{eff}}\text{--}\log g$ plane He WD pulsators should exist (Chapter 2). Guided by this work, we selected candidates and observed them for pulsations and while we did not discover any pulsations

to our detection limits we have been able to constrain the He WD instability strip (Chapter 3). These candidates and their locations in the $T_{\text{eff}}\text{-}\log g$ plane are displayed in Figure 1.2. Finally, in Chapter 5 we show the lucky side-effects of a pulsation search, the discoveries of two unique eclipsing binary systems.

Chapter 2

Pulsations on Helium White Dwarfs

¹ The parameter space where low mass He white dwarfs ($<0.45 M_{\odot}$) exhibit pulsations akin to the ZZ Ceti has not been investigated fully. For many years, the driving mechanism and the expected modes of pulsation in the C/O white dwarf ZZ Ceti have been well understood and match quite well with that of observation. In this chapter, we first review how He white dwarfs fit within the current understanding of white dwarf evolution and how their pulsation properties can lead us to discovering the first He WD pulsators. We have constructed models of very low mass He white dwarfs ($<0.2 M_{\odot}$) and calculated the non-radial pulsation structure expected. We then extend the theories of Brickhill (1983) and

¹Steinfadt et al. (2010a) is adapted and reproduced with the permission of the American Astronomical Society.

Wu & Goldreich (1999) and predict the “blue” edge of the instability strip for very low mass He white dwarfs, highlighting several objects for observation.

2.1 Introduction

White dwarfs (WDs) are observed to pulsate in normal modes of oscillation (g -modes) which are determined by the structure of the stellar interior and atmosphere (Winget & Kepler 2008). Those with hydrogen atmospheres exhibit pulsations when they enter the ZZ Ceti variable (DAV) instability region, a discrete strip in the $T_{\text{eff}}\text{--}\log g$ plane that spans $11,000\text{ K} \lesssim T_{\text{eff}} \lesssim 12,250\text{ K}$ at $\log g \approx 8.0$. The ZZ Ceti strip has been investigated both theoretically (Brassard & Fontaine 1997; Wu & Goldreich 1999; Fontaine et al. 2003) and empirically (Wesemael et al. 1991; Mukadam et al. 2004b; Castanheira et al. 2007; Gianninas et al. 2007). To date, all known ZZ Ceti pulsators have masses $>0.5 M_{\odot}$, implying cores composed of carbon, oxygen, and heavier elements.

Lower mass ($M < 0.5 M_{\odot}$) WDs with nearly pure helium cores are made on the red giant branch (RGB) when core growth is truncated before reaching $\approx 0.45\text{--}0.47 M_{\odot}$ ($\log g \approx 7.67$ at $T_{\text{eff}} \approx 11,500\text{ K}$), prior to the helium core flash (D’Cruz et al. 1996; Dominguez et al. 1999; Pietrinferni et al. 2004). Two modes of envelope mass loss can cause this: strong winds or binary interaction. Significant mass loss due to stellar winds in high metallicity systems may strip the H envelope, preventing the He core flash (D’Cruz et al. 1996; Hansen 2005). Common

envelopes induced by binary interactions also lead to significant mass loss (Iben & Livio 1993; Marsh et al. 1995), and make very low-mass He WDs ($M < 0.2 M_{\odot}$) when the binary interaction occurs at the base of the RGB (van Kerkwijk et al. 1996; Callanan et al. 1998; Bassa et al. 2006a). Thus, He is the expected core composition for WDs below $\approx 0.45\text{--}0.47 M_{\odot}$. However, very little direct evidence exists of He cores. The overbrightness of old WDs (Hansen 2005) in the star cluster NGC 6791 (Bedin et al. 2005) presents possible evidence. The detection of low $\log g$ young WDs make a plausible argument for the old WDs to be He core (Kalirai et al. 2007), however, other possible explanations remain (Deloye & Bildsten 2002; Bedin et al. 2008a,b; García-Berro et al. 2010).

Asteroseismology offers the possibility of directly constraining the He core composition in these low-mass WDs, as the g -mode periods provide information on WD mass, mass of H envelope, and core composition (Córscico & Benvenuto 2002; Castanheira & Kepler 2008). Theoretically, these principles have been applied to C/O versus O/Ne core WDs by Córscico et al. (2004) and O versus He core WDs by Althaus et al. (2004). However, to carry this out, we need to find pulsating He core WDs, something that has yet to occur.

Past studies have illuminated a dichotomy in the evolution of the He core WDs (Driebe et al. 1999; Serenelli et al. 2002; Panei et al. 2007) that impacts their seismic properties and prevalence as pulsators. For masses $\gtrsim 0.2 M_{\odot}$ (dependent upon metallicity) the H envelope experiences a multitude of H shell flashes that

reduces its mass, eventually allowing the WD to cool rapidly. Such objects traverse the extrapolated ZZ Ceti instability strip in $\sim 10\text{--}100$ Myr (Panei et al. 2007), allowing for an investigation of their H layer mass, and confirmation of pure helium core. However, there are presently very few WDs with well known properties in, or near, the extrapolated strip for masses in the $0.2 < M < 0.5 M_{\odot}$ range (Steinfadt et al. 2008b), inhibiting such research. Less massive ($< 0.2 M_{\odot}$) helium WDs have a different evolution, undergoing stable H burning for Gyr, slowing their evolution to rates that may yield more in the extrapolated instability strip. However, the presence of a thick, actively burning hydrogen layer requires new seismic modeling, especially for the eventual assessment of the instability strip for these unusual WDs. The recent discovery of three such objects (Kawka & Vennes 2009; Kilic et al. 2010b) makes our work quite timely.

Motivated by a desire to study the pulsational properties of these long-lived systems, we begin in Section 2.2 by constructing He core WD models with stable H burning shells flexible enough for seismic investigations, and compare to the results from evolutionary codes (Serenelli et al. 2002; Panei et al. 2007). We discuss the unusual seismic properties of these objects in Section 2.3, where we calculate their adiabatic mode structure and, using an approximation for the instability criterion of Brickhill’s theory (Brickhill 1991), highlight the potential location of the He core WD instability strip. In Section 2.4, we suggest a few intriguing pulsation candidates amongst the very lowest mass WDs (van Kerkwijk et al. 1996; Callanan

et al. 1998; Bassa et al. 2006a; Kawka et al. 2006; Kawka & Vennes 2009; Kilic et al. 2010b), where our simple models apply. We close by highlighting the need for future work, especially if observations of our suggested targets yield the first pulsating, low-mass, He WD.

2.2 Hydrogen Burning Models

The $<0.2 M_{\odot}$ He core WDs of interest for our work are undergoing stable H burning via the PP chains in a low-mass shell. The solid/dashed lines in Figure 2.1 are the models from Serenelli et al. (2002) and Panei et al. (2007). These lines transition to solid when 90% of the luminosity is generated from the PP chains. The solid circles are the locations of the observed WDs of interest here, and are clearly in a region dominated by PP-chain burning. For this reason, we construct models with only PP-chain burning. In addition, at these late times, the diffusive timescale at the burning zone is much shorter than the age and the WD core temperature is set by that in the stable burning layer. For these reasons, the prior evolution of a stably burning WD does not affect its properties at this stage of evolution.

We construct models of a stably burning H envelope on an He core, by solving the equations of hydrostatic balance, heat transport, energy generation, and mass conservation. Between the H and He layers the most important physics in our models is the chemical profile. In these layers diffusive equilibrium is valid

as the evolutionary timescale (dominated by nuclear burning, $\sim 1\text{--}10$ Gyr) is significantly longer than the diffusive timescale ($\sim 10\text{--}100$ Myr) over a pressure scale height. We derive the equilibrium electric field by assuming each species is in hydrostatic balance with gravity and the electric force and charge neutrality (see Chang & Bildsten (2003) for more detailed derivation). With this electric field we generate an additional differential equation for one of the chemical species (charge neutrality gives the rest) to be simultaneously solved with the equations of stellar structure. Given our set of differential equations and boundary conditions, our model reduces to two parameters, total mass and total H mass, fewer than those for passively cooling C/O WDs which require total mass, H mass, He mass and surface temperature. A more detailed discussion of these models and the code can be found in Appendix A.

Our models contain zero metallicity. Additional elements require additional differential equations for their diffusive profile for which equilibrium conditions may not exist. Therefore, the PP-chains $(p(p, e^+\nu_e)^2\text{H}(p, \gamma)^3\text{He}({}^3\text{He}, pp)^4\text{He}$ or ${}^3\text{He}({}^4\text{He}, \gamma)^7\text{Be}(e^-, \nu_e(\gamma))^7\text{Li}(p, \alpha)^4\text{He}$ or ${}^7\text{Be}(p, \gamma)^8\text{B}(e^+\nu_e)^8\text{Be} 2 {}^4\text{He})$ are the only source of nuclear energy. We assume ${}^3\text{He}$ has reached its equilibrium abundance, peaking at $\sim 10^{-4}$ to 10^{-3} by mass. We generate evolutionary tracks by conserving total mass; nuclear burning converts envelope mass into core mass. Figure 2.1 compares our models with the time-dependent models of Serenelli et al. (2002) and Panai et al. (2007), exhibiting discrepancy at low gravity (large envelope mass)

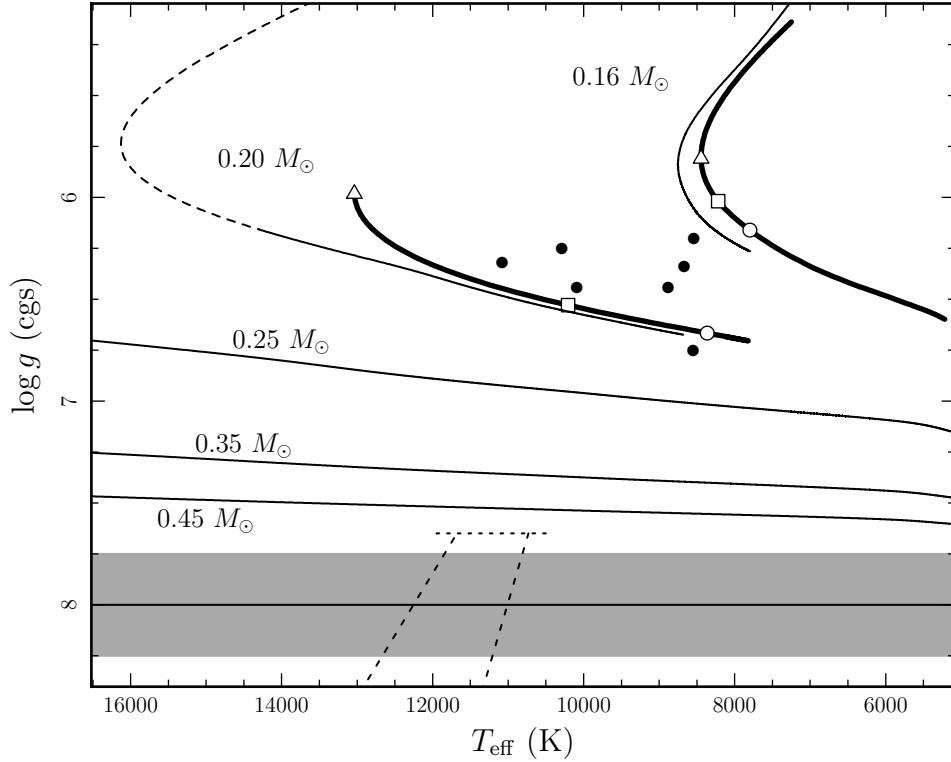


Figure 2.1: Comparison of our model tracks, the heavy black lines, against those of Panei et al. (2007), $0.16 M_{\odot}$, and Serenelli et al. (2002), 0.20 , 0.25 , 0.35 , and $0.45 M_{\odot}$, the thin black lines. Our tracks deviate significantly at low gravity from those of Serenelli et al. (2002). The solid circles are several candidate $< 0.20 M_{\odot}$ WD pulsation candidates (van Kerkwijk et al. 1996; Callanan et al. 1998; Bassa et al. 2006a; Kawka et al. 2006; Kilic et al. 2010b; Kawka & Vennes 2009). Note their location on the higher gravity, past the T_{eff} turn-around portion of the models. The dashed lines in the Serenelli et al. (2002) models denote where the CNO luminosity is greater than 10% of the PP chains. This explains the deviation as our models only have PP-chain luminosity, appropriate to the most relevant regions at higher gravity. Five Gyr have elapsed between the triangle and square marks and the square and circle marks. The gray area approximates the location of the C/O WDs with the vertical dashed lines denoting the empirical ZZ Ceti instability strip (Gianninas et al. 2007). The dotted line above the empirical instability strip denotes the gravity of the lowest known gravity ZZ Ceti, HE 0031-5525 (Castanheira et al. 2006).

but excellent agreement at high gravity (low envelope mass). This is attributed to large CNO luminosities at high envelope mass in the non-zero metallicity models of Serenelli et al. (2002). At low envelope masses, the core temperatures have lowered to $\approx 10^7$ K and CNO elements have diffused out of the burning region (Panei et al. 2007). Therefore, PP-chain luminosity dominates so we expect our models to be valid in this regime, where, as we show, the candidate He core pulsating WDs are likely to be found. As nuclear burning determines the evolution of our models, the timescales are long, of order several Gyr. Figure 2.1 illustrates the evolution of our models over 5 (triangles to squares) and 10 Gyr (triangles to circles) from the point of maximum T_{eff} .

The microphysics, opacities, equation of state, and nuclear energy generation, are all handled by the Modules for Experiments in Stellar Astrophysics (MESA)² code, developed by Paxton et al. (2011). Within MESA, the opacities are drawn from OPAL (Iglesias & Rogers 1993, 1996), the Ferguson et al. (2005) low-temperature tables, and the Cassisi et al. (2007) electron conduction tables. The equation of state is derived from OPAL (Rogers & Nayfonov 2002), low-temperature SCVH (Saumon et al. 1995), and fully ionized high temperature and density HELM (Timmes & Swesty 2000). Nuclear energy generation is calculated using the techniques developed by Timmes (1999).

²<http://mesa.sourceforge.net>

2.3 Non-Radial Pulsation Analysis

To analyze the non-radial pulsational properties of our He-core WD models we perturb and linearize the fluid equations of momentum, energy, and mass conservation. We set the transverse wavenumber of order ℓ as $k_h^2 = \ell(\ell + 1)/r^2$.

2.3.1 WKB Approximation

The star is divided into regions of wave propagation and evanescence. In the propagation zone, the wavelength k_r^{-1} is much smaller than the characteristic length scales associated with the background, such as the radius r , near the center, and the pressure scale height $\lambda_P = p/(\rho g)$ near the surface. This allows for the WKB approximation where all state variables are $\propto \exp(i \int^{r'} dr k_r)$. Neglecting perturbations on the gravitational field (the Cowling approximation) we further reduce the linearized pulsation equations into the dispersion relation,

$$k_r^2 = \frac{(N^2 - \omega^2)(c_s^2 k_h^2 - \omega^2)}{\omega^2 c_s^2}, \quad (2.1)$$

where ω is the frequency of pulsation, N is the Brunt–Väisälä frequency, and c_s is the adiabatic sound speed. For propagating waves, Equation (2.1) defines the resonant cavity for waves of two types. When $\omega > N$ and $c_s k_h$ (the Lamb frequency), waves propagate as sound waves (p -modes) where pressure provides the restoring force. When $\omega < N$ and $c_s k_h$, waves propagate as gravity waves (g -modes) where gravity provides the restoring force. Brickhill (1983) showed that

convective driving could drive the amplitude of g -mode pulsations to an observable level; these are the pulsations observed in the ZZ Cetus (Warner & Robinson 1972).

We approximate the frequencies of propagating g -modes using the WKB quantization condition $\int_{r_{\text{in}}}^{r_{\text{out}}} dr k_r = n\pi$. Under the assumptions $\omega \ll N$ and $\omega \ll c_s k_h$, Equation (2.1) gives,

$$\omega_{n,\ell} = \frac{\sqrt{\ell(\ell+1)}}{n\pi} \int_{r_{\text{in}}}^{r_{\text{out}}} \frac{dr}{r} N, \quad (2.2)$$

where the integral is bounded by the frequency dependent resonant cavity. Here r_{in} and r_{out} are the radii where $\omega = N$ and $\omega = c_s k_h$, respectively; see Figure 2.2 for illustration. Under these assumptions, the derived mode periods are only accurate for large radial order, $n \gg 1$. Figure 2.2 shows a propagation diagram for an $M_{\text{WD}} = 0.17 M_{\odot}$ and $M_{\text{env}} = 3.15 \times 10^{-3} M_{\odot}$ model. As is evident, the resonant cavity for the higher order g -modes samples much of the core and envelope while the lower orders are most affected by the transition region. It is obvious that the contribution of the transition region is quite important, therefore, close attention must be paid to the Brunt–Väisälä frequency. For changing composition, the Brunt–Väisälä frequency is,

$$N^2 = \frac{g}{\lambda_P} \left[\frac{\chi_T}{\chi_\rho} (\nabla_{\text{ad}} - \nabla) + B \right], \quad (2.3)$$

where, $\chi_\rho \equiv \partial \ln P / \partial \ln \rho|_{T, \{X_i\}}$, $\chi_T \equiv \partial \ln P / \partial \ln T|_{\rho, \{X_i\}}$, and,

$$B = \sum_{i=1}^{I-1} \left. \frac{\partial \ln \rho}{\partial X_i} \right|_{T, P, \{X_{j \neq i}\}} \frac{dX_i}{d \ln P}, \quad (2.4)$$

is the compositionally dependent Ledoux term (modified from Brassard et al. 1991) which accounts for the bulk of the bump in the Brunt–Väisälä frequency at the composition transition zone in Figure 2.2.

2.3.2 Numerical Analysis

To obtain more accurate mode periods that are not restricted to the high radial orders as our WKB analysis is, we must turn to the boundary value problem for adiabatic pulsations. The equations and method are described in Unno et al. (1989). Perturbation of the equations reduce to the following three equations for the pressure perturbation $\delta p \equiv \rho\psi$, the radial Lagrangian displacement ξ_r (the transverse Lagrangian displacement is $\xi_h = \psi r/\omega^2$), and the gravitational potential perturbation $\delta\phi$:

$$\frac{d\psi}{dr} = (\omega^2 - N^2)\xi_r + \frac{N^2}{g}\psi - \frac{d\delta\phi}{dr}, \quad (2.5)$$

$$\frac{d\xi_r}{dr} = \left(\frac{g}{c_s^2} - \frac{2}{r}\right)\xi_r + \left(\frac{k_h^2}{\omega^2} - \frac{1}{c_s^2}\right)\psi + \frac{k_h^2}{\omega^2}\delta\phi, \quad (2.6)$$

$$\frac{1}{r^2}\frac{d}{dr}\left(r^2\frac{d\delta\phi}{dr}\right) = 4\pi G\rho\left(\frac{1}{c_s^2}\psi + \frac{N^2}{g}\xi_r\right) + k_h^2\delta\phi. \quad (2.7)$$

At the center of the star, requiring the variables to be finite leads to the scalings $\psi \propto r^\ell$ and $\xi_r \propto r^{\ell-1}$. Placing these scalings into Equations (2.5), (2.6), and (2.7) leads to the central boundary conditions,

$$\omega^2\xi_r = \ell\frac{\psi + \delta\phi}{r}, \quad (2.8)$$

$$\ell\frac{\delta\phi}{r} = \frac{d\delta\phi}{dr}, \quad (2.9)$$

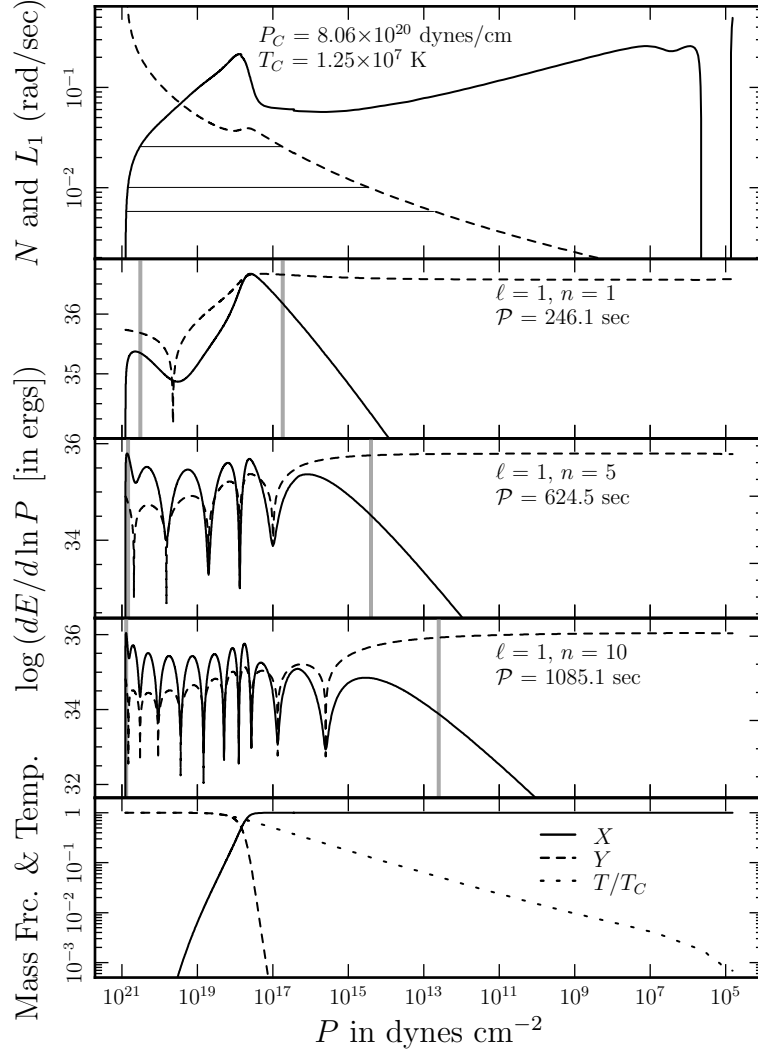


Figure 2.2: Propagation diagram (upper panel) for our $M_{\text{WD}} = 0.17 M_{\odot}$ and $M_{\text{env}} = 3.15 \times 10^{-3} M_{\odot}$ model. Gravity mode (g -mode) pulsations exist below both the Brunt–Väisälä frequency (solid curve) and the Lamb frequency ($\ell = 1$; dashed curve). The thin horizontal lines delineate the locations of the $n = 1, 5$, and 10 modes for $\ell = 1$. Note the large bump in the Brunt–Väisälä frequency due to the Ledoux contribution (Equation 2.4) that aligns with the composition transition region (bottom panel). The middle three panels show the eigenfunction solutions of ξ_h (dashed curves) and mode energy (solid curves) for the $n = 1, 5$, and 10 modes for $\ell = 1$. The gray vertical lines denote the boundaries of the WKB propagation cavity. These show the bulk of each mode to reside in the core, below the H/He transition, with only a couple nodes existing in the envelope. This model is our closest fit to the properties of NLTT 11748 (Kawka & Vennes 2009; Section 5.2).

at a nonzero, but small, radius r . At the surface, we require the perturbations to be both finite and upwardly evanescent. Unno et al. (1989) show that the correct boundary conditions are then

$$\psi = g\xi_r, \quad (2.10)$$

$$-(\ell + 1)\frac{\delta\phi}{r} = \frac{d\delta\phi}{dr}, \quad (2.11)$$

at the upper boundary of the model. We solve Equations (2.5), (2.6), and (2.7) with the boundary conditions in Equations (2.8), (2.9), (2.10), and (2.11) using the shooting method to obtain all mode periods. A detailed derivation of the adiabatic pulsation equations and boundary conditions can be found in Appendix B.

The middle three panels in Figure 2.2 display the transverse displacement eigenfunctions and energy density for the $n = 1, 5,$ and 10 modes for $\ell = 1$. The energy density illustrates where each mode “lives,” that is, what portions of the star most affect the mode period. These modes live primarily in the core, below the H/He transition region, as the energy density declines rapidly in the lower pressure H layer. This contrasts the normal ZZ Cetus (Fontaine & Brassard 2008). This is predominantly because the Brunt–Väisälä frequency in the He core is larger than in the envelope (see Figure 2.2, also noted in Althaus et al. 2004). The electron degeneracy in all WD cores leads to most of the entropy in the ions, yielding $N^2 \sim A^{-1}(k_b T/E_F)(g/\lambda_P)$, where A is the ion mass and E_F is the electron Fermi energy. Hence, there are two reasons why N is relatively larger

in an He core than in a C/O core. First, low-mass implies smaller $E_F \propto M^{4/3}$, and second, $1/A$ is larger for He than a C/O mixture. This shows the power these modes will have in probing the core composition once pulsations have been detected and accurate periods measured.

The observability of these modes requires that they be driven. One type of driving mechanism requires that a portion of the escaping heat flux be converted into the mechanical energy of the pulsation modes. An example is given by the κ -mechanism (Dziembowski 1977; Dziembowski & Koester 1981; Dolez & Vauclair 1981; Winget et al. 1982b), in which the rapid outward increase in opacity associated with an ionization zone bottlenecks the heat flux. For ZZ Ceti-like pulsations, Brickhill (1983) proposed that the response of the convection zone itself to the pulsation drives the instability (Brickhill 1983, 1991; Wu & Goldreich 1999). For now we consider only the convective driving mechanism³. If the convection zone can thermally adjust on a timescale shorter than the pulsation period, \mathcal{P} , then the pulsation will be damped. This motivates the convective thermal time instability criterion $\mathcal{P} \leq 8\pi\tau_{\text{th, bcvz}}$, where $\tau_{\text{th, bcvz}}$ is the thermal time from the base of the convection zone to the surface (Brickhill 1991; Wu & Goldreich 1999). Wu & Goldreich (1999) show (in their Figure 7) this criterion to be quite accurate in the high T_{eff} (the “blue” edge) limit compared to fully nonadiabatic calculations on a $\log g = 8.0$ WD. However, the He core WDs are at

³The existence of the nuclear burning region inside the mode propagation region may additionally drive modes due to the sensitivity of the nuclear reactions to temperature, the ϵ -mechanism (Kawaler 1988). We have yet to investigate this possibility.

significantly lower gravity, requiring an extrapolation in $\log g$. Calculations show that the rapid increase in $\tau_{\text{th, bcvz}}$ due to the deepening convective zone occurs at lower T_{eff} for lower $\log g$, nearly 1500 K for $\log g = 8$ to $\log g = 7$. The circle points on the $\log g$ – T_{eff} evolution plots in Figure 2.3 show where the convective thermal time instability criterion is met for $\ell = 1$ and $n = 1$ modes. As is seen, Figure 2.3 highlights many excellent targets for an observational study of He core WDs, as we comment in the conclusions.

2.4 Conclusions

Our work highlights the $\log g$ – T_{eff} parameter space where observable pulsations may be present. This reveals at least three pulsation candidates, NLTT 11748 (Kawka & Vennes 2009; Steinfadt et al. 2010b; Section 5.2), SDSS J0822+2753 (Kilic et al. 2010b), and PSR J1012+5307 (van Kerkwijk et al. 1996; Callanan et al. 1998), all of which should be observed for variability on timescales of 200–1000 s. All of these objects have been observed in Chapter 3 and show no pulsations. Mode detections and a measurement of the mode period spacing would provide key evidence for an He core composition and large radius, as we predict a period spacing of ≈ 90 s for $\ell = 1$, whereas in normal ZZ Ceti, this number is ≈ 50 s (Kleinman et al. 1998; Kanaan et al. 2005; Pech et al. 2006). Our results regarding the region of instability should be confirmed through future nonadiabatic stability analyses, an issue that is beyond the scope of the present paper.

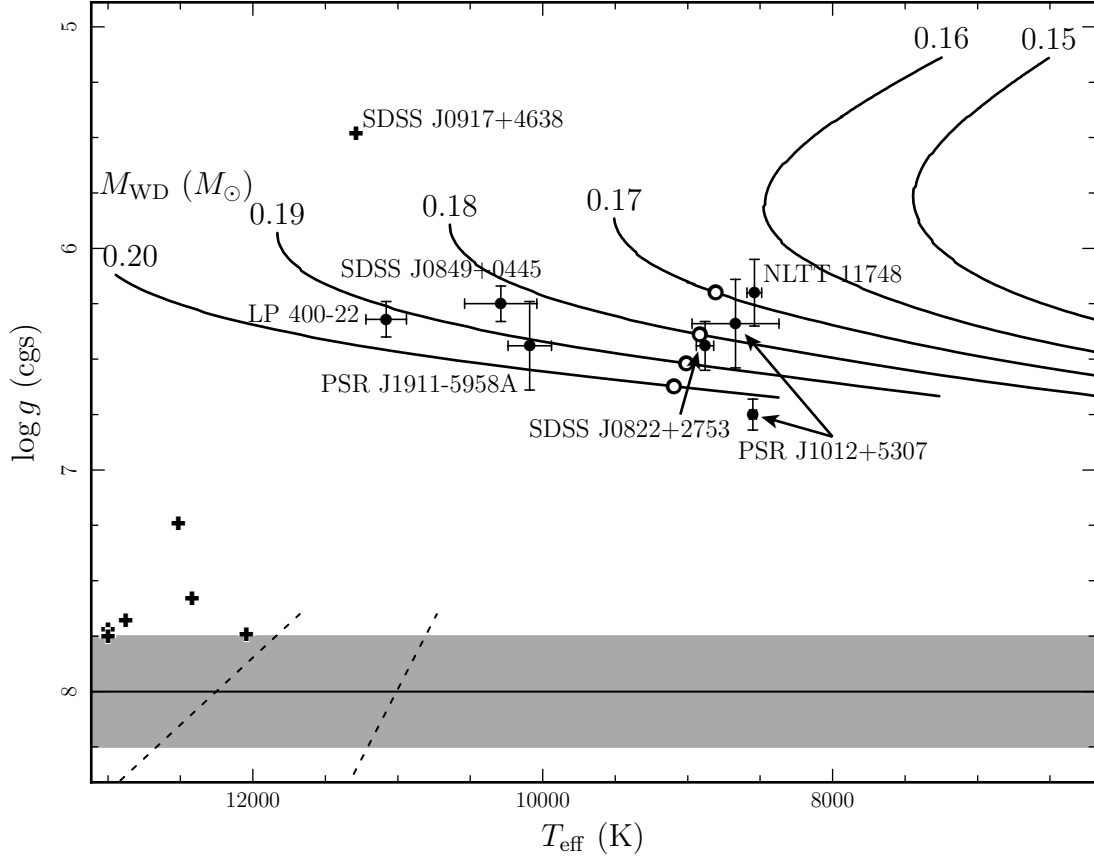


Figure 2.3: Evolution of stably burning low-mass He cores. Evolution proceeds top to bottom. We start our $0.20 M_{\odot}$ model where the deviations from the time-dependent Serenelli et al. (2002) models have been reduced to less than $\Delta \log g = 0.2$ (see Figure 2.1). For our 0.17 , 0.18 , and $0.19 M_{\odot}$ models we begin at the maximum T_{eff} turn as we have no models to directly compare. We show our entire 0.15 and $0.16 M_{\odot}$ models, starting with $M_{\text{env}} = 10^{-2} M_{\odot}$, as our comparison with Panei et al. (2007) show them to be reliable (Figure 2.1). For comparison we exhibit the location of the C/O WDs (the shaded region) and their associated empirical instability strip, the sloped dashed lines (Gianninas et al. 2007). Candidate objects are drawn from several sources. The bullets are PSR J1911-5958A (Bassa et al. 2006a), PSR J1012+5307 (van Kerkwijk et al. 1996; Callanan et al. 1998), SDSS J0849+0445 and SDSS J0822+2753 (Kilic et al. 2010b), NLTT 11748 (Kawka & Vennes 2009; Section 5.2), and LP 400-22 (Kawka et al. 2006). The crosses are those SDSS selected low-mass WDs confirmed by MMT spectra from Kilic et al. (2007a). The circles on the evolution curves represent where the convective thermal time instability criterion is met for the $\ell = 1$ and $n = 1$ modes.

NLTT 11748 is highlighted in Figure 2.3 as a candidate for observable pulsations. Recent observations by Steinfadt et al. (2010b) did not find pulsations down to a 4 mmag level, however, they did discover it to be the first eclipsing He WD system (see also Section 5.2). Given its measured $\log g = 6.20$ and $T_{\text{eff}} = 8540$ K, our models predict a total mass of $0.17 M_{\odot}$ and envelope mass of $3.15 \times 10^{-3} M_{\odot}$, comparable to that reported by Kawka & Vennes (2009). Our numerical pulsation analysis reveals that for this object the lowest order g -mode ($\ell = 1$ and $n = 1$) has a period of 245 s but more importantly the mean period spacing is 89 s for the $\ell = 1$ modes and 51 s for the $\ell = 2$ modes. Figure 2.2 clearly shows these modes to preferentially reside in the core, offering a unique opportunity to probe the core composition of an He WD.

The current candidates were found in surveys that target other phenomena: the Sloan Digital Sky Survey (SDSS; Kilic et al. 2007a), high velocity stars (Kawka et al. 2006; Kawka & Vennes 2009), and companions to pulsars (van Kerkwijk et al. 1996; Callanan et al. 1998; Bassa et al. 2006a). However, the survey selection criteria (photometric colors), although incomplete, can favor WDs of higher T_{eff} ($T_{\text{eff}} \gtrsim 11,000$ K in the SDSS for $\log g < 6$, Kilic et al. 2007a). Surveys able to select low-gravity WDs down to $T_{\text{eff}} = 8,000$ K will significantly impact the study of pulsating He core WDs.

Chapter 3

Pulsation Candidates and Null Detections

An efficient search for pulsating He core white dwarfs (He WDs) requires foreknowledge of parameters that increase the probability of finding pulsations. For the canonical C/O core white dwarfs it is well known that the observed pulsators (ZZ Ceti) are found in a discrete strip in the $T_{\text{eff}}\text{-}\log g$ plane, where g is the gravity on the WD surface. Gravity and effective temperature are quantities that require a detailed theoretical understanding of the WD atmospheres. Theoretical models of WD atmospheres (Finley et al. 1997; Bergeron et al. 1992; Tremblay & Bergeron 2009) predict a spectrum given a $\log g$ and T_{eff} . By fitting an observed spectrum to these atmosphere models the $\log g$ and T_{eff} can be measured. We showed in Chapter 2 that by using the same theory that describes the ZZ Ceti in-

stability strip we predict a distinct hot (blue) edge of the instability strip for very low mass He WDs ($M_{\text{WD}} < 0.2M_{\odot}$). This predicted blue edge of the instability strip is at $T_{\text{eff}} \approx 9,000$ K for $\log g < 6.5$. However, no work has been done to predict the amplitudes of these pulsations. Further, no theoretical work has been done to connect this very low mass He WD blue edge with that of the ZZ Ceti. To fill this gap we have turned to the empirical and theoretical knowledge concerning the canonical ZZ Ceti.

The ZZ Ceti instability strip spans $11,000 \lesssim T_{\text{eff}} \lesssim 12,250$ K at $\log g \approx 8.0$, the fiducial gravity for a $0.6M_{\odot}$ C/O WD, and has the shape shown schematically in Figure 3.1. This instability strip has been extensively investigated both theoretically (Brassard & Fontaine 1997; Wu & Goldreich 1999; Fontaine et al. 2003) and observationally (Wesemael et al. 1991; Mukadam et al. 2004b; Cassisi et al. 2007; Gianninas et al. 2007) and we will use these trends to guide our observations of He WDs. Red giant branch modeling (D’Cruz et al. 1996; Dominguez et al. 1999; Pietrinferni et al. 2004) show that the maximum mass of a He WD to be $\approx 0.45M_{\odot}$ as a more massive He core would experience He ignition and burn to C/O. Models of He WDs (Driebe et al. 1999; Serenelli et al. 2002; Panei et al. 2007) show this mass to have $\log g \approx 7.6$ near the temperatures of the ZZ Ceti instability strip. When selecting our candidates for observation, we select only those candidates whose gravity measurements are $\log g < 7.6$. For normal mass He WDs ($0.2 < M_{\text{WD}} < 0.45M_{\odot}$) the blue edge of the instability strip has not

been theoretically investigated. Therefore, we naively extrapolate the ZZ Ceti empirical blue edge (from Gianninas et al. 2007) to the lower gravities of the He WDs and connect it to the instability strip blue edge for very low mass He WDs, as shown in Figure 3.1.

Since no work has been done to predict the amplitudes of pulsations in potential He WD pulsators, we rely on the empirical trends that have been discovered in the ZZ Ceti. The majority of ZZ Ceti pulsators observed show pulsation amplitudes of $\lesssim 30$ mmags ($\approx 3\%$)¹ with some showing amplitudes as low as 2 mmags (Mukadam et al. 2006). We used 10 mmags as a fiducial amplitude when planning our observations.

3.1 Finding Candidates

To select He WD candidates for observation we generally select only those WDs with $\log g < 7.6$ and $7,000 < T_{\text{eff}} < 12,000$ K. We select a much larger range of temperatures than those suggested by our own theoretical analysis and ZZ Ceti properties because non-detections of pulsations in candidates are still beneficial as they constrain the parameter space in which the conventional theory must hold. Of added interest is the potential detection of pulsations in parameter space not predicted by theory. Objects that are within the hatched grey strip

¹We will often express amplitudes and differential limits in the mmag unit. For a small change in flux ΔF compared to F we can express the magnitude change as $\Delta m = 2.5 \log [(F + \Delta F) / F] = (2.5 / \ln 10) \ln (1 + \Delta F / F) \approx 1.086 (\Delta F / F)$. Therefore, 10 mmags closely corresponds to a 1% change in flux.

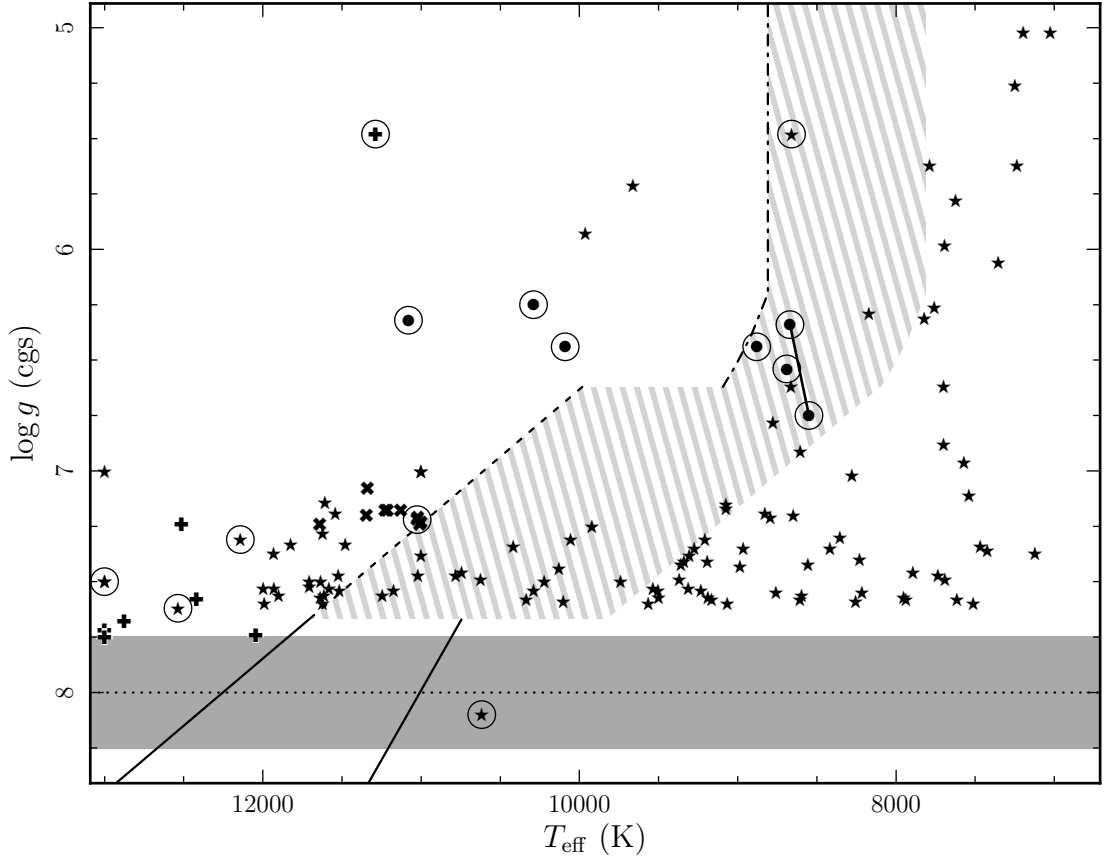


Figure 3.1: The $\log g$ - T_{eff} plane highlighting the instability strip. The dark-grey horizontal strip illustrates the location of the C/O WDs. The solid lines represent the fitted boundaries of the empirical ZZ Ceti instability strip as determined by Gianninas et al. (2007) with the dashed line merely being the naive extension of the blue edge. The dash-dotted line represents the theoretical blue edge highlighted for very low mass He WDs by Steinfadt et al. (2010a) (see Chapter 2) and vertically extended at constant temperature. The light-grey hatched region represents the area of high priority used to guide our observations. The bulleted objects are from single object papers (van Kerkwijk et al. 1996; Callanan et al. 1998; Bassa et al. 2006a; Kawka et al. 2006; Kawka & Vennes 2009; Kilic et al. 2010b,a; Steinfadt et al. 2010b; the connected bullets are the two PSR J1012+5307 measurements). The crosses are SDSS selected low mass WDs from Kilic et al. (2007a). The stars are SDSS WDs from Eisenstein et al. (2006) (corrected by Silvestri et al. 2006 and Heller et al. 2009) including only objects whose $\log g < 7.6$ and $7,000 < T_{\text{eff}} < 12,000$ K. The x's are objects from the candidate hypervelocity star sample of Brown et al. (2006) analyzed by Mukremin Kilic (private communication). The circled objects have been observed for this dissertation.

redward (cooler) of the instability strip blue edge marked in Figure 3.1 are given a higher priority when executing observations.

We find most of our candidates through surveys looking for other phenomena, e.g. the Sloan Digital Sky Survey (SDSS), but we have also found candidates in single object papers. Companions to pulsars have been found to be good candidates such as PSR J1911-5958A (Bassa et al. 2006a) and PSR J1012+5307 (van Kerkwijk et al. 1996; Callanan et al. 1998).

Eisenstein et al. (2006) offers a catalog of WDs within the SDSS that is the largest to date. They found their WDs by selecting SDSS spectra using a series of color cuts and then fitting to a large grid of WD atmospheric models. Objects with spectral contamination due to a companion star, e.g. an M-dwarf star, were not decontaminated and thus the spectral fits obtained were often erroneous. This is an issue for He WDs as their primary formation channel requires a binary companion which frequently contaminates the spectrum. Many of these contaminated spectra were reanalyzed by Silvestri et al. (2006) and Heller et al. (2009) in two catalogs of close binary systems. In these cases, the derived parameters of Silvestri et al. (2006) and Heller et al. (2009) were used. Since the SDSS sample did not target WDs specifically, the quality of the spectra of many of the WDs is low as is the model fits derived from them. Therefore, we generally do not pursue SDSS targets unless additional spectra have been taken.

Brown et al. (2006) performed a hypervelocity star survey looking for B-type

stars escaping the galactic center. They used SDSS photometry to color select their B-type stars and gathered high signal-to-noise spectra looking for large radial velocities. Given their color selection, Kilic et al. (2007a,b, 2010b) made great use of this data-set, uncovering many low mass He WDs. Kawka et al. (2006) and Kawka & Vennes (2009) have used a similar technique to the Brown et al. (2006) survey and searched for hypervelocity stars in proper motion data from a variety of sources (Oswalt et al. 1993, New Luyten Two Tenths, NLTT, Proper Motion Survey). Their survey has discovered some of the lowest mass WDs known (Kawka & Vennes 2009; Kawka et al. 2006).

3.2 Observational Strategy

In all, the surveys in the previous section have revealed dozens of candidates, only 13 of which have been observed for this dissertation and are summarized in Table 3.1. Unfortunately, none of the 13 are observed to pulsate.

The observations we executed followed a simple strategy. Chapter 2 showed that the expected periods of potential pulsations range between 250 and 1,000 seconds. Extrapolating our knowledge of the ZZ Cetus we considered a fiducial amplitude of 10 mmags. We designed each observation to be sensitive to these properties by incorporating a fast cadence (usually less than 60 seconds) and individual measurements of the target that met or exceeded 10 mmags in precision (in the Poisson limit, 10,000 photons/image). In Table 3.2 we report on the details

Table 3.1. Summary of Observed Candidates and Results

Object	g' -SDSS (mag)	$\log g$ (cgs)	T_{eff} (K)	Reference	Det. Limit ^a (mmag)
SDSS J0822+2743	18.3	6.55 ± 0.11	$8,880 \pm 60$	Kilic et al. (2010b)	8
SDSS J0849+0445	19.3	6.23 ± 0.08	$10,290 \pm 250$	Kilic et al. (2010b)	15
SDSS J0917+4638	18.7	5.48 ± 0.03	$11,288 \pm 72$	Kilic et al. (2007a)	11
SDSS J1300+5904	15.2	7.22 ± 0.02	$11,025 \pm 63$	M. Kilic, priv. com.	3
SDSS J1330+0127	18.9	8.1 ± 0.2	$10,617 \pm 452$	Silvestri et al. (2006)	44
SDSS J1435+3733	17.1	7.62 ± 0.12	$12,536 \pm 488$	Eisenstein et al. (2006)	4
SDSS J1448+0112	19.6	7.31 ± 0.18	$12,142 \pm 486$	Eisenstein et al. (2006)	34
SDSS J2049+0005	19.7	5.48 ± 0.10	$8,660 \pm 144$	Eisenstein et al. (2006) ^b	21
SDSS J2240-0935	17.6	6.96 ± 0.09	$11,449 \pm 205$	Heller et al. (2009)	14
LP 400-22	17.2	6.32 ± 0.08	$11,080 \pm 140$	Kawka et al. (2006)	4
NLTT 11748	17.1 ^c	6.54 ± 0.05	$8,690 \pm 140$	Kilic et al. (2010a)	5
PSR J1012+5307	19.5 ^d	6.34 ± 0.20	$8,670 \pm 300$	Callanan et al. (1998)	20
		6.75 ± 0.07	$8,550 \pm 25$	van Kerkwijk et al. (1996)	
PSR J1911-5958A	22.2 ^d	6.44 ± 0.20	$10,090 \pm 150$	Bassa et al. (2006a)	16

^aReporting the best limit over a minimum of 1–7 mHz frequency range (where possible). See Table 3.3 for frequency range details and multiple epochs.

^bSDSS J2049+0005 is likely a distant A star (Eisenstein et al. 2006; Kilic et al. 2007a).

^cMagnitude in Johnson B .

^dMagnitude in Johnson V .

of our observations.

3.2.1 Aperture Photometry

All images were reduced using standard methods (bias subtracted and flat fielded). In most cases, the CCD detectors under-sampled the point spread function (PSF) of the stars making PSF-fitting photometry highly imprecise. Therefore, aperture photometry was executed using the Image Reduction and Analysis Facility (IRAF) software package *apphot*.

During an observation, variable sky conditions (e.g. clouds) cause variations in atmospheric transmission from one image to the next. This has a multiplicative effect on the count rates for each star in the field-of-view. Fortunately this multiplicative factor is the same across an entire image since the variations in atmospheric transmission occur on spatial scales much larger than the field of view. This effect is corrected by using comparison stars and differential photometry. By dividing the count rate of a presumed non-variable star by the count rate of our target star we construct a ratio that is constant regardless of the atmospheric conditions unless our target happens to be variable. However, since the comparison star has its own noise we select bright stars whose noise is Poisson dominated and combine multiple comparison stars by weighting them inversely to their intrinsic variance over a single run of observation (a technique similar to that used in Gilliland & Brown 1988 and Sokoloski et al. 2001). We ensure all comparison

Table 3.2. Details of Observations

Object	g' -SDSS (mag)	Telescope/ Camera/Filter	Date (yyyymmdd)	Len. (hrs.)	Exp. Time (s)	N. of Exp. ^a
SDSS J0822+2743	18.3	WHT/ACAM/ g'	20110220	2.1	30	137
SDSS J0849+0445	19.3	WHT/ACAM/ g'	20110117	1.9	60	96
SDSS J0917+4638	18.7	WHT/ACAM/ g'	20110220	2.3	45	145
SDSS J1300+5904	15.2	BOS/SBIG/Clear	20110126	5.0	50	295
		BOS/SBIG/Clear	20110201	5.2	50	297
SDSS J1330+0127	18.9	WIYN/OPT/BG39	20070530	1.6	90	57
SDSS J1435+3733	17.1	WIYN/OPT/BG39	20070529	1.5	15	197 ^b
		WIYN/OPT/BG39	20070531	1.9	15	233 ^b
		WIYN/OPT/BG39	20070601	3.8	45	259 ^b
SDSS J1448+0112	19.6	WIYN/OPT/BG39	20070531	2.0	60	104
SDSS J2049+0005	19.7	WIYN/OPT/BG39	20070531	3.4	60	166
SDSS J2240-0935	17.6	P60/P60CCD/ g	20060804	3.7	30	204
		P60/P60CCD/ g	20060817	4.5	100	73 ^c
		P60/P60CCD/ g	20060919	1.1	30	57
		P60/P60CCD/ g	20060925	1.0	30	60
		P60/P60CCD/ g	20061205	0.9	30	59
LP 400-22	17.2	WIYN/OPTIC/ g'	20070530	2.4	20	269
NLTT 11748	17.1 ^d	FTN/Merope/ g'	20091222	4.0	45	198 ^b
		FTN/Merope/ g'	20100108	3.3	45	167 ^b
PSR J1012+5307	19.5 ^e	WHT/ACAM/ g'	20100330	2.0	60	103
PSR J1911-5958A	22.2 ^d	HST/WFC3/F200LP	20100305	6.0	60	142

^aExcludes images contaminated by cosmic rays, clouds, and excess noise.

^bAlso excludes images taken during eclipse.

^cObservation contains large gaps.

^dMagnitude in Johnson B .

^eMagnitude in Johnson V .

stars are non-variable by comparing each prospective star within the field-of-view with all others in every combination and use periodograms to ensure no periodic trends are present.

Atmospheric turbulence causes the PSF of stars to fluctuate from image to image, spreading the light of each star over smaller or larger spatial scales depending on the seeing (usually measured as the full width half maxima, FWHM, of a 2D-gaussian function fitted to a star's PSF). We employ a variable aperture algorithm to optimize the signal-to-noise of our photometry in order to combat the varying PSF. For each observation, a single representative frame was selected. For every star in the image we varied the size of the photometric aperture to find that size which optimized the signal-to-noise of the measurement. The optimum apertures were then scaled by the average FWHM of 2D-gaussians fitted to each star. For all other images the average FWHM of the stellar PSFs was measured and then scaled using the appropriate optimum scaling. Therefore, as the seeing fluctuates during an observation the apertures are adjusted larger or smaller as a star's light is spread over larger and smaller scales (a technique similar to that used in Deeg & Doyle 2001).

Once we have constructed the light curve for our target star there are often long timescale trends still present in the data. These trends are usually caused by the color-airmass effect. Our atmosphere preferentially scatters and absorbs blue light over red and the ratio of the transmissions changes depending on the

amount of atmosphere we are looking through. Objects seen near the horizon will appear redder than the same object observed at zenith (e.g. the sun at midday versus the sun at sunset). If our comparison stars are the same color as our target star, which is seldom the case, then this effect is zero and is not a problem. We can correct for this effect by correlating our light curve with airmass (defined as the secant of the angle to zenith of observation) and dividing a fitted trend from the light curve. For some observations this trend removal is insufficient as other systematics may be present (e.g. variable sky background due to the moon). In these cases low order polynomials are fitted against time and divided from the light curve.

3.2.2 Periodograms and Detection Limits

To detect potential pulsations in our light curve, we use a Lomb-Scargle periodogram (Scargle 1982) instead of a standard Fourier transform because our observations are frequently unevenly spaced and sometimes filled with large gaps. In the ZZ Ceti, low amplitude pulsations show pulse shapes that are closely approximated by sinusoids while high amplitude pulsations frequently show narrow peaks in their shape (Fontaine & Brassard 2008). We feel this justifies our use of a periodogram which is optimized for sinusoidal signals because the pulsations that are “in the noise” are closely represented by sinusoids. High amplitude pulsations, though non-sinusoidal, should still be easily detected as they will likely be well

above the noise.

In this dissertation, and to date, no significant pulsation signals have been detected in a He WD. However, null detections and detection limits are still useful in both deciding if additional observations are required and constraining theory. We measure our detection limits by using signal injection and the properties of a Lomb-Scargle periodogram. For a periodogram normalized by the variance of the total light curve, a false-alarm probability is naturally generated that states for M independent frequencies the probability that independent and normal noise produces power greater than z in any of the frequency bins is $\text{Prob}(\text{Any Power} > z) = 1 - (1 - e^{-z})^M$ (Scargle 1982; Horne & Baliunas 1986). Thus, a signal may be considered 90% significant if it has a false-alarm probability of 10%. However, our noise may not be precisely normal and independent due to potential unresolved pulsations and other systematic effects (such as atmospheric correlated noise) that may cause our data to be slightly correlated. This may cause us to slightly overestimate our detection limits. Simulations of normal random data distributed with the same errors as our light curves have shown us that this effect is minimal. We determine our detection limits by injecting sinusoidal signals, integrated over the observation's exposure times, at a single frequency and test all phases. We then increase the amplitude of the signal until 90% of all phases produce a peak in the periodogram at the injected frequency that is 90% significant. Finally, all frequencies accessible by the data are tested with this method. In all cases

Table 3.3. Results of Observations

Object	Date	Filter	Detection Limit (mmag)	Frequency Range (mHz)
SDSS J0822+2743	2011/02/20	g' -SDSS	8	1–11
SDSS J0849+0445	2011/01/17	g' -SDSS	15	1–7
SDSS J0917+4638	2011/02/20	g' -SDSS	11	1–8
SDSS J1300+5904	2011/01/26	Clear	6	1–8
	2011/02/01	Clear	3	1–8
SDSS J1330+0127	2007/05/30	BG-39	44	1–5
SDSS J1435+3733	2007/05/29	BG-39	4	1–17
	2007/05/31	BG-39	6	1–17
	2007/06/01	BG-39	4	1–9
SDSS J1448+0112	2007/05/31	BG-39	34	1–7
SDSS J2049+0005	2007/05/31	BG-39	21	1–7
SDSS J2240-0935	2006/08/04	Gunn- g	22	1–7
	2006/08/17	Gunn- g	13	1–2.25
	2006/09/19	Gunn- g	14	1–7
	2006/09/25	Gunn- g	16	1–9
	2006/12/05	Gunn- g	48	1–9
LP 400-22	2007/05/30	g' -SDSS	4	1–15
NLTT 11748	2009/12/22	g' -SDSS	5	1–7
	2010/01/08	g' -SDSS	4	1–7
PSR J1012+5307	2010/03/30	g' -SDSS	20	1–7
PSR J1911-5958A	2010/03/05	F200LP	16	1–3.25

in this dissertation, the detection limits were largely independent of frequency allowing us to state one detection limit over a range of frequencies. The results of our observations are shown in Table 3.3 and summarized in the next section and Table 3.1.

3.3 Summary of Observations and Results

In the course of this dissertation, several observing setups were employed. Here we summarize the details of the telescopes and instrumentation used.

The William Herschel Telescope (WHT) is a 4.2-m telescope at the Roque de Los Muchachos Observatory on La Palma in the Canary Islands. We used the ACAM imager and the SDSS- g' filter with a circular $8'.3$ diameter field-of-view in a 2×2 pixel binning mode for an effective spatial resolution of $0'.5 \text{ pixel}^{-1}$. Using the fast readout mode we maintain a total dead-time of ≈ 11 s between exposures. All observations using this setup were carried out using Service Time, generally at bright time (near the calendar full moon).

The Byrne Observatory at Sedgwick Reserve (BOS) telescope is a 0.8-m robotically controlled telescope that is part of the Las Cumbres Observatory Global Network of telescopes (LCOGT) on the Sedgwick Nature Reserve north of Santa Barbara, California. We used the SBIG imager and a clear filter with a $17' \times 10'$ field-of-view in a 2×2 pixel binning mode for an effective spatial resolution of $0'.57 \text{ pixel}^{-1}$. The total dead-time between exposures was ≈ 10 s. This setup was used in late-January and early-February 2011.

The Wisconsin Indiana Yale NOAO (WIYN) telescope is a 3.5-m telescope at the Kitt Peak National Observatory in Arizona. We used the OPTIC imager and the broadband filter BG-39 ($\lambda_c \approx 480$ nm, FWHM ≈ 260 nm) with a $9'.5 \times 9'.5$ field-of-view in a 2×2 pixel binning mode for an effective spatial resolution of

$0''.28 \text{ pixel}^{-1}$. The total dead-time between exposures was ≈ 10 s. All observations using this setup were carried out in a single observing run that occurred in late-May and early-June 20 2007.

The Palomar 60-inch (P60) telescope is a 1.5-m robotically controlled telescope at the Palomar Observatory on Mount Palomar in southern California. We used the P60CCD imager and the Gunn- g filter with a $12'.9 \times 12'.9$ field-of-view with a spatial resolution of $0''.38 \text{ pixel}^{-1}$. We decreased readout times by reading out half of the two CCD chips for a total dead-time between exposures of ≈ 20 – 40 s. The large variation in dead-time was due to a software issue in the telescope software. This setup was used in late 2006 and early 2007, however, most of the data taken during that time was for other projects (see Chapter 4 for observations of HS 1824+6000, a ZZ Ceti) or was too degraded by weather.

The Faulkes Telescope North (FTN) is a 2.0-m robotically controlled telescope on Haleakala, Hawaii and is part of LCOGT. We used the Merope imager and the SDSS- g' filter with a $4'.75 \times 4'.75$ field-of-view in a 2×2 pixel binning mode for an effective spatial resolution of $0''.28 \text{ pixel}^{-1}$. The total dead-time between exposures was ≈ 22 s. This setup was used in late-December 2009 and early-January 2010.

The Hubble Space Telescope (HST) is a 2.4-m space telescope in low-earth orbit operated by the Space Telescope Science Institute and NASA. We used the Wide Field Camera 3 (WFC3) UVIS channel and the F200LP filter ($\lambda_c \approx 490$ nm, FWHM ≈ 250 nm). To decrease readout times and to avoid onboard

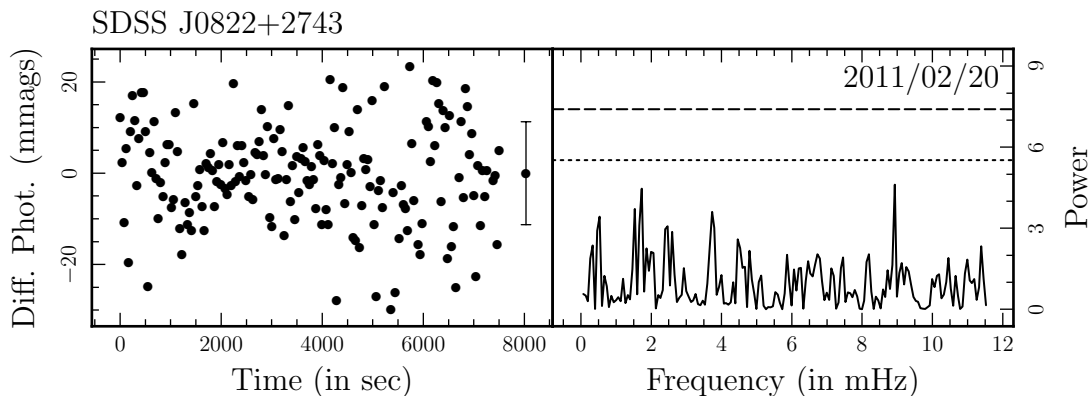


Figure 3.2: The light curve and Lomb-Scargle periodogram for SDSS J0822+2743 for observations taken at WHT/ACAM on 2011 February 20. The dashed (dotted) line in the periodogram represents the 10% (50%) false-alarm probability thresholds given the number of frequency bins.

memory buffer overflow we used the UVIS1-C512A-SUB subarray, a 512×512 pixel sub-section of the CCD. This gave us a $20''.5 \times 20''.5$ field-of-view and a total dead time of 55 s. This setup was used in March 2010 for 4 orbits (6 hours).

3.3.1 SDSS J0822+2743

SDSS J0822+2743 (complete identifier: SDSS J082212.57+275307.4) at SDSS- $g' = 18.3$ mags was observed once using the WHT/ACAM setup on 2011 February 20 using 30 s exposure times for an overall cadence of ≈ 41 s for ≈ 2 hours. We used 10 comparison stars with magnitudes between 16.0–20.0.

No pulsations were detected to a limit of 8 mmags over a frequency range of 1–11 mHz.

This object has a measured $\log g = 6.44 \pm 0.11$ and $T_{\text{eff}} = 8,880 \pm 60$ K which gives a derived model mass of $0.17 M_{\odot}$ (Kilic et al. 2010b). These parameters

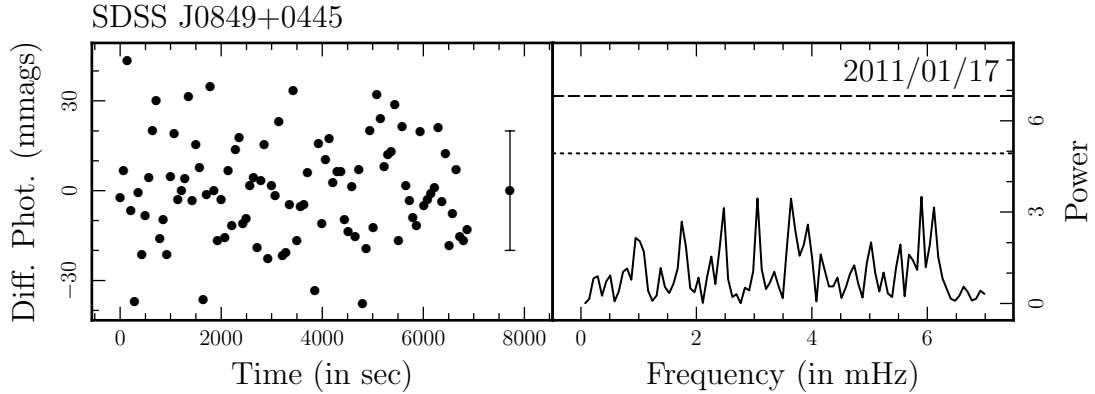


Figure 3.3: The light curve and Lomb-Scargle periodogram for SDSS J0849+0445 for observations taken at WHT/ACAM on 2011 January 17. The dashed (dotted) line in the periodogram represents the 10% (50%) false-alarm probability thresholds given the number of frequency bins.

place it within the high priority target list.

3.3.2 SDSS J0849+0445

SDSS J0849+0445 (complete identifier: SDSS J084910.13+044528.7) at SDSS- $g' = 19.3$ mags was observed once using the WHT/ACAM setup on 2011 January 17 using 60 s exposure times for an overall cadence of ≈ 71 s for ≈ 2 hours. We used 9 comparison stars with magnitudes between 17.0–19.5.

No pulsations were detected to a limit of 15 mmags over a frequency range of 1–7 mHz.

This object has a measured $\log g = 6.23 \pm 0.08$ and $T_{\text{eff}} = 10,290 \pm 250$ K which gives a derived model mass of $0.17M_{\odot}$ (Kilic et al. 2010b).

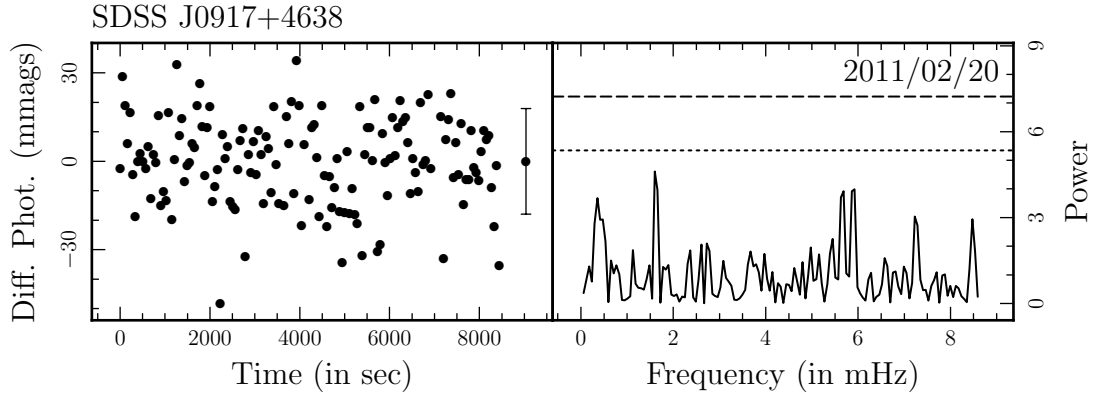


Figure 3.4: The light curve and Lomb-Scargle periodogram for SDSS J0917+4638 for observations taken at WHT/ACAM on 2011 February 20. The dashed (dotted) line in the periodogram represents the 10% (50%) false-alarm probability thresholds given the number of frequency bins.

3.3.3 SDSS J0917+4638

SDSS J0917+4638 (complete identifier: SDSS J091709.55+463821.8) at SDSS- $g' = 18.7$ mags was observed once using the WHT/ACAM setup on 2011 February 20 using 45 s exposure times for an overall cadence of ≈ 56 s for ≈ 2.3 hours. We used 6 comparison stars with magnitudes between 16.1–19.4.

No pulsations were detected to a limit of 11 mmags over a frequency range of 1–8 mHz.

This object has a measured $\log g = 5.48 \pm 0.03$ and $T_{\text{eff}} = 11,288 \pm 72$ K which gives a derived model mass of $0.17M_{\odot}$ (Kilic et al. 2007a).

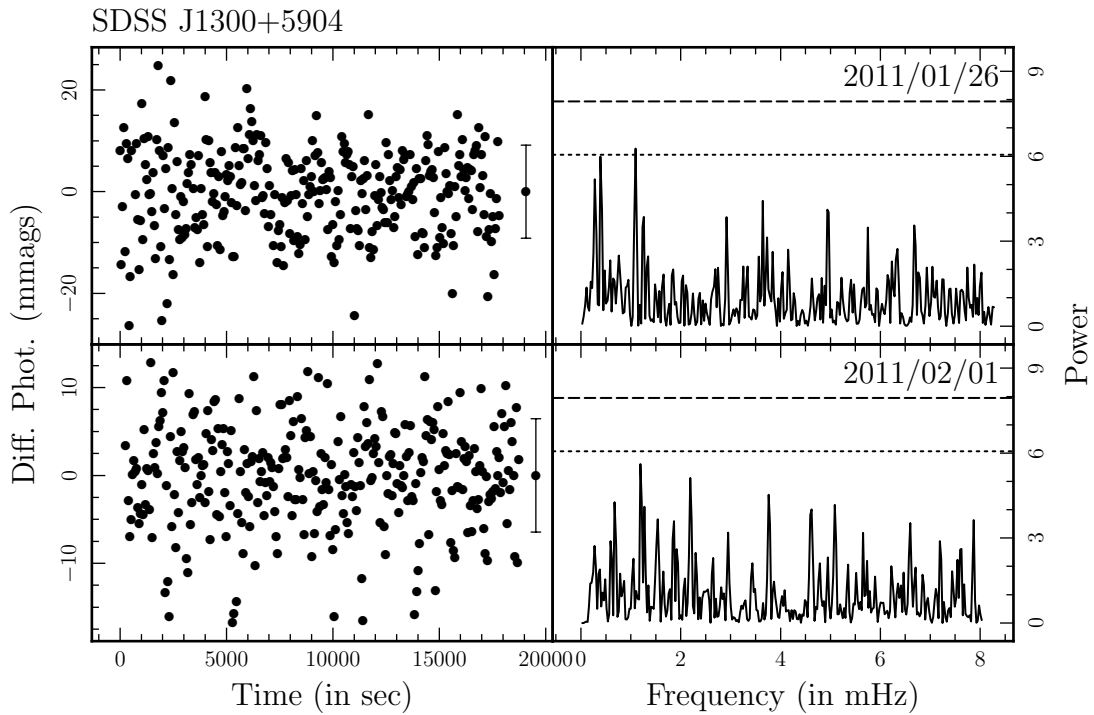


Figure 3.5: The light curves and Lomb-Scargle periodograms for SDSS J1300+5904 for observations taken at BOS/SBIG on 2011 January 26 and 2011 February 1. The dashed (dotted) line in the periodogram represents the 10% (50%) false-alarm probability thresholds given the number of frequency bins.

3.3.4 SDSS J1300+5904

SDSS J1300+5904 (complete identifier: SDSS J130035.22+590415.8) at SDSS- $g' = 15.2$ mags was observed twice using the BOS/SBIG setup on 2011 January 26 and 2011 February 1 using 50 s exposure times for an overall cadence of ≈ 60 s for ≈ 5 hours each night. We used 12 comparison stars with magnitudes between 13.3–16.6.

No pulsations were detected to a limit of 6 mmags over a frequency range of 1–8 mHz for 2011 January 26 and 3 mmags over 1–8 mHz for 2011 February 1.

This object has a measured $\log g = 7.22 \pm 0.02$ and $T_{\text{eff}} = 11,025 \pm 63$ K which gives a derived model mass of $0.3M_{\odot}$ (private communication, Mukremin Kilic).

3.3.5 SDSS J1330+0127

SDSS J1330+0127 (complete identifier: SDSS J133058.19+012706.5) at SDSS- $g' = 18.9$ mags was observed once using the WIYN/OPTIC setup on 2007 May 30 using 90 s exposure times for an overall cadence of ≈ 101 s for ≈ 1.6 hours. We used 5 comparison stars with magnitudes between 16.6–19.0.

No pulsations were detected to a limit of 44 mmags over a frequency range of 1–5 mHz. This observation was plagued by intermittent cirrus clouds and a near full moon creating a high sky background.

This object has a measured $\log g = 5.56 \pm 0.16$ and $T_{\text{eff}} = 8,091 \pm 75$ K (Eisenstein et al. 2006). The SDSS spectra were likely contaminated by a companion

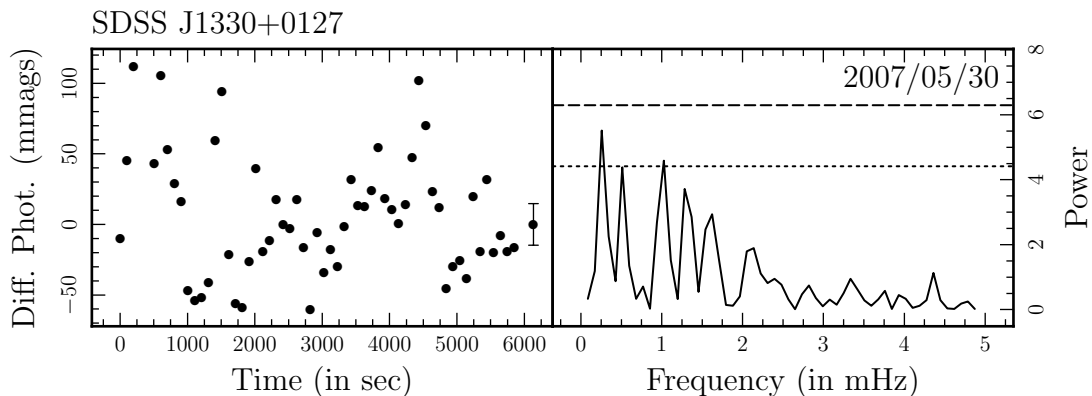


Figure 3.6: The light curve and Lomb-Scargle periodogram for SDSS J1330+0127 for observations taken at WIYN/OPTIC on 2007 May 30. The dashed (dotted) line in the periodogram represents the 10% (50%) false-alarm probability thresholds given the number of frequency bins.

star’s flux. A re-analysis by Silvestri et al. (2006) measured $\log g = 8.1 \pm 0.2$ and $T_{\text{eff}} = 10,617 \pm 452$ K. This object is likely not a He WD and highlights how SDSS parameters can lead one astray.

3.3.6 SDSS J1435+3733

SDSS J1435+3733 (complete identifier: SDSS J143547.87+373338.5) is a partially eclipsing binary system of a C/O WD and M-dwarf discovered by Steinfadt et al. (2008a) and is detailed in Section 5.1. At SDSS- $g' = 17.1$ mags, this object was observed three times using the WIYN/OPTIC setup. It was observed on 2007 May 29 and 31 with exposure times of 15 s for an overall cadence of ≈ 23 s for ≈ 1.5 hours each night. It was observed on 2007 June 1 with exposure times of 40 s for an overall cadence of ≈ 50 s for ≈ 3.8 hours. We used the same 5 comparison stars with magnitudes between 15.9–19. All frames in eclipse were removed for

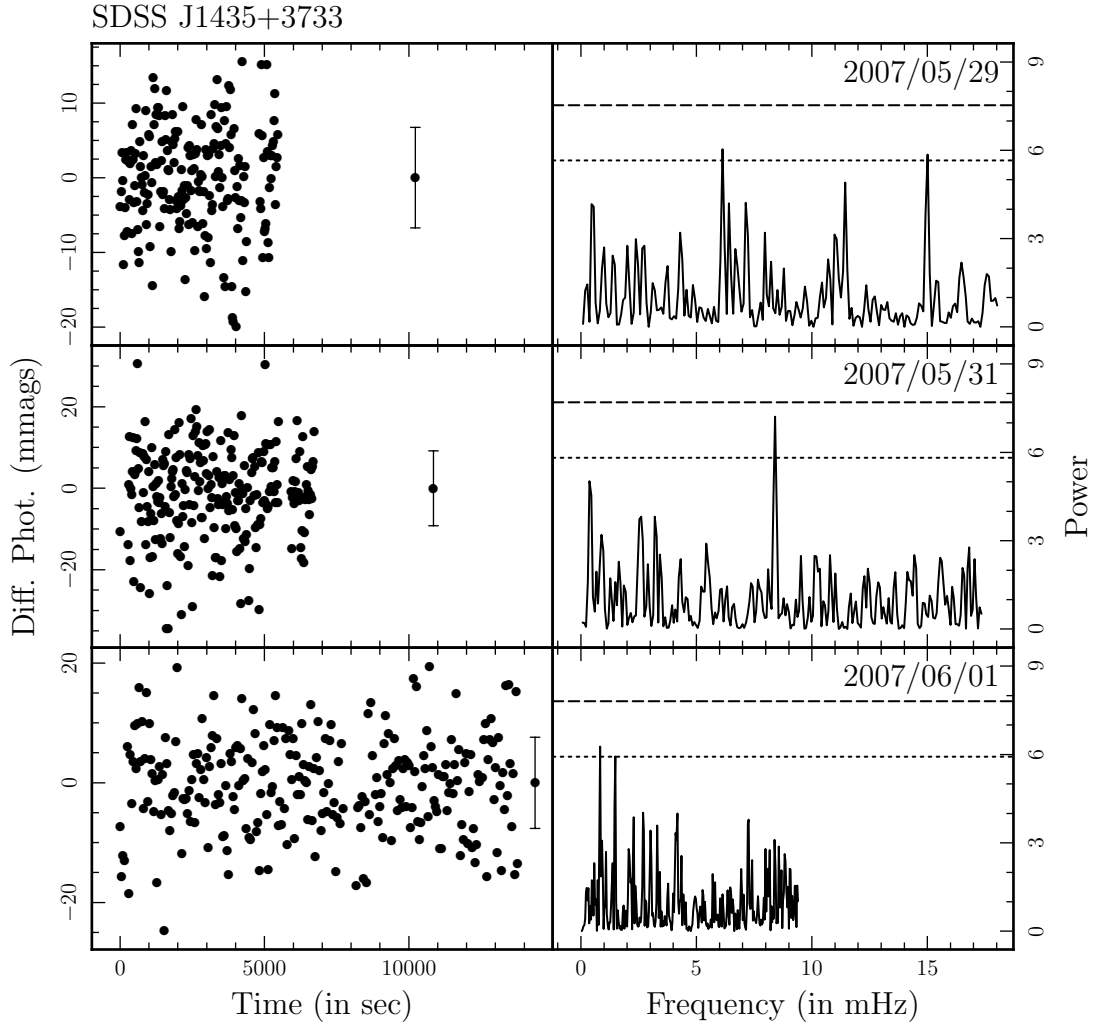


Figure 3.7: The light curves and Lomb-Scargle periodograms for SDSS J1435+3733 for observations taken at WIYN/OPTIC on 2007 May 29, 31, and June 1. The dashed (dotted) line in the periodogram represents the 10% (50%) false-alarm probability thresholds given the number of frequency bins.

pulsation analysis.

No pulsations were detected to a limit of 4 mmags over a frequency range of 1–17 mHz for 2007 May 29, 6 mmags over 1–17 mHz for 2007 May 31, and 4 mmags over 1–9 mHz for 2007 June 1.

This object has a measured $\log g = 6.86 \pm 0.04$ and $T_{\text{eff}} = 11,062 \pm 58$ K (Eisenstein et al. 2006). The SDSS spectra was definitely contaminated by a companion star’s flux (Steinfadt et al. 2008a; Rebassa-Mansergas et al. 2007; Pyrzas et al. 2009). A re-analysis by Rebassa-Mansergas et al. (2007) and Pyrzas et al. (2009) measured $\log g = 7.62 \pm 0.12$ and $T_{\text{eff}} = 12,536 \pm 488$ K which gives a derived model mass of $0.41M_{\odot}$. This object is near the C/O WD and He WD composition boundary and also highlights how SDSS parameters can lead one astray, but that being led astray can also lead to other interesting discoveries!

3.3.7 SDSS J1448+0112

SDSS J1448+0112 (complete identifier: SDSS J144859.39+011243.7) at SDSS- $g' = 19.6$ mags was observed once using the WIYN/OPTIC setup on 2007 May 31 using 60 s exposure times for an overall cadence of ≈ 71 s for ≈ 2 hours. We used 5 comparison stars with magnitudes between 17.3–18.6.

No pulsations were detected to a limit of 34 mmags over a frequency range of 1–7 mHz. This observation was plagued by intermittent cirrus clouds and a near full moon creating a high sky background.

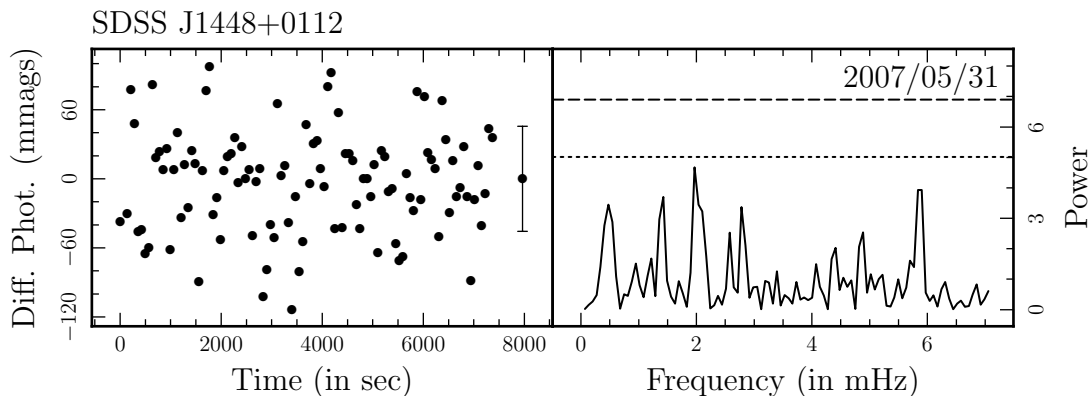


Figure 3.8: The light curve and Lomb-Scargle periodogram for SDSS J1448+0112 for observations taken at WIYN/OPTIC on 2007 May 31. The dashed (dotted) line in the periodogram represents the 10% (50%) false-alarm probability thresholds given the number of frequency bins.

This object has a measured $\log g = 7.31 \pm 0.18$ and $T_{\text{eff}} = 12,142 \pm 486$ K (Eisenstein et al. 2006). There is no indication of spectral contamination by a companion, therefore, these parameters are likely accurate.

3.3.8 SDSS J2049+0005

SDSS J2049+0005 (complete identifier: SDSS J204949.78+000547.3) at SDSS- $g' = 19.7$ mags was observed once using the WIYN/OPTIC setup on 2007 May 31 using 60 s exposure times for an overall cadence of ≈ 71 s for ≈ 3.4 hours. We used 8 comparison stars with magnitudes between 15.9–19.1.

No pulsations were detected to a limit of 21 mmags over a frequency range of 1–7 mHz. This observation was plagued by intermittent cirrus clouds and a near full moon creating a high sky background.

This object has a measured $\log g = 5.48 \pm 0.10$ and $T_{\text{eff}} = 8,660 \pm 144$ K

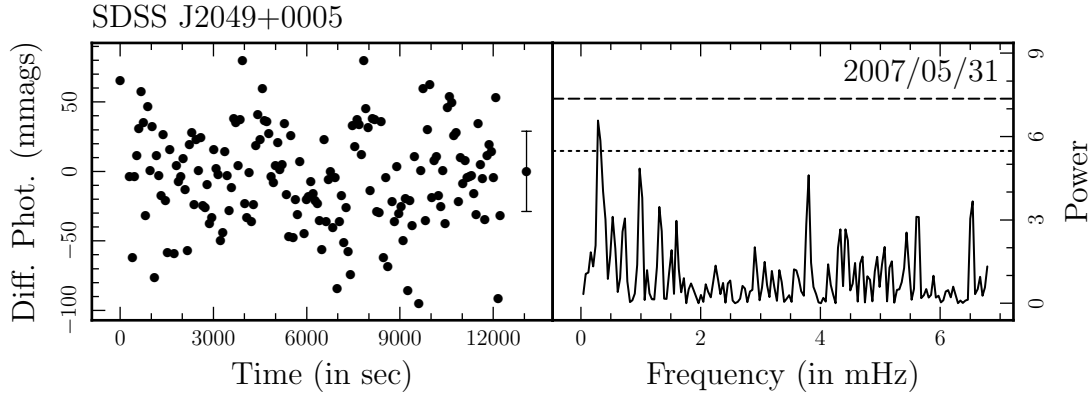


Figure 3.9: The light curve and Lomb-Scargle periodogram for SDSS J2049+0005 for observations taken at WIYN/OPTIC on 2007 May 31. The dashed (dotted) line in the periodogram represents the 10% (50%) false-alarm probability thresholds given the number of frequency bins.

(Eisenstein et al. 2006). Eisenstein et al. (2006) noted multiple minima in their model fits as well as discrepant SDSS- g' band flux compared to best fit models and suggested a $\log g < 5.0$ was likely. Kilic et al. (2007a) confirmed this finding and conclude that this star is likely a distant A2 star. This is yet another instance where SDSS parameters can lead one astray.

3.3.9 SDSS J2240-0935

SDSS J2240-0935 (complete identifier: SDSS J224038.38-093541.3) at SDSS- $g' = 17.6$ mags was observed four times using the P60/P60CCD setup on 2006 August 4, September 19, 25 and December 5 using 30 s exposures for an overall cadence of ≈ 50 – 70 s for ≈ 3.7 , 1.1, 1.0, and 0.9 hours respectively. This object was also observed on 2006 August 17 using 100 s exposures for an overall cadence of ≈ 120 – 140 s cadence for ≈ 4.5 hours, however there are two hour long and half

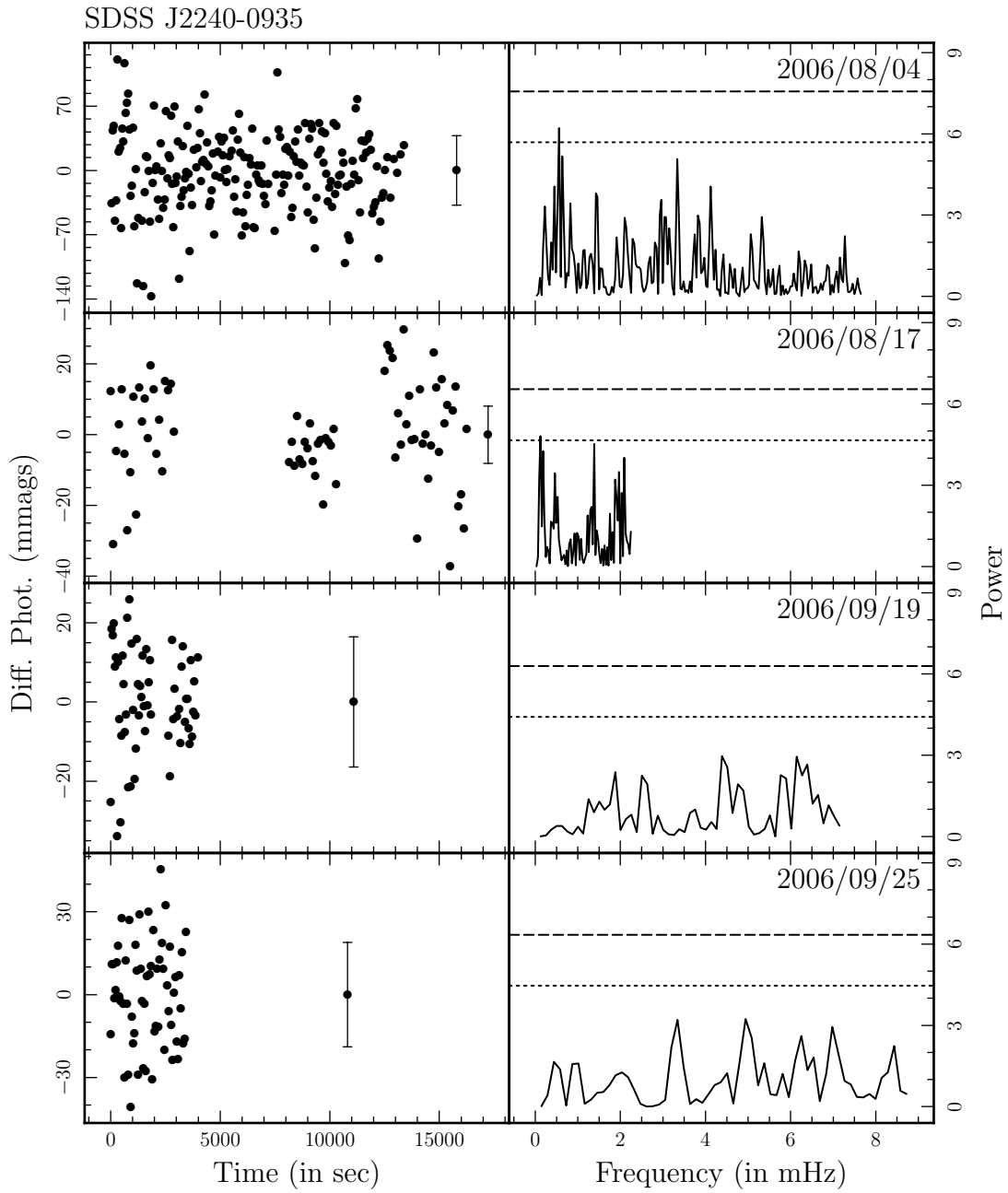


Figure 3.10: The light curves and Lomb-Scargle periodograms for SDSS J2240-0935 for observations taken at P60/P60CCD on 2006 August 4 and 17 and September 19 and 25. The dashed (dotted) line in the periodogram represents the 10% (50%) false-alarm probability thresholds given the number of frequency bins.

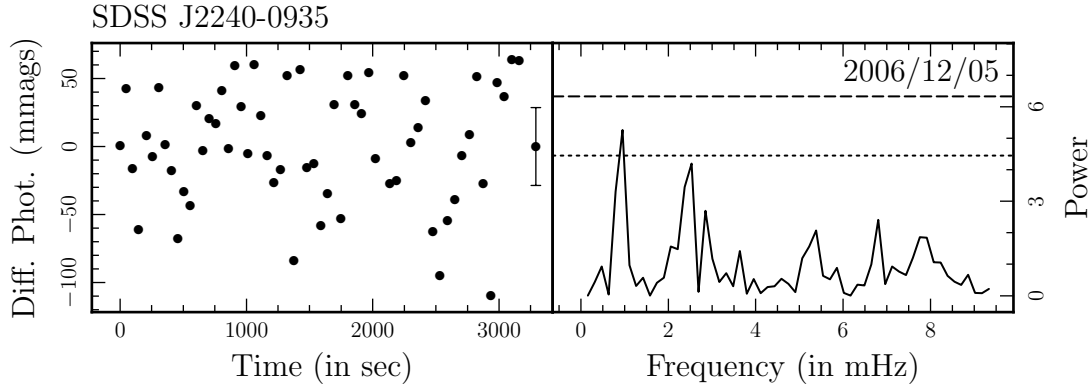


Figure 3.11: Continuation of Figure 3.10 for observations taken on 2006 December 5.

hour long gaps in the time series. We used 5 of the same comparison stars with magnitudes between 16.0–18.5.

No pulsations were detected to a limit of 22 mmags over a frequency range of 1–7 mHz for 2006 August 4, 13 mmags over 1–2.25 mHz for 2006 August 17, 14 mmags over 1–7 mHz for 2006 September 19, 16 mmags over 1–9 mHz for 2006 September 25, and 48 mmags over 1–9 mHz for 2006 December 5.

This object has a measured $\log g = 6.96 \pm 0.09$ and $T_{\text{eff}} = 11,449 \pm 205$ K (Eisenstein et al. 2006). The SDSS spectra were likely contaminated by a companion star’s flux. A re-analysis by Heller et al. (2009) measured $\log g = 7.5$ and $T_{\text{eff}} = 13,000$ K. This object also highlights how SDSS parameters can lead one astray.

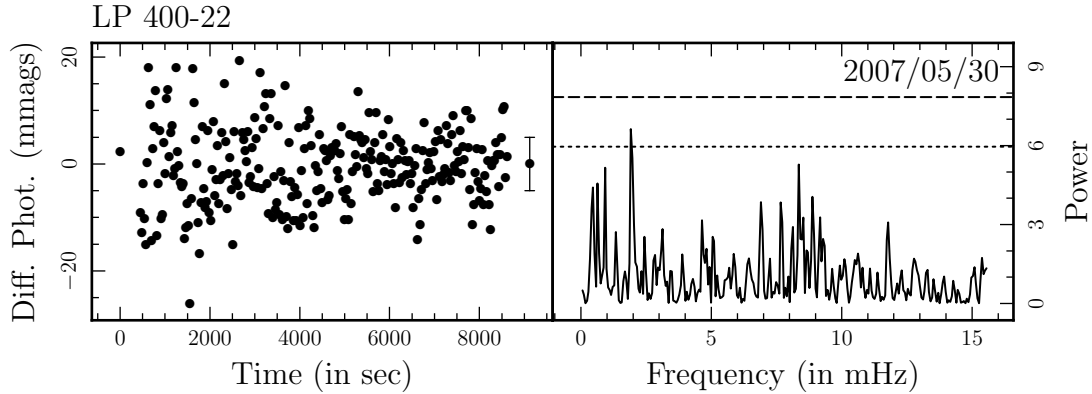


Figure 3.12: The light curve and Lomb-Scargle periodogram for LP 400-22 for observations taken at WIYN/OPTIC on 2007 May 30. The dashed (dotted) line in the periodogram represents the 10% (50%) false-alarm probability thresholds given the number of frequency bins.

3.3.10 LP 400-22

LP 400-22 at $\text{SDSS-}g' = 17.2$ mags was observed one time using the WIYN/OPTIC setup on 2007 May 30 using 20 s exposures for an overall cadence of ≈ 30 s for ≈ 2.4 hours. We used 7 comparison stars with magnitudes between 17.0-18.0.

No pulsations were detected to a limit of 4 mmags over a frequency range of 1-15 mHz.

This object has a measured $\log g = 6.32 \pm 0.08$ and $T_{\text{eff}} = 11,080 \pm 140$ K (Kawka et al. 2006) with a derived model mass of $0.17 M_{\odot}$.

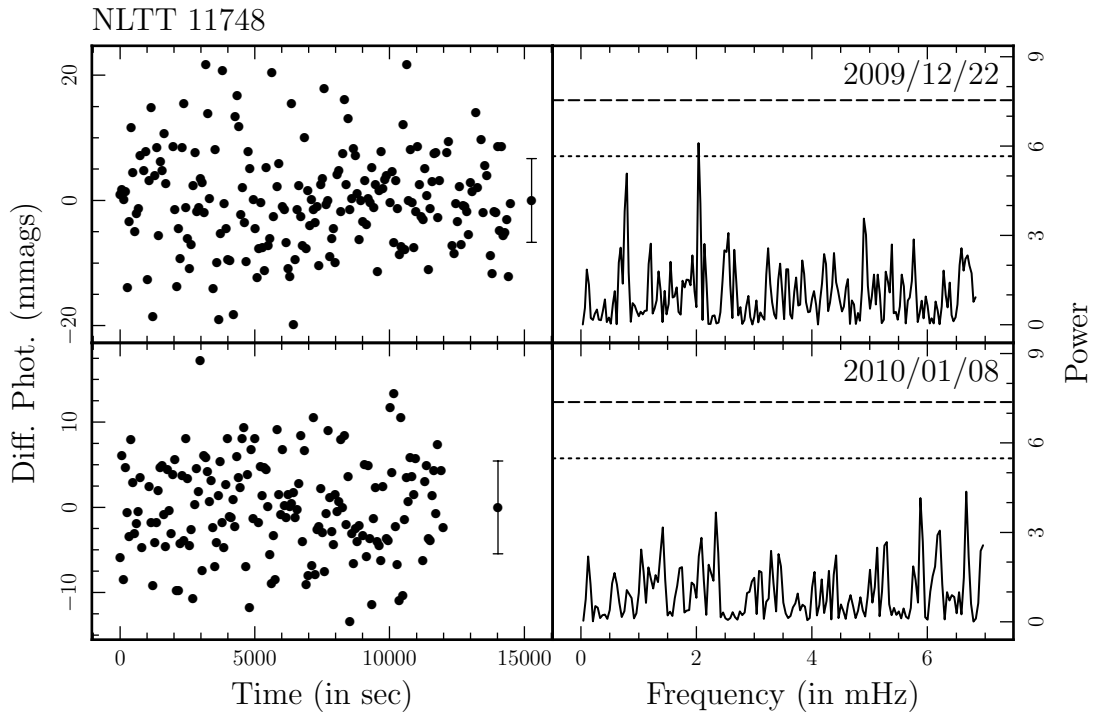


Figure 3.13: The light curves and Lomb-Scargle periodograms for NLTT 11748 for observations taken at FTN/Merope on 2009 December 22 and 2010 January 8. The dashed (dotted) line in the periodogram represents the 10% (50%) false-alarm probability thresholds given the number of frequency bins.

3.3.11 NLTT 11748

NLTT 11748 is the first totally eclipsing detached double white dwarf binary system discovered by Steinfadt et al. (2010b) and is detailed in Section 5.2. At $B = 17.1$ mags, this object was observed two times by the FTN/Merope setup on 2009 December 22 and 2010 January 8 using 45 s exposures for an overall cadence of ≈ 67 s for ≈ 4 hours each night. We used 5 comparison stars with magnitudes between 17.5–18.5.

No pulsations were detected to a limit of 5 mmags over the frequency range of 1–7 mHz on 2009 December 22 and 4 mmags over 1–7 mHz on 2010 January 8.

This object has a measured $\log g = 6.54 \pm 0.05$ and $T_{\text{eff}} = 8,690 \pm 140$ K (Kilic et al. 2010a) with a derived model mass of $0.18M_{\odot}$. In the future, eclipse and radial velocity analysis will produce a high precision measurement of the mass and radius of this object. These parameters place it within the high priority target list.

3.3.12 PSR J1012+5307

PSR J1012+5307 at $V = 19.5$ mags was observed one time using the WHT/ACAM setup on 2010 March 30 using 60 s exposures for an overall cadence of ≈ 71 s for ≈ 2 hours. We used 8 comparison stars with magnitudes between 17.8–19.2.

No pulsations were detected to a limit of 20 mmags over the frequency range

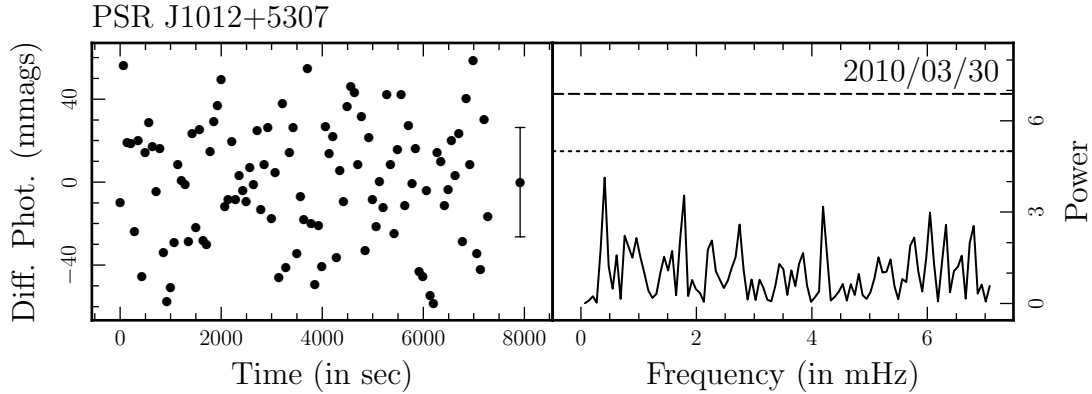


Figure 3.14: The light curve and Lomb-Scargle periodogram for PSR J1012+5307 for observations taken at WHT/ACAM on 2010 March 30. The dashed (dotted) line in the periodogram represents the 10% (50%) false-alarm probability thresholds given the number of frequency bins.

of 1-7 mHz.

This object has a measured $\log g = 6.34 \pm 0.20$ and $T_{\text{eff}} = 8,670 \pm 300$ K with a derived model mass of $0.18M_{\odot}$ (Callanan et al. 1998) and also $\log g = 6.75 \pm 0.07$ and $T_{\text{eff}} = 8,550 \pm 25$ K with a derived model mass of $0.21M_{\odot}$ (van Kerkwijk et al. 1996). Neither of these measurements is obviously superior. Both of these parameters place it within the high priority target list.

3.3.13 PSR J1911-5958A

PSR J1911-5958A at $B = 22.2$ mags was observed one time using the HST/WFC3 setup over 4 orbits on 2010 March 5 using 60 s exposure times for an overall cadence of ≈ 115 s for ≈ 6 hours.

The photometric analysis for this object was uniquely different than all other objects. Due to crowding in the field (PSR J1911-5958A is in a globular cluster)

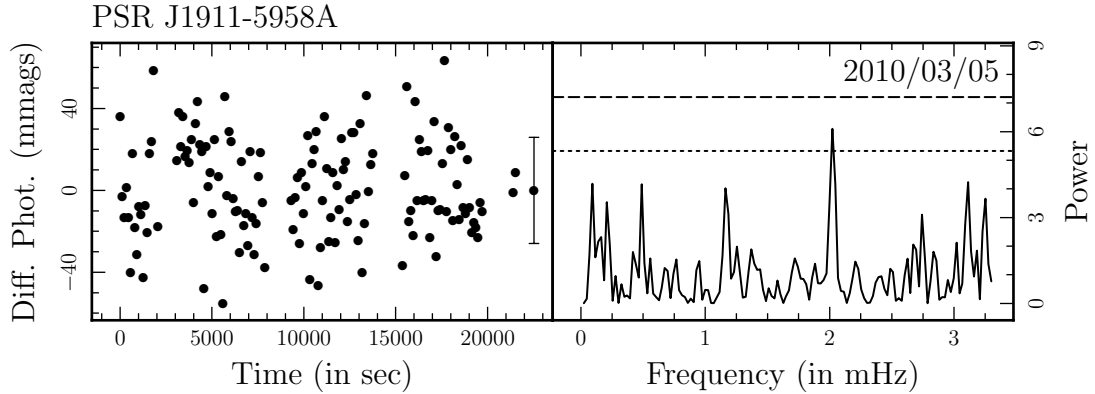


Figure 3.15: The light curve and Lomb-Scargle periodogram for PSR J1911-5958A for observations taken at HST/WFC3 on 2010 March 3. The dashed (dotted) line in the periodogram represents the 10% (50%) false-alarm probability thresholds given the number of frequency bins.

as well as the unique PSF of HST, aperture photometry is not the most precise method. PSF-fitting photometry is ideal since the PSF of the WFC3 instrument is well understood (private communication to Jay Holberg). We used the PSF-fitting software developed by Jay Holberg to extract the photometry from our data. Since most atmospheric and sky effects are nonexistent in space, variable aperture photometry was not required or used. We used 36 comparison stars with magnitudes between 17.5–25.0 to ensure the quality of our photometry.

No pulsations were detected to a limit of 16 mmags over the frequency range of 1–3.25 mHz.

This object has a measured $\log g = 6.44 \pm 0.20$ and $T_{\text{eff}} = 10,090 \pm 150$ K with a derived model mass of $0.18M_{\odot}$ (Bassa et al. 2006a).

Chapter 4

Observations of a Pulsator

¹ In Chapter 3 we observed many candidates for pulsations and discovered no pulsations. In this chapter we detail observations of HS 1824+6000, a low gravity ZZ Ceti that is certainly a C/O-core white dwarf. We carried out these observations shortly after its discovery by Voss et al. (2006) because they reported a gravity and temperature that made it a likely He-core. However, their determination was based on photometric colors, and subsequent spectra by Gianninas et al. (2007) showed it to certainly be a C/O-core white dwarf, albeit lower gravity than average. Motivated by these observations, we compiled a list of all the known (prior to July 2008) ZZ Ceti with spectroscopically determined gravities of $\log g < 8.0$. Using these ZZ Ceti we attempted to compare their observed pulsation periods, in Figure 4.4, in an effort to distinguish a trend that could

¹This chapter is adapted and reproduced from Steinfadt et al. (2008b) with the permission of the Astronomical Society of the Pacific and the University of Chicago Press.

separate potential He core white dwarfs from C/O, a comparison that ultimately failed. However, the list of observed pulsation periods is largely incomplete due to the lack of extensive followup. This makes identifying specific modes (with their spherical eigenvalues) of pulsation impossible except in those situations where week-long continuous observations of objects have been made (e.g. Whole Earth Telescope observations of HL Tau 76 and G117-B15A). Without mode identification, comparison to models is impossible and no detailed constraints on theory can be made.

4.1 Introduction

A detailed asteroseismological study of low-mass WDs with observations of multiple modes of pulsation could provide strong constraints on their interior structure. The mean period spacing of the modes, the rate of change in a mode's period over time, and multiplet splitting of individual modes can provide information on the total mass, spin rate, magnetic field strength, mass of H envelope, and core composition of the WD (Córscico & Benvenuto 2002; Castanheira & Kepler 2008). This has already been theoretically applied to distinguish between C/O and O/Ne core WDs by Córscico et al. (2004). The measured change in an observed mode period in G117-B15 has also been used to constrain significantly the C/O core composition of this object (Kepler et al. 1991, 1995, 2000, 2005b). In Chapter 2 we have developed theory to predict the properties and $T_{\text{eff}}\text{-log } g$

Table 4.1. Properties of HS 1824+6000

	Voss et al. 2006	Gianninas et al. 2007
T_{eff} (K)	$11192 \pm 300^{\text{a}}$	$11380 \pm 140^{\text{b}}$
$\log g$ (dex)	$7.65 \pm 0.10^{\text{a}}$	$7.82 \pm 0.04^{\text{b}}$
m_B (mag)	15.7	15.7
Observed Frequencies (in mHz)		
Voss et al. 2006	$2.6 \pm 0.4, 3.0 \pm 0.9, 3.3 \pm 0.4, 3.4 \pm 0.8$	
This Paper	$2.751190 \pm 0.000010, 3.116709 \pm 0.000006$ $3.495113 \pm 0.000009, 4.443120 \pm 0.000012$	

^aPhotometrically determined.

^bSpectroscopically determined.

locations of pulsating very low mass ($<0.2 M_{\odot}$) He WDs.

We plot a version of the empirical instability strip in Figure 4.1. There is a notable absence of low-mass ($\log g \lesssim 7.67$) WDs within the instability strip. There are a few possible ZZ Ceti stars of this low mass that are not plotted due to the absence of firm spectroscopically determined $\log g$ and T_{eff} measurements (Eisenstein et al. 2006; Voss et al. 2007). Also shown are the He WD cooling tracks of two models for $\approx 0.19, 0.24, 0.40,$ and $0.45 M_{\odot}$ WDs (Althaus et al. 2001; Panei et al. 2007). The difference between these two models at low mass is due to their different H envelope masses. Althaus et al. (2001) used a $1 M_{\odot}$ main sequence star and truncated its evolution up the red giant branch at various stages to produce He WDs of varying masses. Panei et al. (2007) used close binary evolution expectations for main sequence stars of many masses to produce

He WDs of varying masses. These different approaches cause the different remnant H envelope masses that yield a degeneracy in the He WD mass and its position in the $T_{\text{eff}}-\log g$ plane. This degeneracy would be broken in the case of a ZZ Ceti He WD where the pulsation mode spectrum would reveal the H envelope mass.

HS 1824+6000 (hereafter HS 1824, see Table 4.1) was initially observed by Voss et al. (2006) to exhibit pulsations. Their photometrically determined $\log g$ and T_{eff} placed its mass at $\approx 0.40 M_{\odot}$ using the tables of Althaus & Benvenuto (1997). This mass was well within the theoretical expected mass range for He core WDs making it an excellent object to compare and contrast its pulsation frequencies with other C/O core and possible He core DAVs. However, later spectroscopic measurement by Gianninas et al. (2007) determined its mass to be $\approx 0.51 M_{\odot}$, beyond the expected mass range for He core WDs. In §4.2 we discuss our own observations and differential photometry of HS 1824. In §4.3 we apply a Lomb-Scargle Periodogram approach to a non-uniformly sampled time series in order to obtain the pulsation frequencies of HS 1824. In §4.4 we report the results of our observations and analysis.

In §4.5 we compare all observed ZZ Ceti periods with $\log g < 8.0$. It is our hope this will yield a ‘zeroth-order’ approach to He core identification in much the same way T_{eff} and $\log g$ measurements of field WDs identify likely ZZ Ceti stars. No singular distinction is currently present.

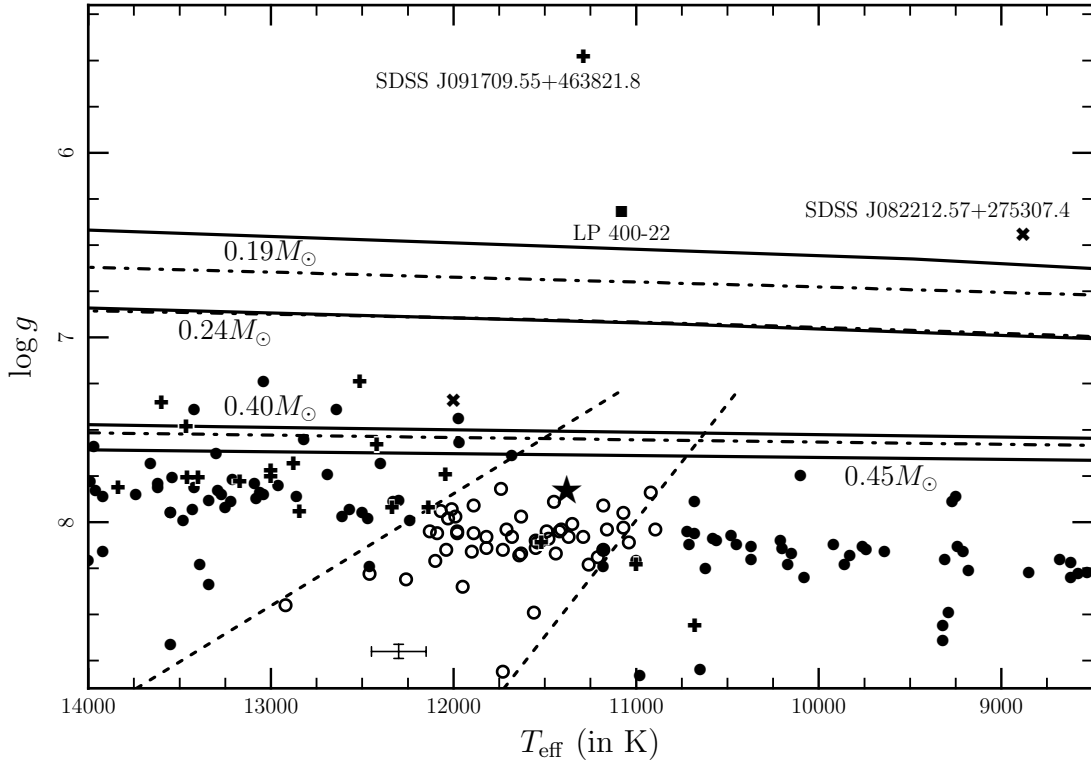


Figure 4.1: The empirical ZZ Ceti instability strip. The circles represent systems for which temporal observations have been performed. Filled circles indicate systems not observed to vary while open circles indicate systems with observed periods. These data are from Bergeron et al. (2004) and Gianninas et al. (2005, 2007). The vertical crosses represent low-mass WDs selected from the SDSS with $\log g$ and T_{eff} redetermined from MMT spectra from Kilic et al. (2007a). The diagonal crosses are from Kilic et al. (2007a) except they are reanalysis of SDSS spectra and are merely candidate low-mass WDs until better spectra can be obtained. The square is LP 400-22 (Kawka et al. 2006; Kilic et al. 2007a). The star is HS 1824+6000 (see Table 4.1, Gianninas et al. 2007). The error bar in the instability strip represents the typical error for measurements within the instability strip. The dashed lines are empirical fits to the instability strip as determined by Gianninas et al. (2007). The solid (Panei et al. 2007) and dash-dotted (Althaus et al. 2001) lines correspond to cooling tracks of He WDs of the labeled mass. The labeled masses correspond to the following model masses (in M_{\odot}) for Panei et al. (2007) and Althaus et al. (2001) respectively: 0.19 to 0.1869 and 0.196, 0.24 to 0.2495 and 0.242, 0.40 to 0.3986 and 0.406, 0.45 to 0.4481 (Panei et al. 2007 only).

4.2 Observations

We observed HS 1824 (see Table 4.1 for properties) on eleven nights from 2006 August to 2006 October using the robotically operated 60-inch (1.52-m) telescope at the Palomar Observatory (Cenko et al. 2006). All observations had 30 second exposures with dead times ranging from 20-40 seconds. To reduce dead time, half the CCD was read out. The large variance in the dead time was due primarily to a technical problem within the automated observing software used to control the telescope. The observing durations varied from 1–3 hours. The primary 2048×2048 pixel, 11'×11', CCD for the robotic Palomar 60-inch was used in all observations with a Gunn *g* filter. We chose the Gunn *g* filter to optimize the ratio of pulsation count amplitude to total stellar counts. It is a known trend that this ratio is larger in bluer filters such as Gunn *g* (Robinson et al. 1982, 1995). A clear filter would not be optimal as it increases the total stellar counts without a comparable increase in pulsation count amplitude, thus reducing this important ratio. Flat fielding, bias subtraction, and sky subtraction were performed within the data pipeline of the Palomar 60-inch Telescope Archive (Cenko et al. 2006). The sky subtraction was done as an inaccurate scalar value and for our purposes was added back into the data and recalculated using standard, more accurate IRAF² tools.

²IRAF (Image Reduction and Analysis Facility) is distributed by the National Optical Astronomy Observatory, which is operated by the Association of Universities for Research in Astronomy, Inc., under contract with the National Science Foundation. <http://iraf.noao.edu>

4.2.1 Data Reduction

We used the IRAF package VAPHOT (Deeg & Doyle 2001) to dynamically determine optimum aperture sizes as a function of seeing for our photometry. Given a characteristic frame for each night, VAPHOT calculates an optimized aperture using a PSF for each star that maximizes the signal to noise within the aperture. This optimized aperture is then found as a function of the seeing. Then, for a time series of frames, VAPHOT calculates the seeing value for each individual frame and scales the optimized apertures accordingly. Finally, all aperture information is input into the standard IRAF task *phot* which calculates counts within the optimized aperture along with background noise counts measured in an annulus just beyond the optimized aperture. For each night of observation, 21 comparison stars were selected ranging $g = 12 - 16$ mag and along with the program star, counts and background information were extracted using the VAPHOT task. Additionally, the exposure start times for all frames of observation were converted to barycentric Julian dates.

The uncertainty of this photometry for each aperture is given by;

$$\sigma_{CCD}^2 = c + n_{bins} \left(1 + \frac{n_{bins}}{n_{sky}} \right) (N_S + N_R^2 + N_D), \quad (4.1)$$

(Howell 2006), where c is the number of integrated source counts in photons, n_{bins} is the aperture area calculated by VAPHOT in pixels, n_{sky} is the area of the annulus used to calculate the background information in pixels, N_S is the background counts per pixel, N_R is the read noise of the CCD in counts per pixel,

and N_D is the dark current in counts per pixel. We do not include the digitization error as it is significantly less than our value for the gain. For our observations, c was $\approx 4 \times 10^4$ counts for HS 1824 and $\approx 10^4$ – 10^6 counts for the comparison stars, while $N_S \approx 40 - 600$ counts, $N_R^2 \approx 25 - 60$, and $N_D \ll 1$ counts for $t_{int} = 30$ sec integrations.

Additional uncertainty arises from atmospheric variability on spatial scales of the CCD field of view. Scintillation is a dimensionless measure of the flux variations of a source observed through a finite aperture (our telescope) due to fluctuations in the refractive index of the atmosphere caused by temperature changes. Young’s formulation (Young 1967) of Reiger’s theory of scintillation (Reiger 1963) gives $s_{scint} = S_0 d^{-2/3} X^{3/2} e^{-h/h_0} \Delta f^{1/2}$, where $S_0 = 0.09$ is a constant (Young 1967), $d = 152$ cm is the mirror diameter, X is the airmass, $h = 1706$ m is the Palomar Observatory altitude, $h_0 = 8000$ m is a constant (Young 1967), and $\Delta f = 1/t_{int}$. The formal photometric error for each star in each frame is,

$$\sigma^2 = \sigma_{CCD}^2 + s_{scint}^2 c^2, \quad (4.2)$$

which determines the count level, c , at which scintillation noise becomes comparable to Poisson noise. This occurs at 9×10^5 counts at airmass 1.15 and 2×10^5 counts at airmass 2.0. Compared to the total formal error given by Equation (4.2), scintillation accounts for 10 – 40% of the error depending upon the airmass (higher airmass account for higher percentages). Therefore, we are mostly limited by Poisson counting statistics, but scintillation can become significant at higher

airmass.

4.2.2 Differential Photometry

Since the atmosphere is constantly changing, differential rather than absolute photometry was used in the construction of our light curves. We used an ensemble of comparison stars to reduce the noise level inherent in any single comparison star. We used the weighting scheme detailed in Sokoloski et al. (2001) inspired by Gilliland & Brown (1988). For our target star we define;

$$x(i) = A \frac{c_p(i)}{\sum_{m=1}^K w_m c_m(i)}, i = 1, \dots, N, \quad (4.3)$$

$$\sigma_x^2(i) \approx \left[\frac{\sigma_p(i)}{c_p(i)} \right]^2 + \frac{\sum_{m=1}^K [w_m \sigma_m(i)]^2}{\left[\sum_{m=1}^K w_m c_m(i) \right]^2}, \quad (4.4)$$

$$A^{-1} = \frac{1}{N} \sum_{i=1}^N \frac{c_p(i)}{\sum_{n=1}^K w_n c_n(i)}, \quad (4.5)$$

$$w_m = \frac{\sum_{i=1}^N c_m(i)}{\sum_{i=1}^N \sigma_m^2(i)}, \quad (4.6)$$

where $x(i)$ is the count ratio for the i 'th image, $c_p(i)$ and $\sigma_p(i)$ are the background-subtracted counts and uncertainty of the program star, $c_m(i)$ and $\sigma_m(i)$ are the background-subtracted counts and uncertainty for the m 'th comparison star in the i 'th image, K is the number of comparison stars, and N is the total number of frames in the light curve. The weights of the m 'th comparison star, w_m , are the same for every image, while A is a normalization factor that gives $x(i)$ meaning

such that,

$$\Delta c_p(i) = \bar{c}_p (x(i) - 1), \quad (4.7)$$

where \bar{c}_p is the mean background subtracted counts of the program star and $\Delta c_p(i)$ is the difference in the total counts of the i th frame compared to the mean counts of the program star for that night.

4.3 Lomb-Scargle Timing Analysis

The robotically controlled Palomar 60-inch presents a few challenges for time domain observations. First is the variable dead time of 20-40 seconds after a 30 second exposure. Second, the automated observing program sometimes places a higher priority on other targets, thus placing temporal gaps in our time series. While data gaps can be addressed in discrete Fourier analysis, large variations in timing is a much more difficult problem that we address via the Lomb-Scargle periodogram approach.

Scargle (1982) defines a periodogram as a function of the angular frequency ω (in rad s⁻¹) as follows;

$$P_x(\omega) = \frac{1}{2} \left(\frac{\left[\sum_{i=1}^N x(t_i) \cos(\omega(t_i - \tau)) \right]^2}{\sum_{i=1}^N \cos^2(\omega(t_i - \tau))} + \frac{\left[\sum_{i=1}^N x(t_i) \sin(\omega(t_i - \tau)) \right]^2}{\sum_{i=1}^N \sin^2(\omega(t_i - \tau))} \right), \quad (4.8)$$

$$\tan(2\omega\tau) = \frac{\sum_{i=1}^N \sin(2\omega t_i)}{\sum_{i=1}^N \cos(2\omega t_i)}, \quad (4.9)$$

where $x(t_i)$ is $\Delta c_p(i)$ from our differential photometry (§4.2.2) and t_i is the start time in seconds of the i 'th frame. Further considerations by Scargle (1982) and Horne & Baliunas (1986) showed that the probability distribution of power at frequency ω (with Gaussian white noise) is $\text{Prob}(P(\omega) > z) = e^{-z}$ when the periodogram is normalized as

$$P(\omega) = P_x(\omega)/\sigma^2, \quad (4.10)$$

where σ^2 is the total measured variance of $x(t)$ over the entire time series. Horne & Baliunas (1986) also showed that for data with periodic signals, the normalization factor remains the total variance of the raw data with the signal present.

The $\exp(-z)$ probability distribution quantifies the significance of any signal seen within the periodogram, allowing us to find the probability that the noise (presumed to be independent and normal) would, by itself, produce a power of z . This allows us to generate a *false-alarm probability* that states if we scan M independent frequencies then the probability that the intrinsic noise produces a

power greater than z in any one of the frequency bins is

$$\text{Prob}(\text{Any Power} > z) = 1 - (1 - e^{-z})^M. \quad (4.11)$$

A periodic signal is thus significant to 90% over all M sampled frequencies if the false-alarm probability is 10%. Since our noise is not exactly normally distributed due to the presence of unresolved pulsations which assure some correlation between data point the precise significance may be slightly lower than this. However, this will not have any consequence for our results.

All 21 comparison stars would not produce the most stable comparison set. To determine the optimum ensemble of comparison stars for a given observing run, every comparison star was compared to all other comparison stars one at a time by calculating light curves (§4.2.2) and periodograms (§4.3). Such an analysis reveals consistent frames where a comparison star has a count value much beyond the scatter of the normal light curve. In these cases, that frame and comparison star were analyzed using standard IRAF tasks to determine what caused the contamination (e.g. cosmic ray strike, drift into bad pixel due to poor guiding). Almost always, these comparison stars were then excluded from the optimum comparison star ensemble for that night only. The periodograms found those comparison stars with consistent frequency content due to possible intrinsic variability. These comparison stars were also excluded. Individual frames were excluded when the program star was contaminated by cosmic ray strikes, or the entire frame was affected by a high background level or poor seeing.

Comparison stars were also excluded when color-airmass effects could not be adequately removed via a de-trending second order polynomial. This was done by comparing all comparison stars to HS 1824 individually and looking for high levels of noise in the lowest frequency domain of the periodogram. De-trending with a second order polynomial is acceptable in our situation as the periods of pulsation are much shorter than the hours time-scale it takes for changing color-airmass. The resulting optimum comparison star ensemble was then used to compute the HS 1824 differential light curve (§4.2.2), which was de-trended through the second order polynomial fitting, and the final light curve processed through the periodogram (§4.3).

4.4 Final Light Curves and Periodograms: Results

Using Equation (4.11), we determined an observed power to be significant in any periodogram if the probability was greater than 90% (*false-alarm* probability less than 10%) over all sampled frequencies. A summary of all significant frequencies is in Table 4.2, where the frequency uncertainty reported is the separation of the frequency bins in the periodogram. Figure 4.2 shows the differential light curves and periodograms for our four longest data sets. The data from the four longest observations allow us to construct a weighted average to arrive at

Table 4.2. Observation Dates and Pulsation Results for HS 1824+6000

Date (UT) YYMMDD	2.7 (Ampl.) mHz (mmag)	3.1 (Ampl.) mHz (mmag)	3.5 (Ampl.) mHz (mmag)	4.4 (Ampl.) mHz (mmag)	Obs. Length ^a hr	Number of Frames ^a	Number of Comp. Stars ^b
060821	-	-	-	4.45 ± 0.10 (9.7)	0.8	56	12
060824	2.68 ± 0.16 (8.1)	3.15 ± 0.16 (9.1)	-	-	0.9	59	13
060827	-	3.08 ± 0.15 (10.4)	-	-	0.9	59	14
060830	-	3.14 ± 0.13 (6.2)	-	4.44 ± 0.13 (5.9)	1.1	69	11
060903	-	-	-	-	1.0	68	11
060906	-	3.13 ± 0.14 (7.8)	-	-	1.0	69	14
060909	-	3.15 ± 0.12 (11.8)	-	-	1.2	66	10
061009	2.74 ± 0.05 (5.6)	3.13 ± 0.05 (7.5)	-	4.45 ± 0.05 (7.0)	2.8	137	9
061016	-	3.10 ± 0.03 (8.1)	3.53 ± 0.03 (5.3)	-	3.5	129	9
061019	2.73 ± 0.03 (7.4)	3.14 ± 0.03 (7.2)	-	-	4.0	164	7
061021	-	3.10 ± 0.09 (8.9)	3.55 ± 0.09 (5.6)	-	1.5	90	11
Weighted Average over Four Longest Nights							
...	2.73 ± 0.03	3.12 ± 0.02	3.53 ± 0.03	4.45 ± 0.05
Combined Data Set (See §4.4)							
...	2.751190 ±0.000010	3.116709 ±0.000006	3.495113 ±0.000009	4.443120 ±0.000012

^aIncludes only data used in analysis; excludes contaminated frames (i.e. cosmic ray in program star, clouds, poor seeing, etc.).

^bSee §4.4 for discussion on the inclusion and exclusion criteria for comparison stars. There was a maximum 21 comparison stars possible.

Note. — ‘-’: denotes the frequency was not observed to the required significance level of 90%

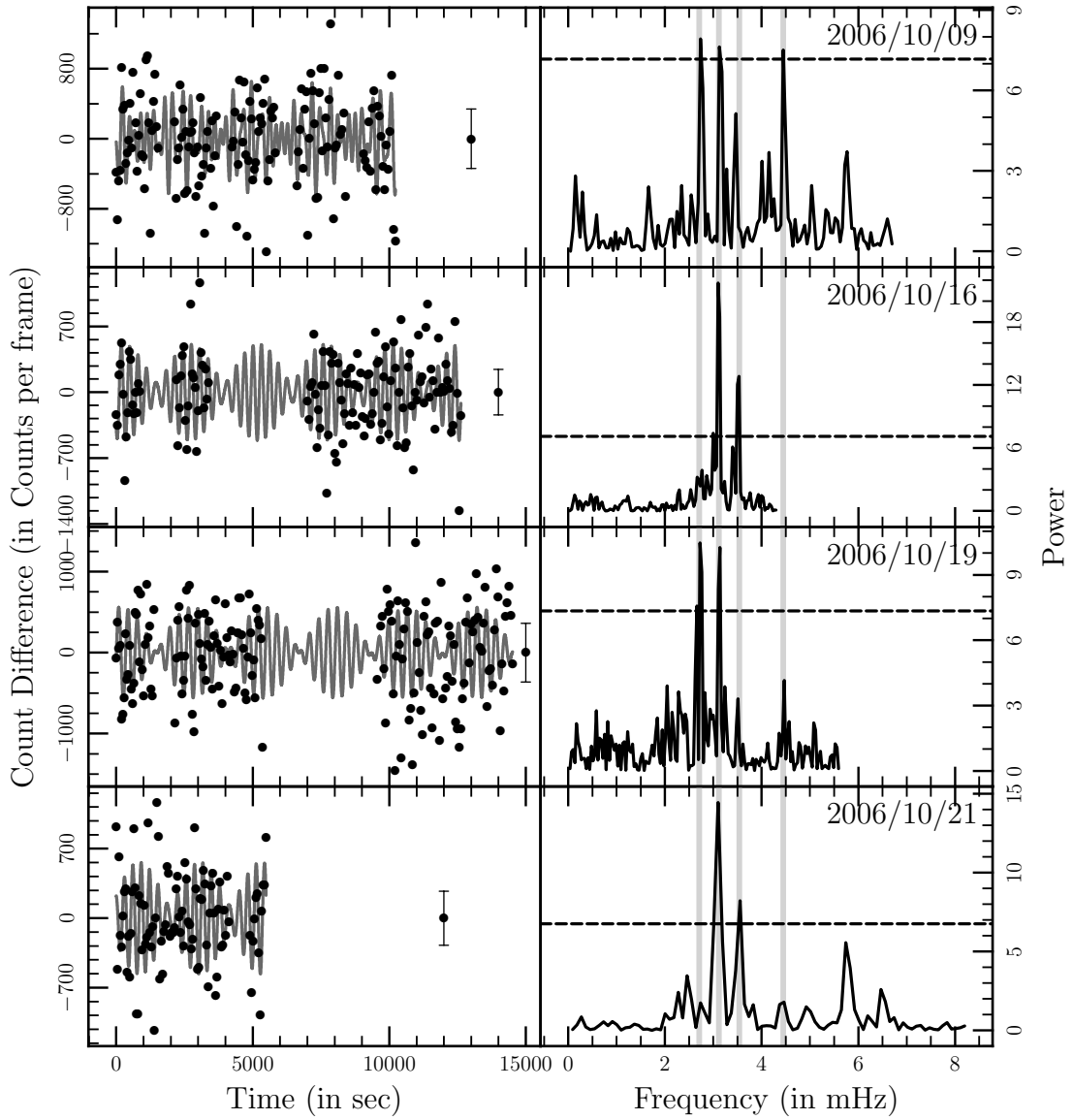


Figure 4.2: Left Panels: Light curves (see §4.2.2) plotted as count difference compared to mean counts of the program star on that night versus time. Counts refers to the total counts accumulated within the 30 second exposure. A least-squares fit of sinusoidal functions to the observed significant frequencies is also plotted. Points detached from data sets denote typical error bars. Right Panels: Lomb-Scargle Periodograms. (see §4.3) Dashed lines denote power level required for 90% significance. Gray vertical lines show locations of 2.7, 3.1, 3.5, and 4.4 mHz frequencies.

2.73 ± 0.03 mHz (366 sec), 3.12 ± 0.02 mHz (321 sec), 3.53 ± 0.03 mHz (283 sec), and 4.45 ± 0.05 mHz (225 sec). The 2.7 and 4.4 mHz frequencies are confirmed in three nights, the 3.5 mHz frequency in two nights, and the 3.1 mHz frequency in nine nights. Excess power is often observed in these frequencies on other nights although not to the required significance level (90%).

Our final analysis combined all eleven nights of data into one data set. Sky conditions were not the same for all nights, so the individually reduced data as described above was used and then combined. Barycentric Julian dates must be used in this analysis as changes in the Earth's orbital position in the solar system can account for as much as a eight seconds per day change in light arrival time. This composite data set was spectrally analyzed using the Lomb-Scargle periodogram and the result is plotted in Figure 4.3.

All four detected frequencies are recovered to our 90% confidence, however, the imprint of our window function makes it difficult to determine any gains in precision over the individual nights. To address this concern we used a method of least-squares fitting of sinusoids at all four detected frequencies, allowing a single frequency to vary while fixing the remaining frequencies and minimizing χ_{fit}^2 . The old detected frequency was then replaced with this more accurate frequency. This was done for all four frequencies and repeated recursively until all four frequencies no longer changed values significantly. This method gives us accurate determinations of the frequencies, amplitudes, and phases of the four detected frequencies.

To determine the precision of these new measurements we used a more robust χ_{fit}^2 minimization technique allowing all parameters to vary, now including the frequencies. The inherent non-linearity of the fitting model requires the use of the Levenberg-Marquardt method which is given the accurate determinations of the frequencies, amplitudes, and phases of the four detected frequencies as a starting point. This method incorporates the calculation of the covariance matrix which in turn gives us a measure of the precision of each parameter of the best-fit model. This yielded more precise values of 2.751190 ± 0.000010 mHz, 3.116709 ± 0.000006 mHz, 3.495113 ± 0.000009 mHz, and 4.443120 ± 0.000012 mHz, more than a 1000 fold increase in precision.

This new fitted sinusoidal function was then subtracted from the data and its periodogram can be found in the lower panel of Figure 4.3. The striking features of this de-sigaled periodogram is the remainder of two signals of significant power near 4.44 mHz and 5.75 mHz. However, the false-alarm probability arguments are not valid in a data set where signals have been removed artificially. Interestingly, the excess power near 4.44 mHz is in a frequency bin significantly offset from our reported detected frequency. If we treat both of these left over frequencies as real pulsation frequencies and use our algorithm, we find that there may exist two more detected frequencies at 4.450643 ± 0.000017 mHz and 5.755451 ± 0.000018 mHz. The existence of these frequencies is questionable because neither frequency had enough power to reach our required false-alarm significance level in the full

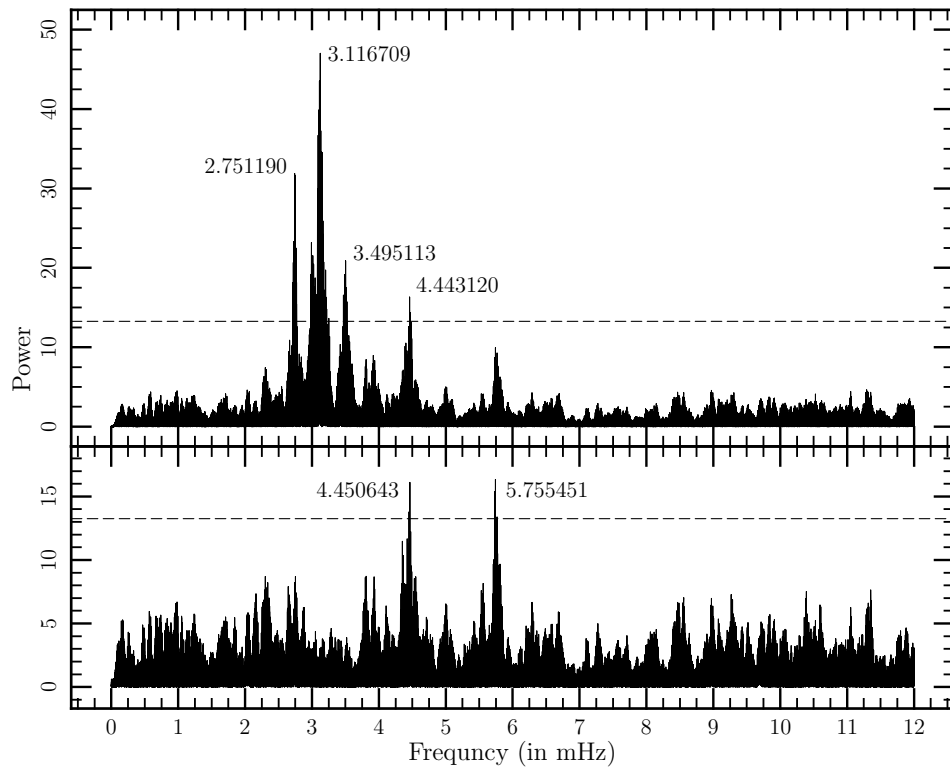


Figure 4.3: Top Panel: Lomb-Scargle Periodogram for combined data set (see §4.4). Bottom Panel: Lomb-Scargle Periodogram for de-sigaled (using only the four significant to 90% detected frequencies) data set . For both plots the dashed lines denote power level required for 90% significance.

data set. Additionally, the new 4.450643 mHz frequency is entirely lost within the window function around the original detected frequency. When we de-signal the entire data set with the least-squares fitted sinusoidal function including the six frequencies, the resulting periodogram no longer contains any frequency bins with significant power. The existence of these two pulsation frequencies is uncertain until better data with higher frequency sampling and more amicable window function can be obtained.

4.5 Conclusions

We have successfully detected four pulsation frequencies (periods), 2.751190 mHz (363.479 sec), 3.116709 mHz (320.851 sec), 3.495113 mHz (286.114 sec), and 4.443120 mHz (225.067 sec), in multiple observations of HS 1824+6000. There are also two possible pulsation frequencies (periods) at 4.450643 mHz (224.687 sec) and 5.755451 mHz (173.748 sec). With these periods of pulsation in HS 1824, the question remains if it, or other low gravity systems, can be empirically distinguished from the normal C/O core ZZ Ceti population. To answer this we compiled all known ZZ Ceti stars with published pulsation periods and spectroscopically measured gravities of $\log g < 8.0$. This search resulted in 30 systems including HS 1824. In Figure 4.4 we plot all reported periods for these 30 systems. Across all of these ZZ Ceti systems there exist many reported pulsation periods ranging from 100 – 1400 sec. However, it is apparent that better than half of the

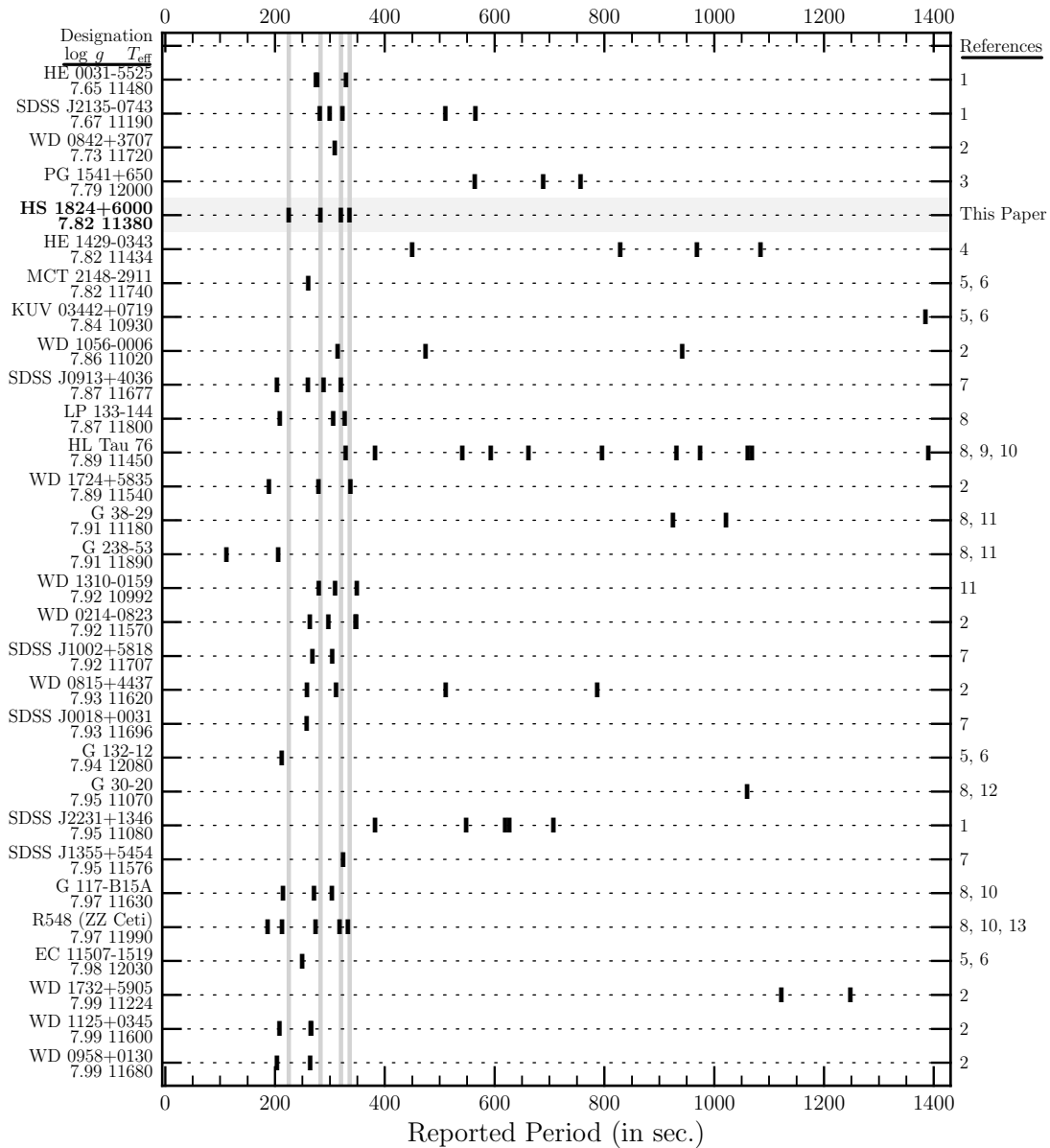


Figure 4.4: Spectrum of reported pulsation periods for published ZZ Ceti systems with spectroscopically determined $\log g < 8$. HS 1824 is highlighted in gray with its four observed period locations marked with four vertical lines. Some marks represent more than one (very closely spaced) observed pulsation period, see references for details. HL Tau 76 lists only the verified independent pulsation modes of Dolez et al. (2006). Several systems listed here are not included in Figure 4.1 as their $\log g$ and T_{eff} measurements are not of sufficient precision. References: 1 - Castanheira et al. 2006, 2 - Mukadam et al. 2004a, 3 - Vauclair et al. 2000, 4 - Silvotti et al. 2005, 5 - Gianninas et al. 2007, 6 - Gianninas et al. 2006, 7 - Mullally et al. 2005, 8 - Bergeron et al. 2004, 9 - Dolez et al. 2006, 10 - Bergeron et al. 1995, 11 - Kepler et al. 2005a, 12 - Mukadam et al. 2002, 13 - Mukadam et al. 2003.

reported periods reside within the range of 150 – 400 sec. The four periods of HS 1824 are indistinguishable from the rest of this set of ZZ Ceti stars. Further, there does not appear to be any distinction between the two low-mass ($\log g \lesssim 7.67$) systems (HE 0031-5525, SDSS J2135-0743, Castanheira et al. 2006) and the rest of the set. With this current set of data it appears that this empirical analysis of reported pulsation periods is not sufficient to distinguish a suspected He core from a normal C/O core. However, HE 0031-5525, and SDSS J2135-0743 (Castanheira et al. 2006) are very close to the boundary of He and C/O core WDs and within the errors of their $\log g$ measurements may be C/O cores.

It remains uncertain as to what degree this period spectrum comparative analysis can succeed. There are two primary differences between He and C/O core WDs that affect g-modes: the contrast in mean molecular weights in their cores, and the one fewer stratified layer in a He core object. G-modes penetrate deeply into the core, so that differences in the Brunt-Väisälä profile there (due to the mean molecular weight; see Deloye & Bildsten 2002) significantly change the resulting mode period spectrum (Arras et al. 2006). The stratified layers of material within the WD also affects how different pulsation modes are trapped, driven, and excited (Córscico & Benvenuto 2002; Arras et al. 2006). He core WDs possess only two zones of He and H, while C/O core WDs possess the additional zone of C/O. Qualitatively, both of these differences would produce differences in the mode period spectra. Chapter 2 investigates in detail these issues.

Most reported systems in Figure 4.4 were found in observational campaigns looking only for pulsations in an effort to constrain the ZZ Ceti instability strip. In most cases, no attempt was made to distinguish observed pulsation periods as independent modes, as opposed to linear combinations of modes. This analysis was neglected in large part due to the lack of extensive follow up. Our observations of HS 1824 showed most single nights of data contain the pulsations of one specific period and it was a rarity to find a night of data with multiple pulsation periods. Ideally, very long gapless observations on the order of several days would address these problems very well. These observations could be obtained through the use of telescope networks such as the Whole Earth Telescope³ as was done with HL Tau 76 (Dolez et al. 2006) and G117-B15A (Kepler et al. 1991, 1995) and the Las Cumbres Observatory Global Telescope⁴. We look toward future, more detailed observations of many low-mass and normal-mass ZZ Ceti stars to help provide a measurable distinction between He and C/O core compositions in WDs.

³<http://www.physics.udel.edu/darc/wet>

⁴<http://www.lcogt.net>

Chapter 5

Discoveries of Two Eclipsing Binary Systems

Formation theories of helium white dwarfs predict that a large fraction should be in binary systems (especially those $<0.2M_{\odot}$). The common envelope phases in which helium white dwarfs are born trade orbital angular momentum and energy to eject the envelope, a process that tightens these binaries to orbital periods short enough that gravitational wave emission will eventually bring them into contact. For these pre-contact systems, the probability of seeing an eclipse can be quite high, reaching 15% for $P_{\text{orb}} = 1$ hr. The eclipses themselves vary in properties according to the possible companions in these systems. They can be short, durations of a few minutes, and shallow or deep in fractional flux, depths of a few percent to near total. A fortuitous side-effect of the pulsation search we

performed in Chapter 3, with a cadence $\lesssim 60$ s and precision $\approx 1\%$, is that we are very sensitive to these eclipses. In fact, we have discovered two unique eclipsing binary systems. In Section 5.1 we detail our discovery of a partially eclipsing low-gravity C/O white dwarf in a binary with an M-dwarf star, SDSS J1435+3733. Our analysis lacks radial velocity data and the partially eclipsing nature of this system hinders our ability to constrain the system and component properties. Fortunately, Pyrzas et al. (2009) have followed up our discovery and constrain the WD to be $0.48\text{--}0.53 M_{\odot}$ and $0.0144\text{--}0.0153 R_{\odot}$. In Section 5.2, we present our discovery of the first eclipsing detached double white dwarf system, NLTT 11748, a system with both He and C/O white dwarfs. Our data already constrain the properties of the He white dwarf, but ongoing and future observations of this system will allow us to make the first model independent constraints of a He white dwarf.

5.1 Discovery of the Partially Eclipsing White Dwarf Binary SDSS J143547.87+373338.5

¹ Eclipsing binary systems offer unique opportunities for precise measurements of stellar properties. With full radial velocity and light curves (commonly from eclipsing double-lined spectroscopic binaries), the masses and radii of both com-

¹This section is adapted and reproduced from Steinfadt et al. (2008a) with the permission of the American Astronomical Society.

ponents are measured to very high precision and accuracy.

We discovered that the $u' = 17.7$ and $g' = 17.1$ mag binary SDSS J143547.87+373338.5 (hereafter J1435, Eisenstein et al. 2006) undergoes a partial eclipse of the WD by its low-mass companion with a period of 3 hrs and a transit time of ≈ 480 sec. The eclipsing M dwarf secondary is expected to contribute $\lesssim 4\%$ in the blue band BG-39 filter. Measurements by Gänsicke et al. (private communication, Rebassa-Mansergas et al. 2007) give an accepted range of WD masses of $0.35\text{--}0.58 M_{\odot}$ (see Table 5.1 and Section 5.1.2). Our analysis in Section 5.1.2 using model fits to the partial eclipse produce main sequence (MS) solutions using Baraffe et al. (1998) for the M dwarf of $M_S \approx 0.15\text{--}0.35 M_{\odot}$ and $R_S \approx 0.17\text{--}0.32 R_{\odot}$, making it a candidate for probing the stellar structure of the low-mass MS. The M dwarf is further constrained in Section 5.1.3 by using the SDSS spectrum and is expected to be of type M4–M6 with $M_S \approx 0.11\text{--}0.20 M_{\odot}$. Measuring the ingress and egress as well as ellipsoidal and reflection effects in multiple color filters of the J1435 eclipse would probe the WD atmosphere.

In Section 5.1.1 we detail our observations and data reduction. A deep analysis for ZZ Ceti type pulsations revealed no pulsations down to a 4 mmag detection limit (see Section 3.3.6 for details). In Section 5.1.2 we discuss our analysis of the eclipse light curve and use it to constrain the properties of J1435. In Section 5.1.3 we discuss the consequences our results along with the SDSS spectrum have on the properties of the secondary star.

Table 5.1. Properties of SDSS J143547.87+373338.5

Property	Eisenstein et al. (2006)	Gänsicke et al. (Hot)	Gänsicke et al. (Cold)
T_{eff} (K)	11062 ± 58	12681 ± 990	12392 ± 350
$\log g$ (dex)	6.860 ± 0.038	7.68 ± 0.20	7.82 ± 0.14
M_{WD} (M_{\odot})	0.20 ^a	0.35 ^b	0.58 ^c
R_{WD} (R_{\odot})	0.0273 ^a	0.0178 ^b	0.0132 ^c

^aFrom Althaus & Benvenuto (1997) He core model, using $\log g = 6.86$.

^bFrom Althaus & Benvenuto (1997) He core model, using $\log g = 7.48$ lower limit.

^cFrom Althaus & Benvenuto (1998) C/O core with $10^{-4}M_{\odot}$ H envelope model, using $\log g = 7.96$ upper limit.

5.1.1 Observations and Data Reduction

SDSS J1435 was targeted, along with many other objects, in a campaign to discover very-low-mass (He core) and very-high-mass (O-Ne core) pulsating DA WDs (ZZ Ceti). From within the Sloan Digital Sky Survey, Eisenstein et al. (2006) released over 9,000 spectroscopically classified WDs. We selected only those DA objects within the empirical ZZ Ceti instability strip (Gianninas et al. 2006; Mukadam et al. 2004b) of either low ($\log g < 7.45$) or high ($\log g > 8.7$) gravity. J1435 was among several dozen objects that met the low gravity criteria and was visible during our observing run of 29 May through 1 June 2007. In Table 5.1 we list the properties of J1435 as measured by Eisenstein et al. (2006) and Gänsicke et al. (priv. com., Rebassa-Mansergas et al. 2007). We report both a "cold" and

”hot” solution for the WD parameters as the equivalent widths of the Balmer lines go through a maximum near $T_{\text{eff}} \approx 13,000$ K (dependent on $\log g$) and two solutions of similar quality result on either side of this maximum. In most cases, this degeneracy is lifted by fitting the overall shape of the spectrum, however, since J1435’s T_{eff} is so near the maximum, both solutions are indistinguishable (Rebassa-Mansergas et al. 2007). The large discrepancy in parameters is because Eisenstein et al. (2006) did not spectrally subtract the companion’s contribution whereas Gänsicke et al. (priv. com., Rebassa-Mansergas et al. 2007) did.

We observed J1435 on the nights of 29 May, 31 May, and 1 June 2007 with the 3.5-meter WIYN telescope at the Kitt Peak National Observatory. All observations used the OPTIC camera with two 4K×2K pixel CCDs side-by-side (15 μm pixels) for a total of 4K×4K pixel viewing area with a full frame field of view of 9’5×9’5 (Howell et al. 2003). Exposure times were 15 seconds over ≈ 2 hr for the 29 May and 31 May observations, and 40 seconds over ≈ 3.5 hrs on 1 June. All exposures were with the broadband BG-39 filter ($\lambda_c \approx 4800\text{\AA}$, FWHM $\approx 2600\text{\AA}$). The 4K×4K total pixel CCD was binned 2×2 to reduce the readout time to ≈ 8.1 seconds, which varied by ≈ 0.03 seconds during a night.

All images were reduced by applying an averaged two dimensional bias subtraction, and were flattened using averaged and normalized dome flat field images taken immediately prior to the night’s observations. All tasks were performed using standard tasks within IRAF (Image Reduction and Analysis Facility). Light

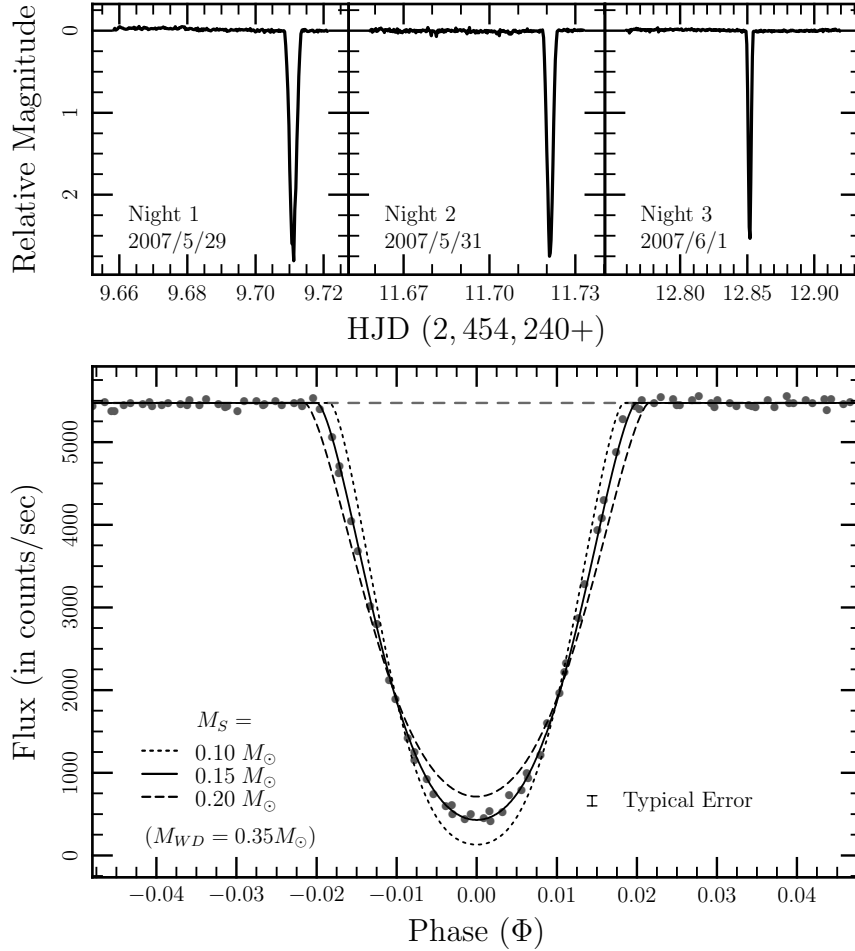


Figure 5.1: Top Panels: Light curves of all three nights in relative magnitudes. Bottom Panel: Phased light curves of all nights centered on the primary eclipse and in relative flux units. Note the representative average error bar of the measurements (grey points). The solid line is the eclipse fit (see Section 5.1.2) for $M_{WD} = 0.35 M_\odot$ (first line in Table 5.2). The other two lines are the best possible fits for other MS masses at $M_{WD} = 0.35 M_\odot$.

curves were produced by extracting fluxes from the program star and several comparison stars and taking their ratios. Fluxes were extracted using the IRAF package VAPHOT (Deeg & Doyle 2001), which applies a dynamic method to aperture size adjustment (both flux apertures and sky background estimation annuli) to account for variable seeing. Fifteen comparison stars were selected within the frame ranging from $B \approx 16$ to 19.5. Differential photometry was performed using the comparison star weighting scheme detailed in Sokoloski et al. (2001) and inspired by Gilliland & Brown (1988).

Though targeted as a possible ZZ Ceti using the T_{eff} and $\log g$ measured by Eisenstein et al. (2006), the new T_{eff} and $\log g$ measurements by Gänsicke et al. (priv. com., Rebassa-Mansergas et al. 2007) place it outside the empirical instability strip (Gianninas et al. 2006; Mukadam et al. 2004b). It is therefore not surprising that our Lomb-Scargle periodogram analysis found no (to 4 mmags) pulsations in the frequency range of 1–17 mHz.

5.1.2 Eclipse Analysis

All three nights of observation show distinct primary eclipses (see Figure 5.1). Using the technique developed by Kwee & van Woerden (1956), fits to the transit centers of these eclipses show primary minima at HJD $2,454,249.711028 \pm 0.000016$, $2,454,251.7211338 \pm 0.0000044$, and $2,454,252.8517916 \pm 0.0000051$. Combining these primary minimum epochs

gives an ephemeris of $\text{HJD } 2,454,249.711056 \pm 0.000011 + \text{N } 0.12562974 \pm 0.00000055$. Our analysis obtains an orbital period of $P = 3.015114 \pm 0.000013$ hrs ($10,854.410 \pm 0.048$ sec) and a transit time (measured as first departure from and full recovery to maximum light) of $\tau \approx 480$ sec.

We constrain the secondary through detailed modeling of the eclipse light curve. There is no evidence of a secondary eclipse, so we only model the primary eclipse and assume the secondary star to be a black (non-luminous) disk. If we assume a point light source WD, $R_{WD} \ll R_S$, Kepler's Law and the system's partially eclipsing geometry lead to a degeneracy between M_S , R_S , and i . We can connect M_S and R_S with a MS $M - R$ relation, but are unable to break the relationship to i . This last degeneracy is broken by giving the WD its finite physical extent, R_{WD} , and modeling the WD disk with a standard linear limb darkening law (van Hamme 1993): $I(\theta)/I(0^\circ) = 1 - u_{LD}[1 - \cos(\theta)]$, where θ is the angle made by the normal vector to the WD surface to the line-of-sight. We obtain the range $M_{WD} = 0.35\text{--}0.58 M_\odot$ by using the $\log g$ and T_{eff} ranges measured by Gänsicke et al. (priv. com., Rebassa-Mansergas et al. 2007, see Table 5.1). The low mass limit uses the He core WD cooling tables of Althaus & Benvenuto (1997) while the high mass limit uses the cooling tables of Althaus & Benvenuto (1998) for a C/O core WD with a $10^{-4}M_\odot$ H envelope of solar metallicity. Finally, we assume circular orbits and the geometry of an inclined system of orbiting masses. In all, there are seven parameters: M_{WD} , M_S , R_{WD} ,

R_S , i , P , and u_{LD} . We fit simple $\cos(\Phi)$ and $\cos(2\Phi)$ functions to determine the strength of reflection and ellipsoidal variations (respectively) on the light curve, but found no such variations at the 0.5% level. We neglect the modeling of these variations.

In Figure 5.2 we present the three-sigma χ_{fit}^2 contours for the $R_S - M_S$ parameter space for two values of the linear limb darkening coefficient and extreme WD masses of the accepted range. We obtain a contour by fixing P , u_{LD} , M_{WD} , and R_{WD} . Then at each point in the $R_S - M_S$ parameter space we minimize χ_{fit}^2 with respect to the inclination and adopt this χ_{fit}^2 value for that mass and radius. Our data tightly constrains the radius of the secondary while very loosely constraining the mass if we assume a specific linear limb darkening coefficient and WD solution with non-negligible radius. Figure 5.1 shows a comparison of model fits to the observed light curve for one set of WD parameters and three sets of MS parameters fit over i . This figure plainly shows the broken degeneracy between $M_S - R_S$ and i .

When modeling the limb darkening of a WD atmosphere with a linear law, the coefficient depends upon the effective temperature and the bandpass of the filter. Insufficient data exists to define this dependence, so we used two values bracketing the measured range of similar systems: $u_{LD} = 0.3-0.5$ (Littlefair et al. 2006b, 2007; Maxted et al. 2007).

Given the present uncertainties and range of RL fillings, we simply assume

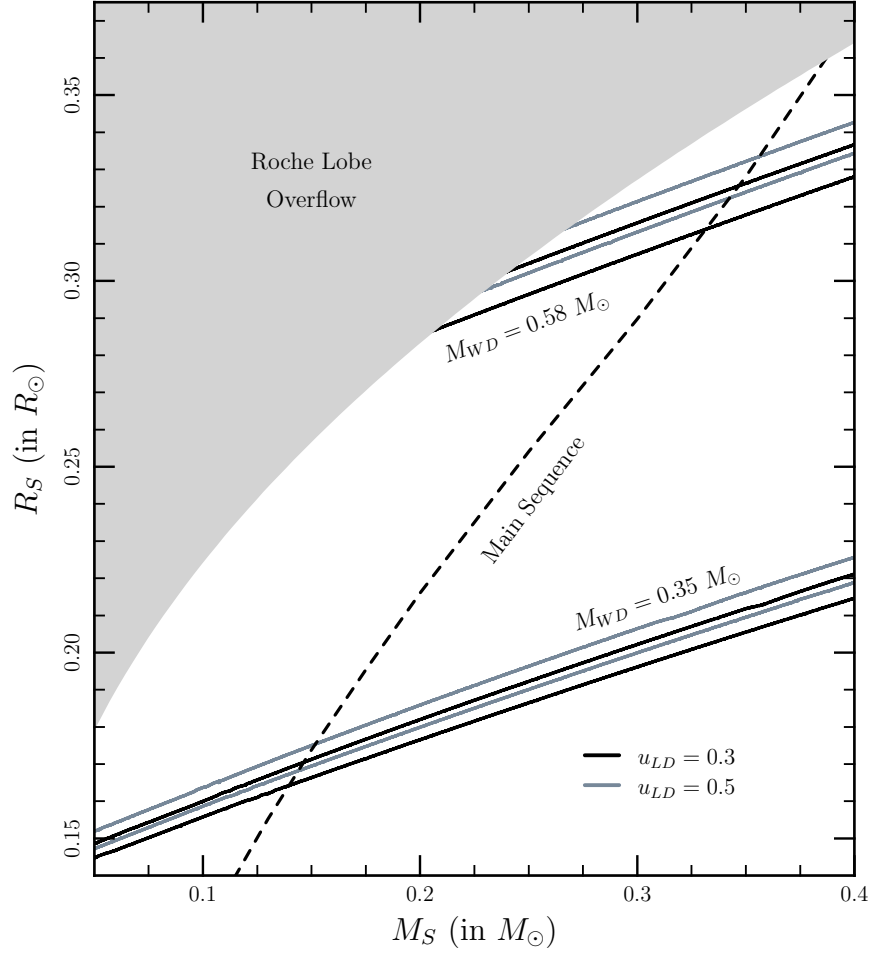


Figure 5.2: Constraints within the $R_S - M_S$ parameter space. Three-sigma contours of minimized χ^2_{fit} to eclipse light curve (see Section 5.1.2) using the two extreme accepted WD masses and two linear limb darkening coefficients. RL overflow boundary defined using Eggleton (1983). Theoretical MS from Baraffe et al. (1998).

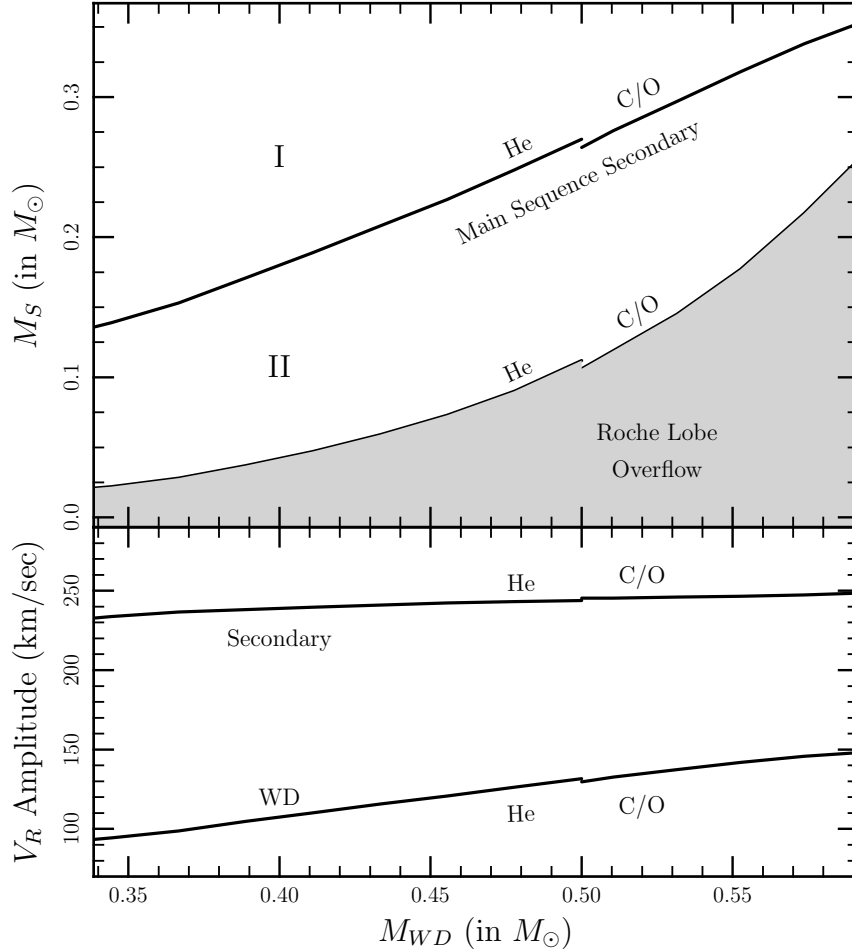


Figure 5.3: Upper Panel: Constraints within the M_S – M_{WD} parameter space. All curves incorporate a minimized χ^2 fit to eclipse light curve (see Section 5.1.2). All WD M – R relations are derived as follows: He WD from Althaus & Benvenuto (1997) and C/O WD from Althaus & Benvenuto (1998). The MS M – R relation is from Baraffe et al. (1998). The RL boundary is defined using Eggleton (1983). Region I requires a secondary which is denser than a MS star of its mass, a likely sign of He enrichment. Region II requires a secondary which is less dense than a MS star of its mass, most likely not in thermal equilibrium and still contracting to the MS. Lower Panel: Radial velocity amplitudes for the WD and secondary for the MS solutions in the Upper Panel.

Table 5.2. Best Fit Main Sequence Secondary Solutions

M_{WD} (M_{\odot})	u_{LD}	M_S (M_{\odot})	R_S (R_{\odot})	i (deg)	$V_{R,WD}$ (km/sec)	$V_{R,S}$ (km/sec)
0.35	0.3	0.143	0.167	79.3	95.7	234
0.35	0.5	0.148	0.172	79.0	98.3	233
0.58	0.3	0.340	0.320	72.4	146	248
0.58	0.5	0.349	0.327	72.0	148	246

that the secondary star has the M_S-R_S relation from Baraffe et al. (1998). The MS solutions for the two extreme accepted WD masses and two limb darkening coefficients are in Table 5.2. Further, we investigated how the secondary star solution would change with the WD mass. In Figure 5.3 we plot the best fit MS star solutions using He core and C/O core WD models from Althaus & Benvenuto (1997, 1998) in the M_S-M_{WD} parameter space.

We bound this space for low M_S by requiring that our system not be in RL overflow. If we assume our system to be at the boundary of RL overflow we can minimize χ_{fit}^2 along the RL overflow boundary shown in Figure 5.2. The result of this minimization can be seen in Figure 5.3 as the boundary of the shaded region. The scaling of this curve is simply understood by considering the geometry of inclination and the circular orbits of two masses. By requiring an inclination where the WD is just fully eclipsed at zero phase, using the period and transit time of the binary, the radius of the secondary is found as a function of M_{WD} and M_S . Equating this radius with the RL filling radius of Eggleton (1983) gives M_S

as a function of M_{WD} whose scaling closely follows that of the curve in Figure 5.3. Any system below this line must be in RL overflow. Figure 5.3 clearly illustrates two regimes for the secondary star. Region I requires it to be more dense than that of a MS star of the same mass, therefore, if found in this region it would be a likely sign of He enrichment in the secondary from a prior stage of mass transfer (Pylyser & Savonije 1989). Region II requires the secondary star to be less dense than that of a MS star of the same mass, therefore, if found in this region, the secondary would likely not be in thermal equilibrium. Both of these conditions are only possible if J1435 is a mass transfer system that is temporarily out of contact. That being said, the most likely explanation for J1435 is a pre-Cataclysmic Variable (pre-CV) where the M dwarf is a MS star that has yet to make contact.

5.1.3 Discussion

Our analysis of J1435 is far from complete. With a single color light curve of the primary eclipse, only broad constraints may be placed upon the parameters of the system (see Section 5.1.2). Therefore, we look to future observations in multiple colors as well as full spectra over the entire orbit to increase the precision and accuracy of the system parameters. Our observations in a very blue bandpass, while ideal for a ZZ Ceti pulsation search, puts the effects of an M dwarf secondary eclipse at a level far below the precision of our observations. A redder bandpass

would allow for better observation of the secondary eclipse and resulting model fits would provide additional constraint to J1435's components. Full spectral coverage over the entire orbital period would ideally reveal a double-lined binary system yielding velocity curves for both components. With these velocity curves, good measurement of the inclination of the orbit can be made.

One spectrum of J1435 was observed in the SDSS (York et al. 2000) and within the errors of our ephemeris the entire exposure was taken out of eclipse. Visual inspection of the SDSS spectrum and comparison with M dwarf spectra from Bochanski et al. (2007) clearly place the secondary star's spectral type to be later than M4, consistent with under-filling the RL at $P = 3$ hrs with $M_S < 0.2M_\odot$ (Knigge 2006). Using the empirical M dwarf colors from Bochanski et al. (2007) we fix the colors of the secondary at $u' - g' > 2.3$ and $g' - i' > 3.0$. Therefore, the M dwarf contribution in the BG-39 filter would be $\lesssim 4\%$ of the total system flux. This is consistent with the 10% remaining flux observed at maximum eclipse and the lack of an observed secondary eclipse.

Further constraint of the secondary mass is possible by using the SDSS spectrum, synthetic WD spectra, and WD and M dwarf absolute magnitudes. We used a synthetic WD spectrum provided by Gänsicke et al. (priv. com., Rebassa-Mansergas et al. 2007) within the J1435 T_{eff} and $\log g$ parameters and scaled it to fit the Balmer absorption lines shorter than 500 nm in the SDSS spectrum. In the Johnson V filter at 560 nm, the contribution from a WD with our synthetic

spectrum requires the M dwarf to be ≈ 2.3 magnitudes fainter. Using Holberg & Bergeron (2006) for WD and Knigge (2006) for M dwarf absolute magnitudes, we find the M dwarf to be in the spectral range M4-M6 with $M_S = 0.11\text{--}0.20 M_\odot$. This analysis is in contrast to that of Silvestri et al. (2006) which found the M dwarf spectral type of J1435 to be M2-M4 with $M_S = 0.20\text{--}0.55 M_\odot$. It is clear that much more rigorous spectral analysis needs to be carried out if it is to be used to constrain the secondary mass.

We expect that J1435 is a pre-CV system with the M dwarf secondary on or near the MS. Two systems with similar parameters to J1435, MS Peg and NN Ser, have calculated times to contact of ≈ 1.5 Gyrs (Schreiber & Gänsicke 2003). There are little more than a dozen eclipsing double-lined spectroscopic binaries containing M dwarfs below $1M_\odot$ (Bayless & Orosz 2006; Hebb et al. 2006; Ribas 2006; Young et al. 2006; Devor et al. 2008; López-Morales & Shaw 2007; Shaw & López-Morales 2007). If J1435 were found to be a double-lined spectroscopic binary, from which velocity curves for both components could be found and its parameters found to high precision, it would be a significant addition to this group especially being below $0.35M_\odot$, where theory (Siess et al. 1997; Baraffe et al. 1998; Yi et al. 2001) would benefit. However, many recent surveys are revealing many WD post common envelope binary systems as well as several more eclipsing systems (Rebassa-Mansergas et al. 2007; Drake et al. 2009; Pyrzas et al. 2009; Rebassa-Mansergas et al. 2010).

5.2 Discovery of the Eclipsing Detached Double

White Dwarf Binary NLTT 11748

² Double white dwarfs (WDs) in tight enough ($P_{\text{orb}} < \text{day}$) binaries to reach contact in a Hubble time are expected on theoretical grounds (Nelemans et al. 2001), and are presumed to be the progenitors of highly variable objects: R CrB stars, AM CVn binaries, and Type Ia supernovae (Iben & Tutukov 1984; Webbink 1984). However, examples of these systems are rare, with only 10 known prior to May 2010 (Nelemans et al. 2001; Badenes et al. 2009; Mullally et al. 2009; Kilic et al. 2010b; Marsh et al. 2010; Kulkarni & van Kerkwijk 2010). Many of these binaries are of immediate interest for the *Laser Interferometer Space Antenna* (*LISA*), providing ‘verification’ sources loud enough to be detected in space (Nelemans 2009).

Spectral measurements of the high proper motion object NLTT 11748 by Kawka & Vennes (2009) revealed it to be a low-mass ($< 0.2 M_{\odot}$) helium core WD with $\log g = 6.2 \pm 0.15$ and $T_{\text{eff}} = 8540 \pm 50 \text{ K}$ and an H-rich (DA) atmosphere. The strong expectation that low-mass He WDs can only be formed in common envelope events led Kawka & Vennes (2009) to note that this object was likely a binary. Indeed, they found a 40 km s^{-1} velocity difference between two measured spectra. NLTT 11748 was originally targeted in a ZZ Ceti like pulsation search

²This section is adapted and reproduced from Steinfadt et al. (2010b) with the permission of the American Astronomical Society.

based on theoretical calculations and the $\log g$ and T_{eff} measurements (Steinfadt et al. 2010a). In this failed pulsation search, our rapid (≈ 1 minute) differential photometry with the Las Cumbres Observatory’s Faulkes Telescope North (FTN) revealed ≈ 180 s 3%–6% dips, which were confirmed by Keck spectroscopy to be primary and secondary eclipses from a $\approx 0.7 M_{\odot}$ faint C/O WD companion orbiting at 5.6 hr.

NLTT 11748 joins the growing class (Kawka et al. 2006; Kilic et al. 2007a; Mullally et al. 2009; Kilic et al. 2010b; Marsh et al. 2010; Kulkarni & van Kerkwijk 2010; Badenes et al. 2009) of WD binaries where the low-mass WD is a very low-mass ($< 0.2 M_{\odot}$) helium core WD.

Our observations are summarized in Section 5.2.1, demonstrating that the companion to NLTT 11748 is a cold ($T_{\text{eff}} \lesssim 7400$ K), old (1.5–3 Gyr) C/O WD. We show in Section 5.2.2 that eclipse modeling yields the first radius measurement of an extremely low-mass WD. We close in Section 5.2.3 by discussing the value of additional measurements for constraining WD mass–radius relations.

5.2.1 Observations

We targeted NLTT 11748 as part of an observational search for ZZ Ceti like pulsations from low-mass He core WDs (Steinfadt et al. 2008b, 2010a; see also Section 3.3.11 for pulsation detection limits). Our photometric discovery led to our Keck spectroscopy, both described here.

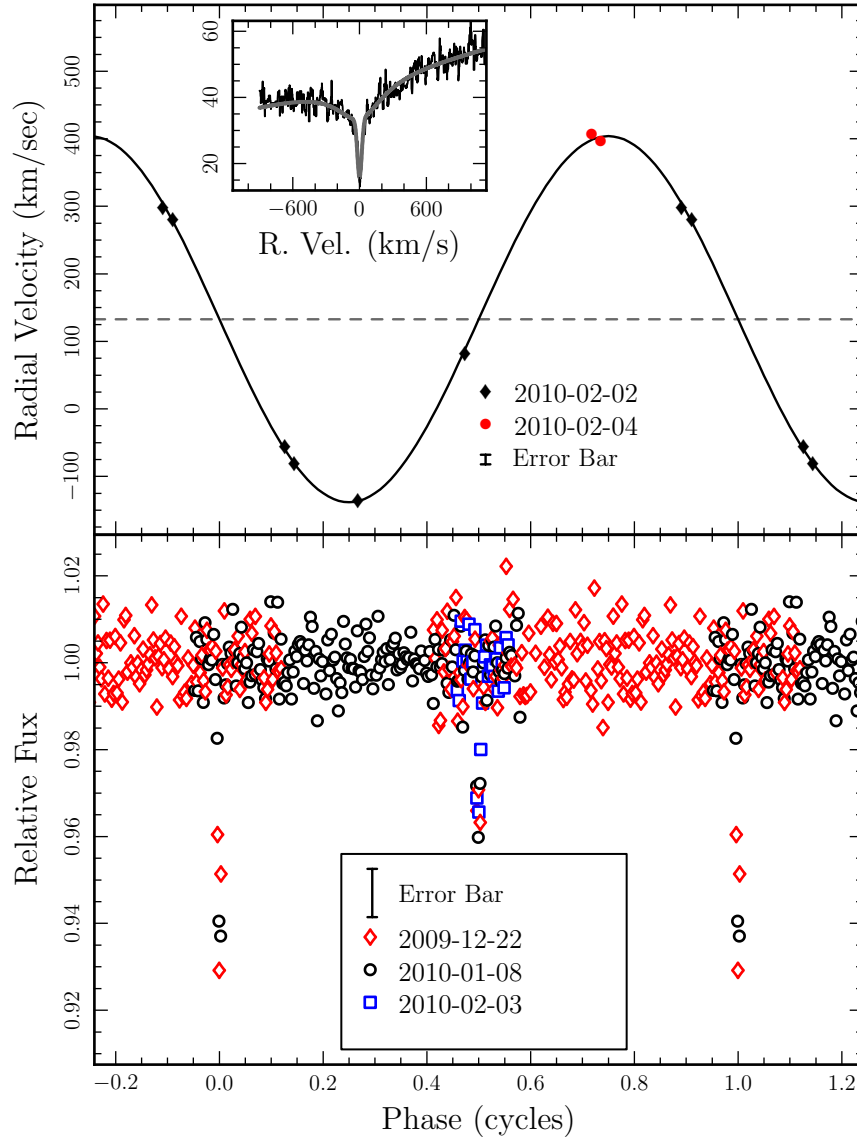


Figure 5.4: Top panel: phased radial velocities from Keck/HIRES H α measurements over two consecutive nights. The black line is the ($e = 0$) sinusoid with $K_1 = 271 \text{ km s}^{-1}$ amplitude and the $v_r = 133 \text{ km s}^{-1}$ systemic velocity offset. Inset shows the phase combined H α spectrum, in arbitrary flux units, with fitting function over plotted. Bottom panel: phased photometric light curve for all three nights of data. The error bar represents 4–5 mmag uncertainty.

Table 5.3. Measured and Derived Quantities for NLTT 11748

Quantity	Value		
HIRES spectra			
Rad. vel. amp., K_1 (km s ⁻¹)	271(3)		
Sys. radial velocity, v_r (km s ⁻¹)	133(2)		
χ^2/dof	4.5/6		
FTN photometry			
Time of prim. ecl. (BJD TDB)	2,455,196.87828(7)		
Period (days)	0.2350606(11)		
Ephemeris χ^2/dof	3.5/3		
Primary eclipse depth, d_1	0.067(3)		
Secondary eclipse depth, d_2	0.034(2)		
Primary ecl. duration, τ_1 (s)	180(6)		
Secondary ecl. duration, τ_2 (s)	185(10)		
F_2/F_1 (in SDSS- g')	0.035(3)		
Out of eclipse ^a χ^2/dof	404.8/372		
Combined data (assuming Mass of Primary $M_1 = 0.15M_\odot$)			
Limb darkening coefficient, u_{LD}	0.0	0.3	0.5
Mass of secondary, M_2 (M_\odot)	0.71(2)	0.71(2)	0.71(2)
Inclination (deg)	89.90(11)	89.88(11)	89.87(11)
Radius of primary, R_1 (R_\odot)	0.0393(9)	0.0406(9)	0.0415(9)
$\chi^2/\text{dof}^{\text{b}}$	285.1/227	279.5/227	276.5/227
Distance ^c (pc)	150(32)		
Sys. kin. (U, V, W) ^d (km s ⁻¹)	(-151(9), -183(41), -34(5))		

Note. — Quantities in parentheses are 1σ uncertainties on the last digit.

^aExcluding ± 0.005 cycles around each eclipse.

^bResult of fitting phases ± 0.1 cycles around each eclipse.

^cScaled from Kawka & Vennes (2009) using our R_1 .

^dCalculated from the proper motion (Kawka & Vennes 2009) corrected to the local standard of rest (Hogg et al. 2005) and our updated distance.

Faulkes Telescope North Photometry

Photometric observations were done with the 2-m robotic (FTN) (Lewis et al. 2010), part of the Las Cumbres Observatory Global Telescope (LCOGT) network³, on Haleakala, Hawaii. We used the Merope camera with 2×2 pixel binning for a pixel scale of $0''.28 \text{ pixel}^{-1}$ and a $4'.75\times 4'.75$ field-of-view. Our observational setup, consisting of the SDSS- g' filter and 45 s exposure time (with ≈ 22 s dead time), was aimed at detecting pulsations, expected to be at the few minutes timescale (Steinfadt et al. 2008b, 2010a). Preliminary reduction, including bias and flat-field corrections using standard IRAF⁴ routines, is done automatically at night's end.

Our first observation on 2009 December 22 (night 1) was for 4 hr. We immediately identified two dips in the light curve, ≈ 3 minutes in duration and a few percent in depth, indicative of eclipses. To verify the existence of eclipses we observed the system again on 2010 January 8 (night 2), for 3.5 hr, revealing two similar eclipses at the expected times based on the previous observations. An additional 30-minute observation was obtained on 2010 February 3 (night 3).

Photometric processing was carried out using IRAF aperture photometry and the VAPHOT package of routines (Deeg & Doyle 2001). Three comparison stars were selected to yield a light curve with the smallest variance. In 45 s expo-

³<http://lcogt.net>

⁴IRAF is distributed by the National Optical Astronomy Observatory, which is operated by the Association of Universities for Research Astronomy, Inc., under cooperative agreement with the National Science Foundation. <http://iraf.noao.edu>

tures, each of these stars accumulated $\approx 4 \times 10^5 e^-$ while NLTT 11748 accumulated $\approx 7 \times 10^5 e^-$. The differential light curve for NLTT 11748 was constructed using the scheme detailed in Steinfadt et al. (2008b, inspired by Sokoloski et al. 2001). A de-trending second-order polynomial removed uncorrected long-term variations, such as color–airmass effects. For all data points outside of eclipses we find a χ^2/dof of 404.8/372, indicating a reasonable estimate of our uncertainties.

After considering the radial velocity measurements in Section 5.2.1, we found that nights 1 and 2 had primary and secondary eclipses, while night 3 shows a secondary eclipse. Using the technique of Kwee & van Woerden (1956) we fit the transit centers of each eclipse, and combined all eclipse timings (primary (BJD TDB): 2,455,188.886207(89), 2,455,205.81071(29); secondary (BJD TDB): 2,455,188.76882(16), 2,455,205.92783(19), 2,455,231.784879(19)) in a linear least-squares analysis to find the orbital period of $P_{\text{orb}} = 5.641454 \pm 0.000026$ hr (barycentering used the JPL DE405 ephemeris). Fitting ephemerides using the primary and secondary eclipses separately gives consistent results with our reported ephemeris (Table 5.3). The resulting phased light curve from all three nights of data is shown in Figure 5.4.

Keck Spectroscopy

We observed NLTT 11748 with High Resolution Echelle Spectrometer (HIRES, Vogt et al. 1994) on the 10-m Keck I telescope 6 times on 2010 February 2 and

twice on 2010 February 4. All observations were taken with the same grating tilt, integrating for 5 minutes, binning by 3 pixels in the spatial direction, and with a $0''.86 \times 14''$ slit (giving $R \approx 50,000$). The wavelength solution was based on a Th–Ar lamp, accurate to <0.1 pixel (with $1.4 \text{ km s}^{-1} \text{ pixel}^{-1}$), and the data covered 3,600–8,000 Å. The stability of the solution was monitored to high precision by G. Marcy (private communication, 2010).

We used the H α line for our radial velocity measurements, although other lines were detected at lower significance. We initially identified the velocity from each spectrum by eye, then shifted each spectrum to zero velocity and combined them. We fit the combined H α spectrum with the sum of a broad ($\approx 520 \text{ km s}^{-1}$ FWHM) Lorentzian and a narrow ($\approx 47 \text{ km s}^{-1}$ FWHM) Gaussian with roughly equal depths. Using this template, we then measured radial velocities and fit them to a sinusoid with the period and phase constrained by the eclipse timing. We then iterated this procedure, using the velocities from the radial-velocity fit to construct the template, fitting the template shape, fitting the individual velocities, and fitting the radial velocity curve. This converged quickly: after one iteration all changes were $< 1 \text{ km s}^{-1}$.

We obtain a χ^2 for the radial velocity fit (assuming a circular orbit and an accurate ephemeris from the eclipse photometry) of 4.5 for 6 dof. Our final radial-velocity amplitude was $K_1 = 271 \pm 3 \text{ km s}^{-1}$ yielding a mass function $0.48(2) M_\odot$, or an $M_2 = 0.71(2) M_\odot$ secondary for a fiducial $M_1 = 0.15 M_\odot$ primary. We

computed the systemic radial velocity from the data, correcting to the solar system barycenter, finding $v_r = 133 \pm 2 \text{ km s}^{-1}$. We do not correct for gravitational redshift as uncertainties in M_1 and R_1 are too high and we expect a shift of only $\approx 2 \text{ km s}^{-1}$. We checked our velocities by fitting only the broad component of the $\text{H}\alpha$ line or the $\text{H}\gamma$ line, and both gave consistent results although with a factor of 6 lower precision. We limit the eccentricity of the orbit to <0.06 at 3σ .

At the primary’s orbital velocity, the width of the narrow $\text{H}\alpha$ component may be broadened by orbital motion: the maximum derivative is $2\pi K_1/P_{\text{orb}} = 0.08 \text{ km s}^{-1} \text{ s}^{-1}$. Compared with the narrow $\text{H}\alpha$ component, $\approx 47 \text{ km s}^{-1}$ FWHM, this effect is unlikely to affect our data (5-minute exposures) but might have slightly influenced the $\log g$ measurement of Kawka & Vennes (2009).

5.2.2 Binary Parameter Analysis and Results

The deepest (primary) eclipse is the transit of the primary object (1) by the secondary (2), and the shallowest (secondary) is the occultation of the secondary by the primary. There are six relevant binary parameters to be fitted: the primary and secondary radii and masses (R_1 , R_2 , M_1 and M_2); flux ratio (for our filter/CCD response) F_2/F_1 ; and inclination i . We consider the orbital period, P_{orb} , and the linear limb darkening coefficient, u_{LD} , as fixed. We presume $u_{\text{LD}} = 0.3$ but will show how its uncertainty ($u_{\text{LD}} \approx 0.2 - 0.6$, Littlefair et al. 2006a, 2007, and Maxted et al. 2007) modifies our desired parameters. The eclipse light curve in

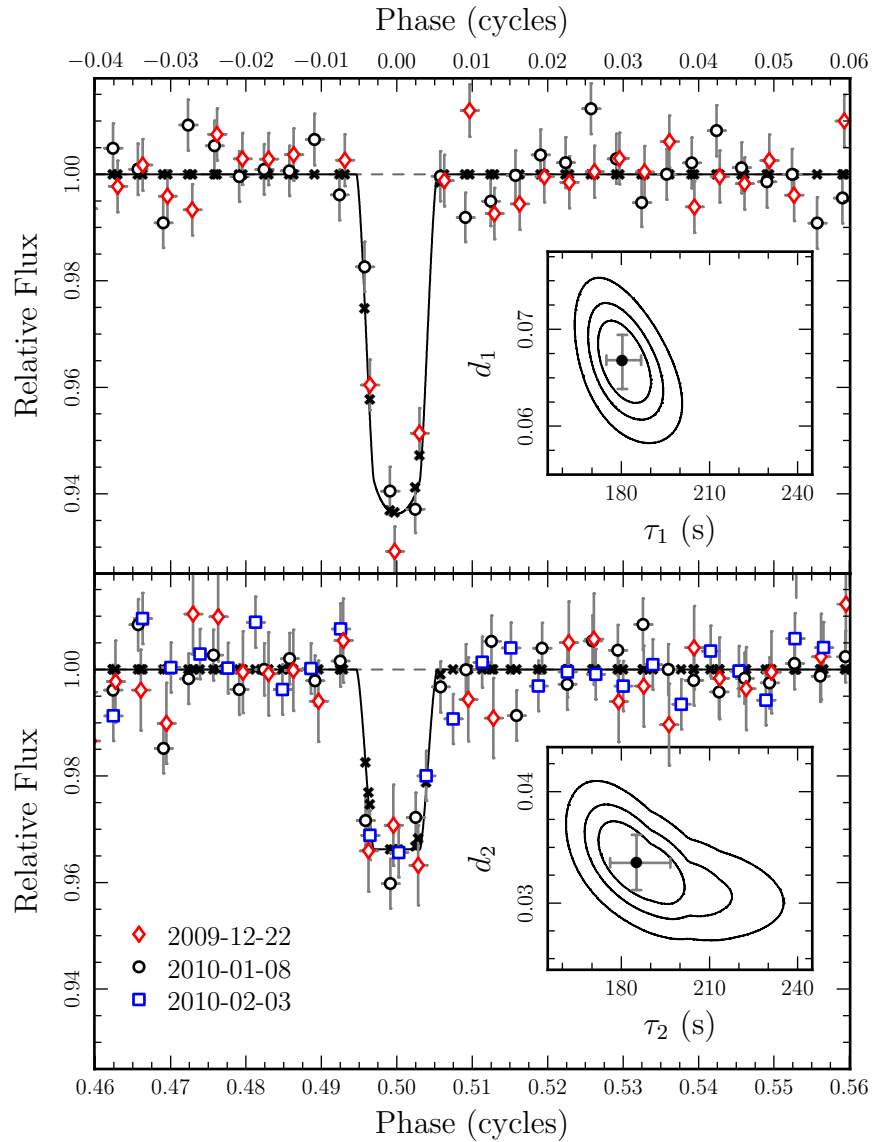


Figure 5.5: Phased light curves of the primary (top panel) and secondary (bottom panel) eclipses. The widths of each data point represent the exposure duration. The black line is the light curve model for the $u_{LD} = 0.3$ parameters in Table 5.3. The crosses show the average of the model over the exposure duration of that associated data point. It is the differences between these points and those measurements that are considered when calculating χ^2 . Insets display the 1σ , 2σ , and 3σ contours of the χ^2 minimization for the eclipse depth and width parameterized light curve fitting. The error bars are the 1σ error bars on the individual parameters.

Figure 5.5 shows the secondary eclipse as flat-bottomed while the primary eclipse shows the distinct signature of limb darkening. This indicates that the eclipses are likely total (confirmed by our inclination measurements) and $R_2 < R_1$, $F_2/F_1 \ll 1$, and $i \approx 90^\circ$.

We initially fit the eclipses with a parameterization of the linear limb darkening law (van Hamme 1993) for the primary eclipse and a box function for the total secondary eclipse, yielding the depths, d_1 and d_2 , and durations, τ_1 and τ_2 . The 1σ results are reported in Table 5.3 with the 1σ , 2σ , and 3σ contours plotted in the insets of Figure 5.5. This allows us to directly measure F_2/F_1 , as $1 - d_2 = F_1/(F_1 + F_2)$.

The sparsity of our data in eclipse requires additional assumptions about the properties of the secondary. The flat bottom secondary eclipse unambiguously gives a low flux ratio (at SDSS- g') of $F_2/F_1 = 0.035(3)$ which implies that the value of the primary eclipse total depth must be dominated by the radii ratio. Our measured primary eclipse depth implies $R_2/R_1 \approx 1/4$, further corroborated by the unseen (and thereby fast) ingress and egress in the secondary eclipse. Our measurements of F_2/F_1 and R_2/R_1 constrain the temperature of the secondary relative to the 8500 K primary. Taking SDSS- g' measurements as bolometric ($L_2/L_1 = F_2/F_1$) gives $T_2 \leq 7400$ K, which we confirm by using the synthetic photometry of Holberg & Bergeron (2006), constraining the flux ratio of model atmospheres integrated over the filter passband. The Kawka & Vennes (2009)

spectrum constrains the primary to be a low-mass, $\lesssim 0.25 M_\odot$, likely He WD with a radius $\approx 0.04 R_\odot$. This implies an $R_2 \approx 0.01 R_\odot$ companion. Therefore, the secondary cannot be a main sequence (MS) star as Kawka & Vennes (2009) constrain such an MS star to have $M < 0.2 M_\odot$ based on Two Micron All Sky Survey photometry, breaking our mass function and radius constraints. A brown dwarf would break our mass function and radius constraints. A neutron star is far too small and its luminosity contribution insufficient. Therefore, a cold C/O WD is the only solution, meeting the radius, mass, and luminosity constraints.

We powerfully constrain the binary parameters by directly integrating the faces of the primary and secondary and model our light curve for any arbitrary inclination and phase by assuming a linear limb darkening law. We do this with a code originating from Steinfadt et al. (2008a) and Mandel & Agol (2002), including the effects of microlensing in the binary (following Marsh 2001 and Agol 2002). For the approximate parameters above, the Einstein radius is $R_E = \sqrt{4GM_2a/c^2} \approx 0.003 R_\odot$, giving $R_1/R_E \approx 13$ and $R_2/R_E \approx 3$, leading to a 1% magnification of the primary at conjunction. Our measurement of K_1 and F_2/F_1 reduces our six-parameter system to four-parameter system. Our surface temperature measurement yields an age of 1.5–3.0 Gyr (Chabrier et al. 2000) for the secondary allowing us to use M-R relations of cold WDs (Althaus & Benvenuto 1998) for our current work. Though Kawka & Vennes (2009) derived an $M_1 = 0.167 \pm 0.005 M_\odot$ from their low-resolution spectrum, radial velocity broad-

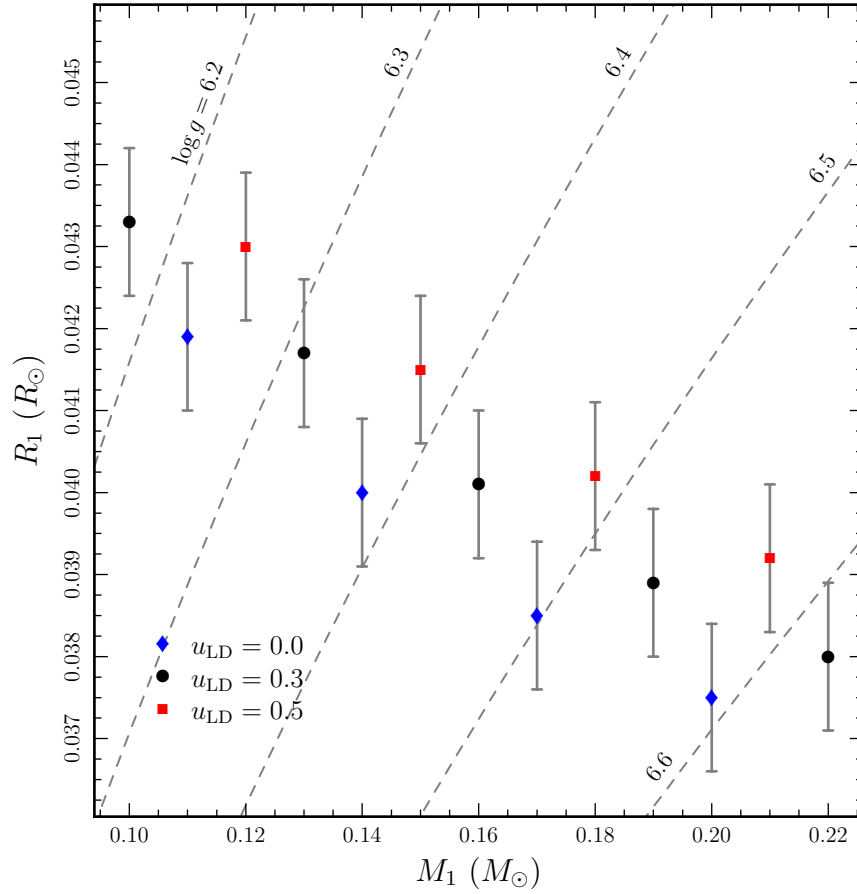


Figure 5.6: Primary radius vs. primary mass. The uncertainties are 1σ uncertainties assuming the values and uncertainties of K_1 and F_2/F_1 given in Table 5.3 and assuming a secondary radius derived from its mass. Dashed lines are constant $\log g$.

ening and theoretical model uncertainties may render this determination unreliable. Therefore, we calculate separate χ^2 grids of R_1 and inclination for a range of M_1 . Minimization of χ^2 on each grid constrains R_1 and inclination directly and $\Delta\chi^2$ techniques yield their uncertainties. We scale these uncertainties to consider the additional uncertainties of F_2/F_1 and K_1 using a Monte Carlo method.

The results of our direct eclipse fitting method are displayed in Figure 5.6 with the parameters and uncertainties reported in Table 5.3 for $M_1 = 0.15 M_\odot$. Without including lensing the fits would be very similar, but the inclination would be slightly lower (closer to 89.4°) and the radius of the primary would be slightly larger ($0.0437 R_\odot$ for $u_{LD} = 0.3$). The χ^2 minima for all M_1 within each u_{LD} data set in Figure 5.6 are approximately consistent and as such yield no constraint on M_1 over this range. Our range of $u_{LD} = 0.0, 0.3, \text{ and } 0.5$ results in a $\approx 5\%$ spread in R_1 measurements, consistent with the $\log g = 6.2 \pm 0.15$ of Kawka & Vennes (2009). The χ^2 value is reduced slightly as u_{LD} increases; however, we cannot constrain u_{LD} due to the sparsity of data at ingress/egress. This will be constrained in future higher cadence data sets. For $M_1 > 0.2 M_\odot$ the minimum χ^2 values significantly increase and the quality of the eclipse fits degrade. Therefore, our combined radial velocity and light curve data sets provide an upper limit, assuming that the secondary is a C/O WD, of $M_1 \lesssim 0.2 M_\odot$.

5.2.3 Conclusions

Our discovery of the first eclipsing detached double WD binary has substantially constrained low-mass He WD models with radius measurements that agree with current models (Serenelli et al. 2002; Panei et al. 2007). Additional measurements will reveal even more about the faint $\approx 0.7 M_{\odot}$ C/O WD secondary. With our discovery, there are 11 confirmed double WD binaries that will merge within a Hubble time. From spectroscopic masses alone, six of these contain low-mass ($< 0.25 M_{\odot}$) He core primaries with large ($> 0.03 R_{\odot}$) radii indicative of a stable H burning shell (Mullally et al. 2009; Kilic et al. 2010b; Badenes et al. 2009; Marsh et al. 2010; Kulkarni & van Kerkwijk 2010). Other than its inclination, NLTT 11748 is not extraordinary in any way relative to these, many of which offer larger solid angles for eclipse observations than NLTT 11748.

Our analysis of this system is far from complete, but our existing constraints, Table 5.3 and Figure 5.6, highlight the value of further studies. High cadence photometry, resolving the ingress/egress of each eclipse, would yield the component radii as functions of inclination and orbital semimajor axis. If future spectroscopic observations can reveal the secondary's line features and measure its radial velocity, this would allow precise measurements of the masses of both components. Detection of eclipses in different filters, both bluer and into the infrared, would additionally constrain the temperature of the secondary further as well as its age.

Model-independent mass and radius determinations for He and C/O WDs are

rare. For He WDs, there exist several pulsar binary systems for which Shapiro time delay measurements have yielded accurate mass determinations: PSR B1855+09 (Kaspi et al. 1994), PSR J0437–4715 (van Straten et al. 2001), PSR J0751+1807 (Bassa et al. 2006b), PSR J1012+5307 (Callanan et al. 1998; van Kerkwijk et al. 1996), PSR J1911–5958A (Bassa et al. 2006a), and PSR J1909–3744 (Jacoby et al. 2003, 2005). Of these, only four have radii measurements, PSR J0437–4715, PSR J0751+1807, PSR J1911–5958A and PSR J1909–3744. However, all rely upon either distance measurements and evolutionary model-dependent luminosities or gravity measurements derived from atmospheric models. Therefore, He WD evolutionary models (Althaus & Benvenuto 1998; Serenelli et al. 2002; Panei et al. 2007) remain largely unconstrained. For C/O WDs, mass and radius measurements have been more frequent (Schmidt 1996; Provencal et al. 1998, 2002; Casewell et al. 2009) and all rely on distance measurements via parallax or cluster membership, surface brightness measurements and detailed knowledge of each spectrum. To reach the precisions required to constrain theoretical models, these measurements must rely upon atmospheric model spectra. Only recently Parsons et al. (2010) have derived precise measurements of mass and radius in a model-independent way in the eclipsing binary system NN Ser. NLTT 11748 offers an additional C/O WD system for model-independent mass and radius measurements as well as the first such system for He WDs.

Gravitational wave emission will bring this system into contact in 13.8–6.3 Gyr

(for $M_1 = 0.1\text{--}0.2 M_\odot$). With a mass ratio of $0.15/0.71 = 0.2$, stable mass transfer at contact is likely to occur and create an AM CVn binary (Nelemans et al. 2001; Marsh et al. 2004). The known orbital period, inclination, and distance ($d \approx 150$ pc) yield the gravitational wave strain at Earth, $h = (3.6 - 7.9) \times 10^{-23}$ (Timpano et al. 2006; Roelofs et al. 2007) at a frequency $\nu \approx 10^{-4}$ Hz for $M_1 = 0.1\text{--}0.2 M_\odot$. Though not ‘louder’ than the verification sources tabulated by Nelemans (2009), NLTT 11748’s accurate ephemeris allows for a coherent folding of the *LISA* data over the mission duration.

Chapter 6

Conclusions

Throughout this dissertation the consistent narrative has been the search for the first pulsating helium core white dwarf (He WD). To that end, in Chapter 2 we extended the existing theory of ZZ Ceti pulsations to that of the very low mass He WDs ($<0.2 M_{\odot}$) and predicted the parameter space in which pulsations would occur. In Chapter 3, we used this theory coupled with observed ZZ Ceti phenomenology to select He WD candidates with T_{eff} and $\log g$'s near the expected instability region and observed 13 objects for pulsations with the hope of reaching detection limits of 1%. This search was unsuccessful in finding pulsations, but has added constraints to pulsation theory and will serve as a guide to future work. Along the way, our project has encountered other unexpected results, such as a low gravity C/O WD ZZ Ceti (Chapter 4) and two unique eclipsing binary systems (Chapter 5).

Of the 13 objects we observed in Chapter 3 seven are likely very low mass He WDs (a potential eighth is likely an interloping A star). Three of these seven are nominally within the high priority candidate region and thus are predicted to pulsate by the theory of Chapter 2. Whether or not these observations offer strong constraint on this theory is currently an open matter. First we must consider the accuracy of the $\log g$ and T_{eff} measurements that place these objects within the predicted pulsation parameter space. Unfortunately, very low mass WD atmospheres are not well understood. Due to their low surface temperatures ($T_{\text{eff}} \lesssim 9,000 \text{ K}$), the H atmospheres are not sufficiently ionized and neutral broadening of the H absorption lines plays an important role. The theory of neutral broadening is not well understood and may account for significant errors in line widths (Barklem et al. 2000; Allard et al. 2004; Tremblay et al. 2010; private communication, Detlev Koester). As such, the reported errors on $\log g$ and T_{eff} for these objects are always the statistical error of the fit to theoretical atmosphere grids and do not take into account the uncertainties of the theory itself which can increase the uncertainty by as much as a factor of two (private communication, Detlev Koester). Further, the uncertainty of the atmosphere theory is likely not random but rather a shift in a specific direction in the $T_{\text{eff}}\text{--}\log g$ plane, affecting the parameter space location of all very low mass He WDs. This is why NLTT 11748 is such an important eclipsing binary system (Section 5.2). As a potential double-lined spectroscopic eclipsing binary, it could offer high precision *model independent* determinations

of both the mass and radius of the He WD component providing a high precision constraint on its gravity for which any atmospheric gravity measurement must match.

Of added concern is the location of the instability strip “blue” edge itself. In Chapter 2 we derived the “blue” edge to be where pulsation modes of eigenvalues $\ell = 1$ and $n = 1$ were driven. This offers a temperature upper limit to the $\ell = 1$ instability strip because the “blue” edge shifts redward when higher radial orders of n are considered. In the few cases where pulsation mode eigenvalues have been identified observationally (e.g. HL Tau 76, Pech et al. 2006; G117-B15A and R548, Bradley 1998) the highest amplitude observed modes range in n from 1 to several 10s. If very low mass He WDs preferentially only excite the higher radial order modes, then the “blue” edge could shift redward by a few 100 K potentially removing our three high priority candidates from the instability region.

An additional observational concern is whether our detection limits are truly meaningful. Only NLTT 11748 and SDSS J0822+2743 met our fiducial pulsation limit of 10 mmags and only NLTT 11748 was observed more than once. As we have seen in HS 1824+6000 (Figure 4.2 and Table 4.2) that pulsation amplitudes can be small, 3–4 mmag, and vary in detectability from one night to the next. Therefore additional observations may be required of PSR J1012+5307 and SDSS J0822+2753 to both tighten their detection limits and gain multiple epochs of observation so that these null detections can be even more convincing.

Also, many of the lower priority objects we observed were only observed once and/or to detection limits not meeting the fiducial, therefore, additional observations of these objects may be warranted. The two pulsation null detections in SDSS J1300+5904 may offer unique constraints on the canonical ZZ Ceti instability strip. The observed slope of the ZZ Ceti instability strip “blue” edge is determined by only a few objects (Bergeron et al. 2004; Gianninas et al. 2007). If the driving mechanism in the C/O WD ZZ Ceti is similar to that of the He WDs, then SDSS J1300+5904 offers a long lever arm constraint to this slope.

There are many methods that could be employed to solve the problems of finding the theoretical location of the He WD instability strip. We will not touch on the atmospheric models as this is a very active area of research by other research groups. In this dissertation we have concerned ourselves with the theoretical instability strip for very low mass He WDs ($< 0.2 M_{\odot}$). This was because the evolution governing them was relatively simple, requiring only time-independent models. To access the rest of the He WD instability strip ($0.2 < M_{\text{WD}} < 0.45 M_{\odot}$) we will require time-dependent models. Already within the open-source code MESA (Paxton et al. 2011), the tools exist to build state-of-the-art He WD models, they just need to be combined and developed. In our analysis of the pulsational properties of our models, we used a linear adiabatic approximation and applied the Brickhill criterion (Brickhill 1991; Wu & Goldreich 1999) to predict the “blue” edge of the instability strip. The Brickhill criterion has only been tested using

non-adiabatic pulsation modeling for $\log g = 8$ C/O WDs and not at the lower gravities of the He WDs. Therefore, an extension of this non-adiabatic pulsation analysis as well as applying mode amplitude saturation analysis (predicting the pulsation amplitudes themselves) to the models and lower gravities of the He WDs would improve our confidence in the predicted He WD instability region considerably and extend it over all He WD masses.

Appendix A

Very Low Mass Helium White Dwarf Models: Code Description

A.1 Goal

In very low mass helium white dwarfs (He WDs), $M_{WD} \lesssim 0.18\text{--}0.2 M_{\odot}$, simulations find that the H envelope above the helium core burns stably on timescales of several Gyrs. He WDs of higher mass experience unstable nuclear flashes that rapidly remove their H envelopes causing them to evolve on a much shorter timescale of 10s–100s Myrs (Webbink 1975; Papaloizou et al. 1982; Driebe et al. 1999; Serenelli et al. 2002; Panei et al. 2007). These simulations are time-dependent and complex in order to access the total parameter space of He WDs (0.1–0.45 M_{\odot}). However, in very low mass He WDs for most of their evolution the

dominant energy source is H burning in the H/He transition region between envelope and core. Thus, the nuclear timescale (of several Gyrs) dominates the evolution and so diffusive equilibrium is maintained because the diffusive timescales are much shorter. This motivates our static, time-independent, models. Below we describe how our code builds the individual models. Outlined briefly, we solve the equations of stellar structure including hydrostatic balance, heat transport (both radiative and convective), and luminosity generation via nuclear burning. The composition is described fully by equilibrium diffusion. Our luminosity generation is only described by nuclear burning because it dominates all other sources of luminosity (e.g. cooling and gravitational contraction). This leaves our models with essentially two parameters, mass of the He core, M_{core} , and the mass of the H envelope, M_{env} , both of which are defined as the total He and H mass respectively. We then simulate evolution by conserving total WD mass ($M_{\text{WD}} = M_{\text{core}} + M_{\text{env}}$) and moving mass from the envelope to the core (as would occur during the fusion of H to He). This evolution is shown for our models in Figures A.4 and A.5.

Very low mass He WDs could conceivably spend far longer in or near the ZZ Ceti instability strip than the higher mass WDs. We have constructed these models in order to measure and predict the pulsational properties of very low mass He WDs.

A.2 Physics

In this section we discuss the physics that goes into our models: stellar structure, opacities, equation of state (EOS), convection, nuclear burning, and diffusion.

A.2.1 Equations of Stellar Structure

$$\frac{dP}{dr} = -\frac{GM_r}{r^2}\rho \quad (\text{A.1})$$

$$\frac{dM_{r,\text{tot}}}{dr} = 4\pi r^2 \rho \quad (\text{A.2})$$

$$\frac{dM_{r,\text{H}}}{dr} = 4\pi r^2 X \rho \quad (\text{A.3})$$

$$\frac{dL_r}{dr} = 4\pi r^2 \rho \epsilon \quad (\text{A.4})$$

$$\frac{dT}{dr} = -\frac{GM_r T \rho}{r^2 P} \nabla \quad (\text{A.5})$$

$$\frac{dn_{\text{H}}}{dr} = \text{See Section A.2.5} \quad (\text{A.6})$$

$$\nabla = \frac{d \ln T}{d \ln P} \quad (\text{A.7})$$

$$\nabla_{\text{rad}} = \frac{3}{16\pi acG} \frac{P \kappa}{T^4} \frac{L_r}{M_r} \quad (\text{A.8})$$

$$\nabla_{\text{ad}} = \frac{\Gamma_2 - 1}{\Gamma_2} \quad (\text{A.9})$$

In general we solve six ODEs, solving for pressure (Equation A.1), interior mass (Equation A.2), interior H mass (Equation A.3), luminosity (Equation A.4), temperature (Equation A.5), and H number density (Equation A.6), and we have nine unknown quantities: mass of the core M_{core} , mass of the envelope M_{env} , core

($r = M_r = 0$) temperature T_{core} , core density ρ_{core} or pressure P_{core} , core H mass abundance X_{core} , surface ($M_{r,\text{tot}} = M_{\text{core}} + M_{\text{env}} = M_{\text{tot}}$ and $M_{r,\text{H}} = M_{\text{env}} = M_{\text{H}}$) radius R_{surf} , surface luminosity L_{surf} , surface temperature T_{eff} , and surface density ρ_{surf} or surface pressure P_{surf} . There are additional implied boundary conditions where the core luminosity is $L_{\text{core}} = 0$ and the surface H abundance is $X_{\text{surf}} = 1$. The surface density, pressure, and temperature are all related via the radiative zero solution given the output luminosity and surface radius (the reality of this statement is far more complex and will be discussed later) and so reduce our nine unknowns to eight. Of the eight unknowns, we select two to be parameters to obtain a unique solution. For the purposes of this discussion, we will elevate M_{core} and M_{env} to the status of parameter. Profiles of various quantities for an example model are shown in Figures A.1, A.2, and A.3.

A.2.2 Microphysics: Opacity and Equation of State

All portions of the code use the same microphysics when evaluating the opacities and the equation of state (EOS). We use MESA (Modules for Experiments in Stellar Astrophysics written by Paxton et al. 2011) to evaluate this microphysics. The MESA EOS modules utilize a blended and smoothed combination of the HELM (Timmes & Swesty 2000), OPAL (Rogers & Nayfonov 2002), and SCVH (Saumon et al. 1995) equations of state. The MESA opacity modules utilize a blended and smoothed combination of the OPAL Type 1 and Type 2 tables (Igle-

sias & Rogers 1993, 1996) and the Ferguson (Ferguson et al. 2005) opacities with the overall addition of the effects of electron conduction from Cassisi et al. (2007). The opacity profile of an example model is shown in Figure A.3.

A.2.3 Convection

A fluid parcel is unstable to convection when the Schwarzschild Criterion is satisfied:

$$\nabla_{\text{rad}} > \nabla_{\text{ad}} \rightarrow (\text{convectively unstable}). \quad (\text{A.10})$$

When this criterion is satisfied, energy transport is carried out almost exclusively through the physical movement of fluid parcels. At all other times, energy transport is carried out exclusively through radiative transport.

Our code is able to deal with convection in three ways: ignore convection, $\nabla = \nabla_{\text{rad}}$; use the adiabatic approximation, $\nabla = \nabla_{\text{ad}}$; or use Mixing Length Theory (MLT), $\nabla = \nabla_{\text{MLT}}$. Our code currently allows for two variations on the same MLT. One is precisely as defined in Hansen et al. (2004), and the other defined in the same way excepting the mixing length which is defined as the lesser of the local pressure scale height or distance to the top of the convection zone.

The models discussed in this dissertation always use standard MLT with a mixing length $\alpha = 1.0$. All heat transport gradient (the $d \ln T / d \ln P_s$) profiles for an example model are shown in Figure A.3. Notice the superadiabaticity, caused by MLT, of the actual gradient within the convection zone near the surface.

A.2.4 Nuclear Energy Generation

Our code evaluates nuclear energy generation in one of two ways: the MESA module or analytically. The MESA module takes as input the composition, temperature, and density and is based on Timmes (1999). Our composition is always H, ^4He , and ^3He in equilibrium abundance (calculated below) and we only ever use the most basic nuclear network in MESA.

Our analytic energy generation goes through the entire proton-proton (PP) chains and the proton-electron-proton (PEP) chains, via the following rate calculations:

$$\epsilon = \frac{\Gamma Q_{\text{eff}}}{\rho} \quad [\text{ergs g}^{-1} \text{ s}^{-1}], \quad (\text{A.11})$$

$$\Gamma = N_A \rho X^2 r \quad [\text{reactions s}^{-1}], \quad (\text{A.12})$$

$$r_{\text{pp}} = 4.01 \times 10^{-15} \rho T_9^{-2/3} \exp\left(-3.38 T_9^{-1/3}\right) \times \\ \left(1 + 0.123 T_9^{1/3} + 1.090 T_9^{2/3} + 0.938 T_9\right) \\ [\text{reactions g}^{-1} \text{ s}^{-1}], \quad (\text{A.13})$$

$$r_{\text{pep}} = 1.36 \times 10^{-20} \rho^2 y_e T_9^{-7/6} \exp\left(-3.38 T_9^{-1/3}\right) \times \\ \left(1 - 0.729 T_9^{1/3} + 9.82 T_9^{2/3}\right) \quad [\text{reactions g}^{-1} \text{ s}^{-1}], \quad (\text{A.14})$$

$$Q_{\text{eff,pp}} = Q_{\text{eff,pep}} = (1.442 + 5.493) \quad [\text{MeV}], \quad (\text{A.15})$$

where N_A is Avogadro's number. For the models of this dissertation, the PEP chain generates $\approx 1\%$ the energy of the PP chain.

A concern for using this simplistic approach for the entire PP and PEP chains

is our models may contain nuclear burning at temperatures and densities low enough that the completion step of ${}^3\text{He}$ on ${}^3\text{He}$ or ${}^4\text{He}$, may not occur on a shorter timescale than the evolutionary timescale of the envelope mass. Therefore, in our models we calculate the lifetimes of ${}^3\text{He}$ with respect to the two reactions with ${}^3\text{He}$ and ${}^4\text{He}$ via the following rate calculations:

$$n_{X_i} = \frac{\rho X_i}{m_{X_i}}, \quad (\text{A.16})$$

$$\Gamma = N_A \rho X_{3\text{He}} X_{3 \text{ or } 4\text{He}} \quad [\text{reactions s}^{-1}], \quad (\text{A.17})$$

$$l_{3\text{He}+3\text{He}\rightarrow 4\text{He}+2\text{p}} = \frac{n_{3\text{He}}}{2\Gamma_{3\text{He}+3\text{He}\rightarrow 4\text{He}+2\text{p}}}, \quad (\text{A.18})$$

$$l_{3\text{He}+4\text{He}\rightarrow 7\text{Be}+\gamma} = \frac{n_{3\text{He}}}{\Gamma_{3\text{He}+3\text{He}\rightarrow 7\text{Be}+\gamma}}, \quad (\text{A.19})$$

$$\begin{aligned} r_{3\text{He}+3\text{He}\rightarrow 4\text{He}+2\text{p}} &= 6.04 \times 10^{10} \rho T_9^{-1/3} \exp\left(-12.276T_9^{-1/3}\right) \times \\ &\quad \left(1 + 0.034T_9^{1/3} - 0.522T_9^{2/3} - \right. \\ &\quad \left. 0.124T_9 + 0.353T_9^{4/3} + 0.213T_9^{5/3}\right) \\ &\quad [\text{reactions g}^{-1} \text{ s}^{-1}], \quad (\text{A.20}) \end{aligned}$$

$$\begin{aligned} r_{3\text{He}+4\text{He}\rightarrow 7\text{Be}+\gamma} &= 5.61 \times 10^6 \rho \left(T_9 \frac{1}{1 + 0.0495T_9}\right)^{5/6} \times \\ &\quad T_9^{-3/2} \exp\left(-12.826T_9^{-1/3}\right) \\ &\quad [\text{reactions g}^{-1} \text{ s}^{-1}]. \quad (\text{A.21}) \end{aligned}$$

Notice that the ${}^3\text{He}$ abundance ($X_{3\text{He}}$) cancels out completely in Equation (A.19) but not in Equation (A.18). Therefore, we must calculate an equilibrium value for ${}^3\text{He}$ to find its lifetime in reactions on itself.

We calculate the equilibrium abundance of ${}^3\text{He}$ by assuming that the deu-

terium lifetime is sufficiently shorter than all other lifetimes so that it is also in equilibrium. Therefore, the differential equation governing ${}^3\text{He}$ creation and destruction is:

$$\frac{dX_{{}^3\text{He}}}{dt} = \frac{r_{\text{pp}}}{\rho} \frac{X_{\text{H}}^2}{2} - \frac{r_{{}^3\text{He}+{}^3\text{He}\rightarrow{}^4\text{He}+2\text{p}}}{\rho} X_{{}^3\text{He}}^2. \quad (\text{A.22})$$

Which assumes that the reaction rate of ${}^3\text{He}$ on ${}^4\text{He}$ is much slower than ${}^3\text{He}$ on itself. This builds to an equilibrium at,

$$\left(\frac{X_{{}^3\text{He}}}{X_{\text{H}}} \right)_{\text{equilibrium}} = \left(\frac{r_{\text{pp}}}{2r_{{}^3\text{He}+{}^3\text{He}\rightarrow{}^4\text{He}+2\text{p}}} \right)^{1/2}. \quad (\text{A.23})$$

This equilibrium value itself is also dependent upon the assumption that the reaction rate of ${}^3\text{He}$ on itself is faster than all other reactions at equilibrium.

In the parameter space of this dissertation, the PP and PEP chains are always complete where the nuclear energy generation is important. For the models of this dissertation, the MESA nuclear network module was used. An example of the nuclear energy generation profile can be found in Figure A.3.

A.2.5 Composition Profile

The composition profile of our models is defined by the equilibrium diffusive profile. Ions and their electrons must be suspended by an electric field in order to maintain overall neutral charge in the presence of gravity. In a multicomponent plasma this causes the ions to separate and layer by ion mass with diffusive tails defining their boundaries. In our models we are only concerned with H and He

ions, however, it is easy to consider an infinite number of ions under condition of total ionization. For our purposes we track only the dn_{H}/dr (Equation A.6) differential equation since it is related trivially to the He and electron differential equations through charge neutrality and our assumption of total ionization. The result of equilibrium diffusion is best illustrated by the composition profile found in Figure A.2. Notice the long diffusive tails of both H and He into the other.

Partial Pressure Equations and the Electric Field

Assuming only hydrostatic equilibrium we write down the partial pressure gradients as follows,

$$\frac{dP_i}{dr} = -n_i (A_i m_p g - Z_i e E), \quad (\text{A.24})$$

$$\frac{dP_e}{dr} = -n_e (m_e g + e E), \quad (\text{A.25})$$

$$dP_X = \frac{\partial P_X}{\partial n_X} dn_X + \frac{\partial P_X}{\partial T} dT. \quad (\text{A.26})$$

Where X is to be replaced by H, He (or any ion) and electrons as needed. Combining these and solving for the number density gradients we get,

$$\frac{dn_i}{dr} = - \left(\frac{\partial P_i}{\partial n_i} \right)^{-1} n_i \left[A_i m_p g - Z_i e E + \frac{1}{n_i} \frac{\partial P_i}{\partial T} \frac{dT}{dr} \right], \quad (\text{A.27})$$

$$\frac{dn_e}{dr} = - \left(\frac{\partial P_e}{\partial n_e} \right)^{-1} n_e \left[m_e g + e E + \frac{1}{n_e} \frac{\partial P_e}{\partial T} \frac{dT}{dr} \right]. \quad (\text{A.28})$$

By demanding charge neutrality, $n_e - \sum n_i Z_i = 0$, we can solve these equations for the electric field,

$$eE = \frac{\sum \left(\frac{\partial P_i}{\partial n_i}\right)^{-1} Z_i \left(n_i A_i m_p g + \frac{\partial P_i}{\partial T} \frac{dT}{dr}\right) - \left(\frac{\partial P_e}{\partial n_e}\right)^{-1} \left(n_e m_e g + \frac{\partial P_e}{\partial T} \frac{dT}{dr}\right)}{\left(\frac{\partial P_e}{\partial n_e}\right)^{-1} n_e + \sum \left(\frac{\partial P_i}{\partial n_i}\right)^{-1} n_i Z_i^2}. \quad (\text{A.29})$$

Ionic Equation of State

For the situations we are concerned, equilibrium diffusion in helium core white dwarfs, the ideal gas law provides an accurate equation of state for the ions. Therefore, we may reduce the electric field equation using the ideal gas law for the ionic portion,

$$eE = \frac{\sum Z_i n_i \left(A_i m_p g + k_B \frac{dT}{dr}\right) - k_B T \left(\frac{\partial P_e}{\partial n_e}\right)^{-1} \left(n_e m_e g + \frac{\partial P_e}{\partial T} \frac{dT}{dr}\right)}{k_B T \left(\frac{\partial P_e}{\partial n_e}\right)^{-1} n_e + \sum n_i Z_i^2}. \quad (\text{A.30})$$

Electron Equation of State

We obtain the electron equation of state from MESA by explicitly calling the HELM EOS (an electron-positron equation of state using the Helmholtz free energy based on Timmes & Swesty 2000). This equation of state is only valid in areas of high density and pressure. The H/He transition region fortunately occurs in the region of validity.

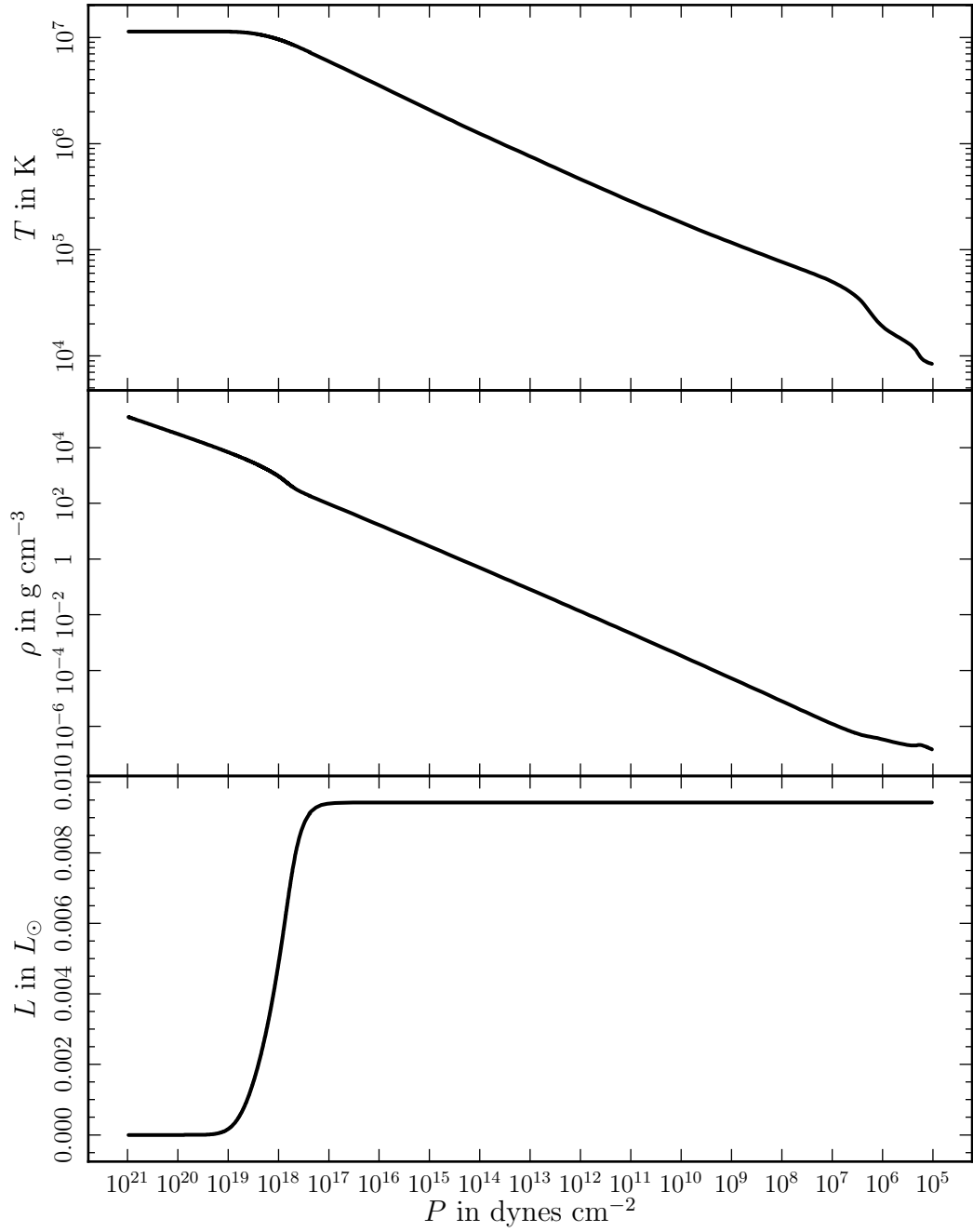


Figure A.1: The profiles for temperature (top panel), density (middle panel), and luminosity (bottom panel) against pressure (core to left, surface to right) for a $M_{\text{WD}} = 0.17 M_{\odot}$ with a $M_{\text{env}} = 3.15 \times 10^{-3} M_{\odot}$. This represents a typical predicted pulsator also analyzed in Chapter 2.

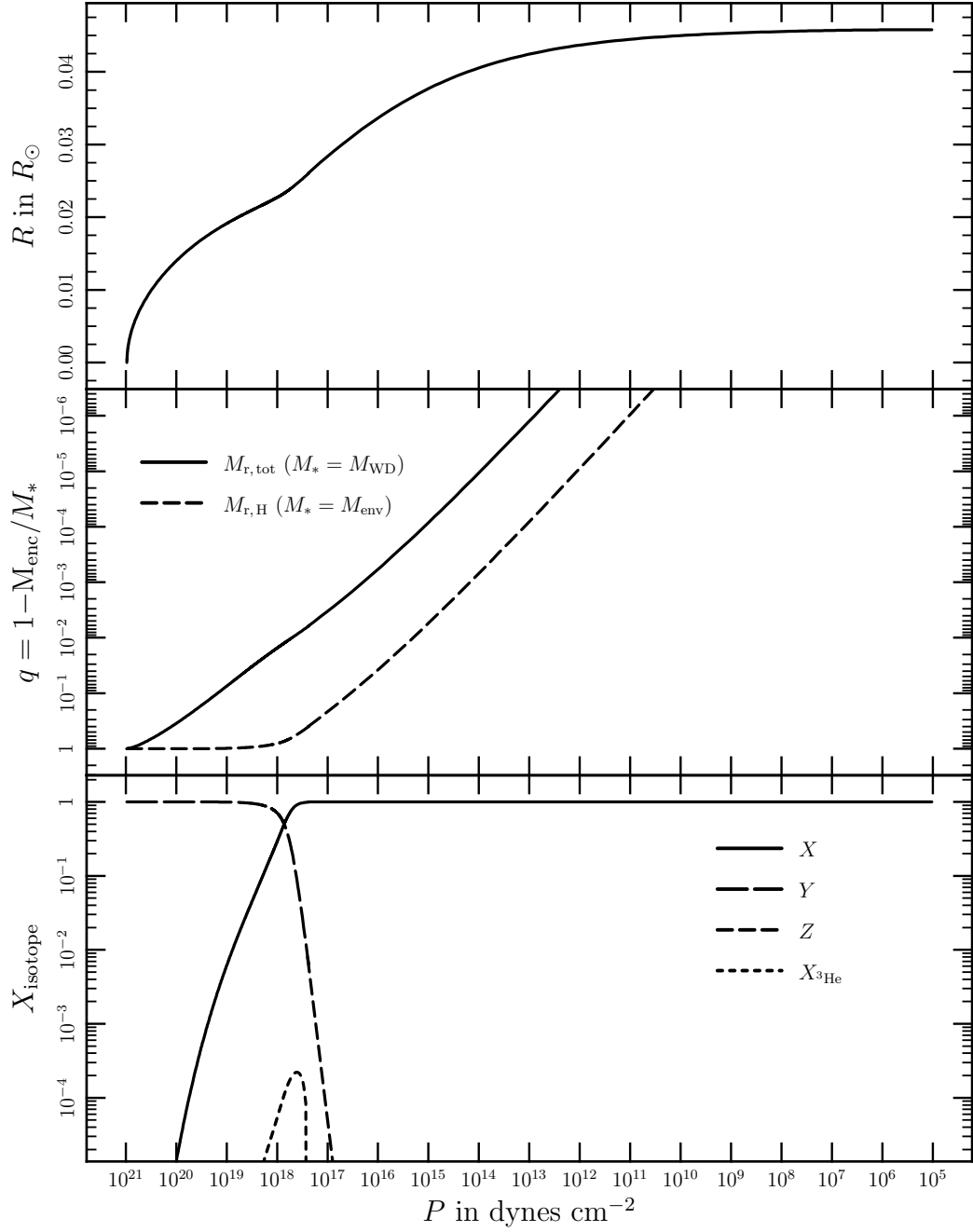


Figure A.2: The profiles for radius (top panel), total mass interior and hydrogen mass interior (middle panel), and composition (bottom panel) against pressure (core to left, surface to right) for a $M_{\text{WD}} = 0.17 M_{\odot}$ with a $M_{\text{env}} = 3.15 \times 10^{-3} M_{\odot}$. This represents a typical predicted pulsator also analyzed in Chapter 2.

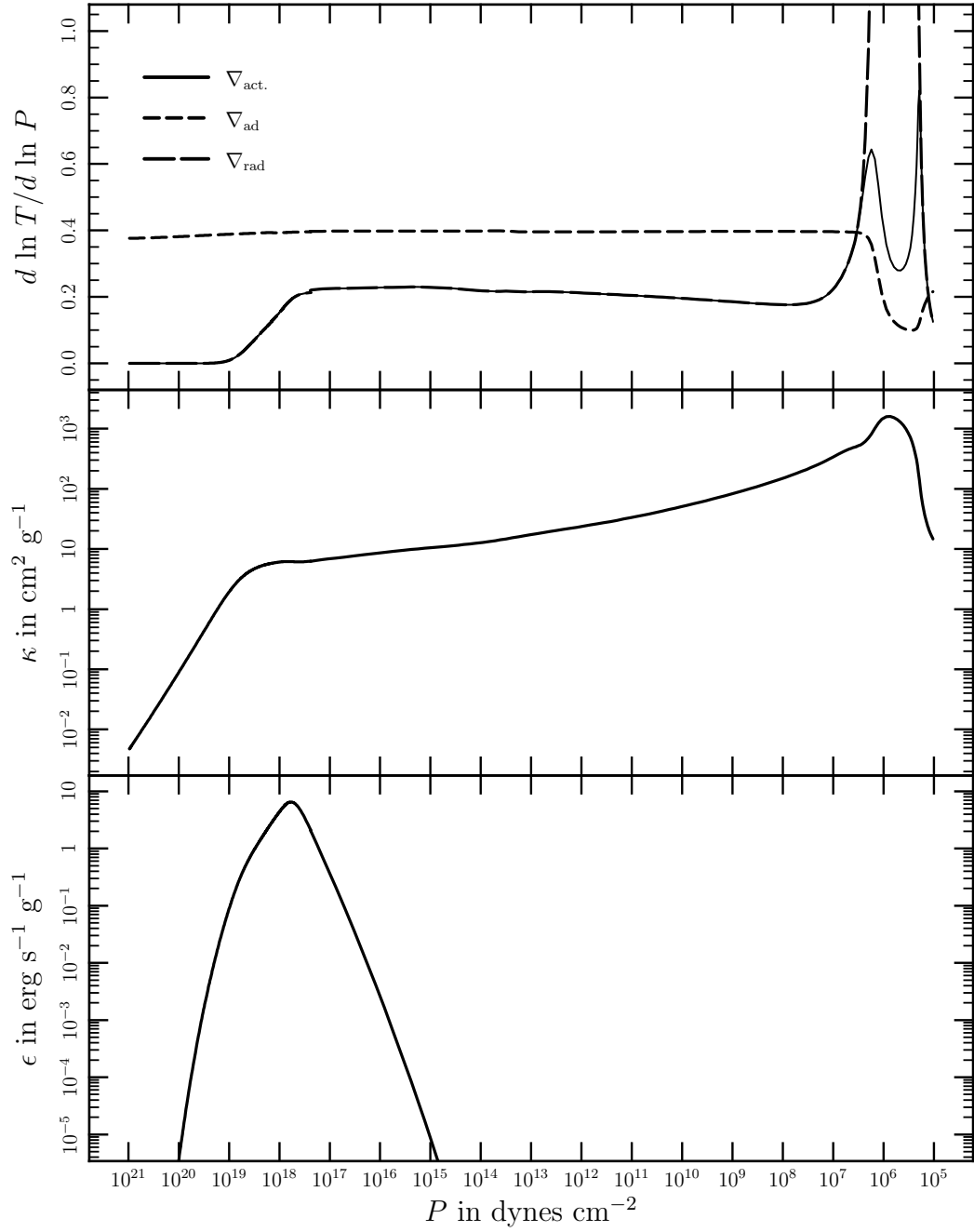


Figure A.3: The profiles for heat transport gradients ($d \ln T / d \ln P$) (top panel), opacity (middle panel), and nuclear energy generation (bottom panel) against pressure (core to left, surface to right) for a $M_{\text{WD}} = 0.17 M_{\odot}$ with a $M_{\text{env}} = 3.15 \times 10^{-3} M_{\odot}$. This represents a typical predicted pulsator also analyzed in Chapter 2.

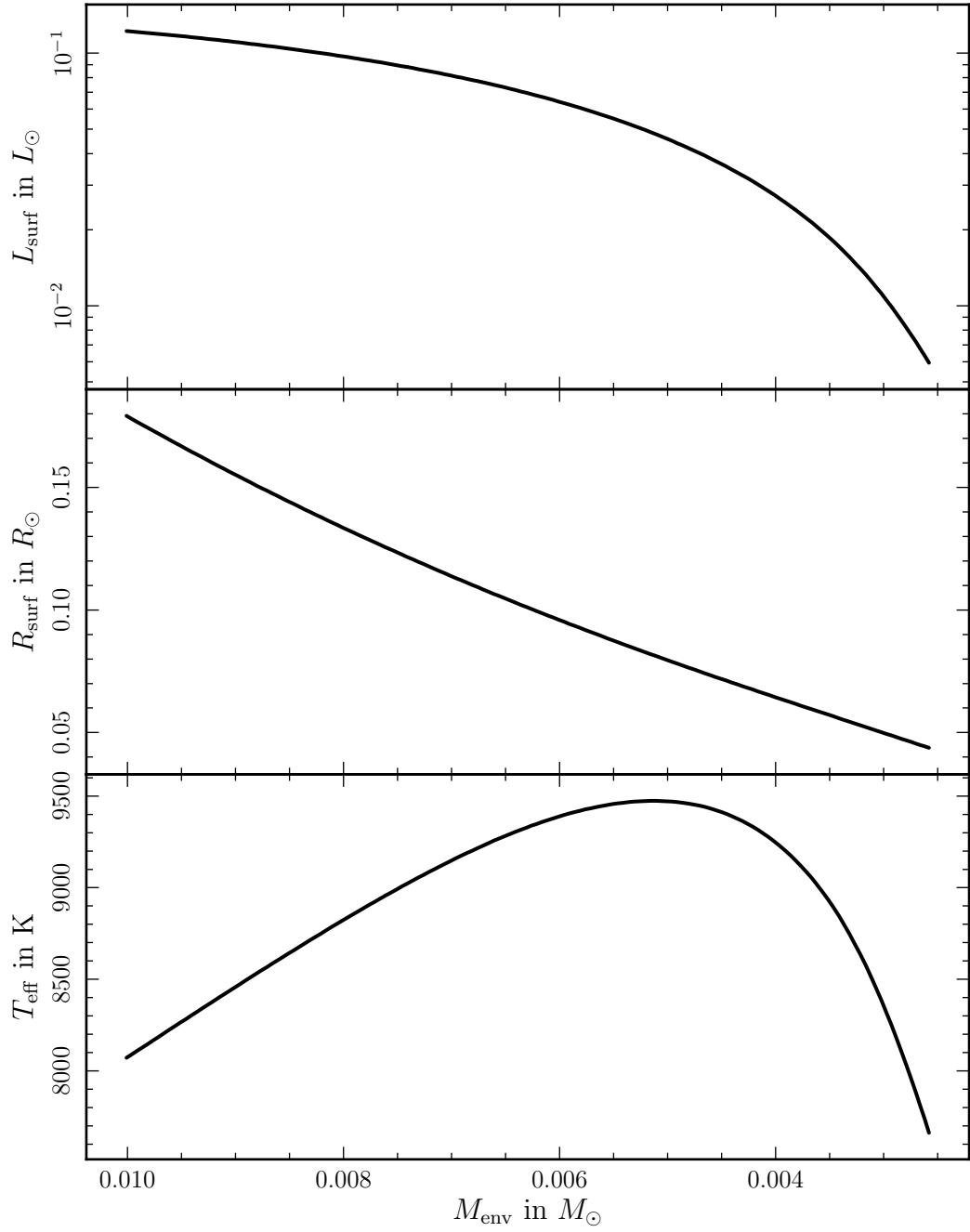


Figure A.4: The family of models for a $M_{\text{WD}} = 0.17 M_{\odot}$ WD. Evolution is simulated (from left to right) by conserving $M_{\text{tot}} = M_{\text{WD}}$ and decreasing the H envelope mass (M_{env}) and adding to the core mass. We show the evolution of surface luminosity (top panel), surface radius (middle panel), and effective temperature (bottom panel).

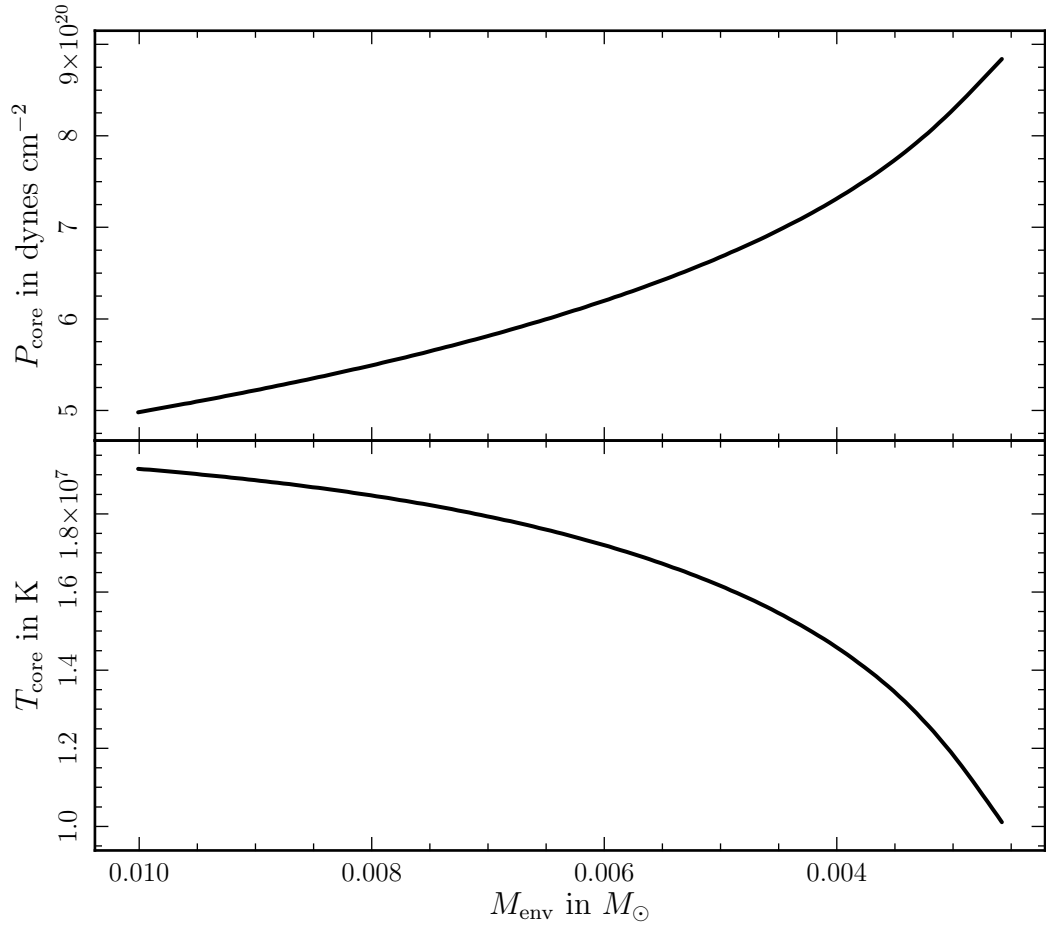


Figure A.5: The family of models for a $M_{\text{WD}} = 0.17 M_{\odot}$ WD. Evolution is simulated (from left to right) by conserving $M_{\text{tot}} = M_{\text{WD}}$ and decreasing the H envelope mass (M_{env}) and adding to the core mass. We show the evolution of core pressure (top panel) and core temperature (bottom panel).

A.3 The Code

The code itself is split into three regions: the core and two envelope regions. We have distinguished two envelope regions for reasons that will be made clear below. We use an explicit Runge-Kutta ODE integrator of order 5 (implemented by a MESA module) to integrate the equations of stellar structure from the surface toward the core and from the core toward the surface. We evaluate the shooting problem by iterating the integrations and forcing them to meet between the core region and lowest surface region via a Newton-Raphson method (also implemented by a MESA module). We have chosen to solve the shooting problem at a point interior to the surface of the WD due to numerical difficulties uncovered by integrating from the core to the surface. Given that our goal was to use the masses of the core and the envelope as parameters, this requires us to iterate the remaining six variables (mass interior, hydrogen mass interior, hydrogen number density, temperature, pressure, and luminosity) to a model that satisfies the equations of stellar structure. If these variables were not already sufficiently close to the real solution, two behaviors of the integrator would arise. In one case, the integrator would find parameter space that lead to a stiff behavior in the ODE equations that resulted in large numerical error and the inability of the solution to find the outer radiative zero solution. The second case resulted in the integrator failing before reaching the surface. The level of precision required to *not* be in one of these two regions of parameter space was sufficiently high that we decided to

abandon this method. Further, by starting part of the integration at the surface allows us to force it to always be on a radiative zero solution by calculating the grey atmosphere approximation.

A.3.1 The Grey Atmosphere

The boundary condition at the surface is defined by the radiative zero solution given the output luminosity, L_{surf} , and the surface radius, R_{surf} . However, this is not simple to describe in mass or radius coordinates without significant approximation. Of further concern is that the observed surface may actually exist in a convection zone where the heat transport is no longer radiative. The grey atmosphere approximation allows us to use optical depth, τ , as our coordinate and to start at low enough optical depth that the assumption of radiative heat transport is safe. We then integrate toward the *true* observed surface at $\tau = 2/3$. In the atmosphere, the radius and mass are changing slowly enough that the plane parallel approximation is appropriate. Therefore, only hydrostatic equilibrium needs to be satisfied (obviously, there is no nuclear burning in the atmosphere). We recast the equation of hydrostatic equilibrium, Equation (A.1), in terms of optical depth through the definition, $d\tau = -\kappa\rho dr$:

$$\frac{dP}{d\tau} = \frac{g}{\kappa}. \quad (\text{A.31})$$

The MESA opacities are explicitly dependent on temperature and density. Following Hansen et al. (2004), we use the Eddington approximation for temperature

as a function of optical depth,

$$T(\tau) = \left[\frac{3}{4} \left(\tau + \frac{2}{3} \right) \right]^{1/4} T_{\text{eff}}. \quad (\text{A.32})$$

To obtain the density, we could turn to our equation of state, unfortunately, the MESA EOS is also explicitly dependent on temperature and density. Therefore, to obtain density given pressure, MESA must perform a root-find on the EOS tables, a numerically expensive task. To increase the computer evaluation speed, we perform the following transformation into density:

$$d\rho = \left[dP - \left(\frac{dP}{dT} \Big|_{\rho} \right) dT \right] \left(\frac{dP}{d\rho} \Big|_T \right)^{-1}. \quad (\text{A.33})$$

The $dP/dT|_{\rho}$ and $dP/d\rho|_T$ terms are explicitly determined in the EOS and not numerically expensive.

We determine the observed surface properties by integrating Equation (A.31) from $\tau = 10^{-4}$ to $2/3$. We obtain the initial density through linear approximation from $d\rho/d\tau$ assuming density is zero at zero optical depth. As stated earlier, this entire analysis assumes radiative energy transport. However, in our models, this is not always the case as a convection zone may develop before we reach the $\tau = 2/3$ surface. Therefore, during our integration of Equation (A.31), we test for convective instability at each integration step via the Schwarzschild Criterion, Equation (A.10). If a step becomes unstable to convection, we stop the integration and transfer the properties to the full surface toward core integrator as if the properties were those of the true surface.

A.3.2 Surface toward Core: Outer Layer

As mentioned earlier, the envelope portion of the code is partitioned into two sections. We start with the outermost portion, that section that receives its initial conditions from the grey atmosphere. In this section we integrate Equations (A.1), (A.2), and (A.5), where $\nabla = \nabla_{\text{rad}}$, with respect to radius. Additionally, all equations are integrated using logarithmic variables. We neglect integrating Equation (A.4) as we truncate this section long before energy generation from nuclear burning significantly alters the luminosity profile. We also neglect integrating Equations (A.3) and (A.6) because the composition gradient is smaller than computer precision and so tracking it can introduce numerical artifacts. We choose to integrate in radius as tests on several model WD and envelope masses showed it to be computationally faster than integrating in mass, these tests were not extensive and may not be true for all of parameter space, however, the computational gains were only a few percent. To increase computational speed, we transform Equation (A.1) to $d\rho/dr$ via the transformation Equation (A.33) and explicitly follow density instead of pressure.

In those situations where the grey atmosphere finds a radiative surface, a subroutine is setup to test each step of integration for convective instability via Equation (A.10) and then interpolate (at order four in the Runge-Kutta scheme) to find the more precise top of the convection zone. When a convection zone is found, the integrator is restarted and ∇ is replaced with ∇_{conv} . A separate

subroutine also exists to find the bottom of the convection zone in much the same way as the top of the convection zone is found. The Outer Layer integration is terminated when pressure reaches 10^{10} dynes cm^{-2} and all state information is then transferred to the Inner Layer integrator.

A.3.3 Surface toward Core: Inner Layer

In this section we integrate Equations (A.1), (A.2), (A.3), (A.4), (A.5), and (A.6) with respect to radius. Additionally, all equations are integrated using logarithmic variables. As in the previous section, cursory tests showed integrations in radius to be faster than in mass. We no longer neglect luminosity or the composition gradient.

It is expected in this section that the integration either starts in a convection zone or never develops one. Therefore, we only implement a subroutine to find the bottom of the convection zone. The Inner Layer integrator is terminated when when the hydrogen mass fraction, X , reaches a predetermined boundary value, X_b . At this point, the state information, specifically ρ , L , R , T , and M_H , at this boundary is compared to the same values of the Core toward Surface integration, which will all be described shortly. Since both Core toward Surface and Surface toward Core integrations terminate at the same X_b , this already will match perfectly.

A.3.4 Core toward Surface

In this section we integrate Equations (A.1), (A.2), (A.3), (A.4), (A.5), and (A.6) with respect to radius. As in the previous sections, cursory tests showed integration in radius to be faster than mass.

The Core toward Surface integrator is terminated when when the hydrogen mass fraction, X , reaches a predetermined boundary value, X_b . At this point, the state information, specifically ρ , L , R , T , and M_H , at this boundary is compared to the same values of the Surface toward Core integration.

For the models used in this dissertation, X_b was set as 0.1. For the WD masses desired, this offered the most numerically stable shooting boundary giving the widest range of envelope masses.

A.3.5 Iterating to a Solution

We use a Newton-Raphson iteration method to iterate an individual model's state vector toward a solution where the Surface toward Core and Core toward Surface integrators meet with sufficient precision. We have elevated M_{core} and M_{env} to model parameters, meaning that we state these variables and then solve for the remaining state vector. The state vector that we iterate over includes the core density ρ_{core} , the core temperature T_{core} , the core hydrogen abundance X_{core} , the surface luminosity L_{surf} , and the surface radius R_{surf} .

For this dissertation we generated models for $M_{\text{WD}} = 0.15\text{--}0.20 M_{\odot}$ step-

ping by $0.01 M_{\odot}$. For each WD mass we produce models with $M_{\text{env}}=1.0\times 10^{-3}$ – $1.0\times 10^{-2} M_{\odot}$ in steps of $0.05\times 10^{-3} M_{\odot}$. However, for some WD masses (most notably the higher masses) we were unable to construct some of the lower mass envelopes due to numerical convergence issues. The family of models for a $0.17 M_{\odot}$ WD are show in Figures A.4 and A.5.

Appendix B

Adiabatic Pulsations

B.1 Derivation Framework

¹ Calculating stellar pulsations requires both an understanding of the underlying stellar structure as well as an understanding of the perturbations on top of that structure. Therefore we must define specific notation that we will be used throughout this Appendix.

The background star will be notated with the following property variables:

$$\rho_0(r), P_0(r), T_0(r) \text{ and } \{X_{i,0}(r)\},$$

where $\{X_{i,0}(r)\}$ represents the vector of all isotopic abundances. The Lagrangian displacement vector will be represented by $\vec{\xi}(\vec{x}, t)$. The perturbed state variables

¹An outline of this derivation can be found in Unno et al. (1989).

will be denoted as follows:

$$\rho(r), P(r), T(r) \text{ and } \{X_i(r)\}.$$

Note that these state variables are full thermodynamic variables. As such, Eulerian perturbations, where perturbations are measured at a specific position with respect to the background star, will be denoted with δ , e.g. $\rho(\vec{x}) \rightarrow \rho(\vec{x}) + \delta\rho(\vec{x}, t)$. Lagrangian perturbations, where perturbations are measured with respect to a specific fluid element, will be denoted with Δ , e.g. $\rho(\vec{x}) \rightarrow \rho(\vec{x}) + \Delta\rho(\vec{x}, t)$. In an operational sense, these two perturbations are related via

$$\Delta = \delta + \vec{\xi} \cdot \vec{\nabla}. \quad (\text{B.1})$$

B.2 The Energy Equation

When considering a fluid element, we make the assumption that all energy transport between it and the background fluid occurs adiabatically. Therefore, it is best to expand the state variable ρ in terms of pressure, composition and entropy, rather than temperature. The full derivative of ρ is therefore,

$$\begin{aligned} \frac{d\rho}{\rho} &= \left. \frac{\partial\rho}{\partial P} \right|_{S, \{X_i\}} \frac{dP}{\rho} + \left. \frac{\partial\rho}{\partial S} \right|_{P, \{X_i\}} \frac{dS}{\rho} + \sum_{i=1}^{I-1} \left. \frac{\partial\rho}{\partial X_i} \right|_{S, P, \{X_{j \neq i}\}} \frac{dX_i}{\rho}, \\ &= \left. \frac{\partial \ln \rho}{\partial \ln P} \right|_{S, \{X_i\}} \frac{dP}{P} + \left. \frac{\partial \ln \rho}{\partial S} \right|_{P, \{X_i\}} dS + \\ &\quad \sum_{i=1}^{I-1} \left. \frac{\partial \ln \rho}{\partial \ln X_i} \right|_{S, P, \{X_{j \neq i}\}} \frac{dX_i}{X_i}, \quad (\text{B.2}) \end{aligned}$$

where the sum over all isotopes, I , has been reduced by one owing to the condition that $\sum X_i = 1$. If we recognize

$$\Gamma_1 = \left. \frac{\partial \ln P}{\partial \ln \rho} \right|_{S, \{X_i\}}, \quad (\text{B.3})$$

and, since we are assuming adiabaticity, $ds = 0$, the second term vanishes, and recognize we are implicitly following a single fluid element, then Equation (B.2) reduces to the following with Lagrangian derivatives

$$\frac{\Delta \rho}{\rho_0} = \frac{1}{\Gamma_1} \frac{\Delta P}{P_0}, \quad (\text{B.4})$$

note that the composition gradient also goes to zero as we assume our fluid parcel does not have time to chemically diffuse with its surrounding fluid. We may recast this equation into the Eulerian view via the transformation Equation (B.1) while making the assumption here that ρ_0 and P_0 are spherically symmetric,

$$\frac{\delta \rho}{\rho_0} + \frac{\xi_r}{\rho_0} \frac{d\rho_0}{dr} = \frac{\delta P}{\Gamma_1 P_0} + \frac{\xi_r}{\Gamma_1 P_0} \frac{dP_0}{dr}, \quad (\text{B.5})$$

and rearranging terms and pulling out “suggestive” coefficients,

$$\frac{\delta \rho}{\rho_0} = \frac{\delta P}{\Gamma_1 P_0} + \xi_r \frac{1}{g} \left[-g \left(\frac{d \ln \rho_0}{dr} - \frac{1}{\Gamma_1} \frac{d \ln P_0}{dr} \right) \right], \quad (\text{B.6})$$

where g is the local acceleration. We recognize the squared Brunt-Väisälä frequency, N^2 , as the term in the square brackets. While N certainly has units of frequency, its role as a characteristic frequency of a fluid will become more clear later. If we also recognize the adiabatic sound speed, $c_s^2 = \Gamma_1 P / \rho$, we are now left

with,

$$\delta\rho = \frac{\delta P}{c_s^2} + \frac{\rho_0}{g} N^2 \xi_r. \quad (\text{B.7})$$

B.2.1 Aside: The Brunt-Väisälä Frequency

For simplicity, the notational nuances of the rest of these notes do not apply to this subsection. As was pointed out in the last section, the Brunt-Väisälä frequency is simply,

$$N^2 = -g \left(\frac{d \ln \rho}{dr} - \frac{1}{\Gamma_1} \frac{d \ln P}{dr} \right). \quad (\text{B.8})$$

If we assume hydrostatic equilibrium and take the definition of the pressure scale height,

$$\frac{d \ln P}{dr} = -\frac{\rho g}{P} = -\frac{1}{\lambda_P}, \quad (\text{B.9})$$

then we massage Equation (B.8) into,

$$N^2 = \frac{g}{\lambda_P} \left(\frac{d \ln \rho}{d \ln P} - \frac{1}{\Gamma_1} \right). \quad (\text{B.10})$$

If we take density to be a function of pressure, entropy and composition we expand the total derivative of density in terms of its partial derivatives as was done in Equation (B.2). Recognizing Γ_1 and taking the derivative with respect to pressure we get,

$$\frac{d \ln \rho}{d \ln P} = \frac{1}{\Gamma_1} + \left. \frac{\partial \ln \rho}{\partial S} \right|_{P, \{X_i\}} \frac{dS}{d \ln P} + \sum_{i=1}^{I-1} \left. \frac{\partial \ln \rho}{\partial X_i} \right|_{S, P, \{X_{j \neq i}\}} \frac{dX_i}{d \ln P}, \quad (\text{B.11})$$

and inserting into Equation (B.10),

$$N^2 = \frac{g}{\lambda_P} \left(\frac{\partial \ln \rho}{\partial S} \Big|_{P, \{X_i\}} \frac{dS}{d \ln P} + \sum_{i=1}^{I-1} \frac{\partial \ln \rho}{\partial X_i} \Big|_{S, P, \{X_{j \neq i}\}} \frac{dX_i}{d \ln P} \right), \quad (\text{B.12})$$

and we are then left to the task of rewriting $\partial \ln \rho / \partial S|_{P, \{X_i\}}$ and $\partial \ln \rho / X_i|_{S, P, \{X_i\}}$ in terms of quantities more readily available from our equation of state package of choice. In our case, the EOS takes density, temperature and composition as independent variables. Therefore, to get at $\partial \ln \rho / \partial S|_{P, \{X_i\}}$ we consider the First Law of Thermodynamics and enthalpy,

$$\begin{aligned} d\varepsilon &= TdS - Pd \left(\frac{1}{\rho} \right), \\ dH &= d \left(\varepsilon + \frac{P}{\rho} \right) = TdS + \frac{1}{\rho} dP. \end{aligned} \quad (\text{B.13})$$

Then by taking the second derivative of enthalpy with respect to pressure and entropy (for simplicity, we will assume constant composition for all partial derivatives) we get,

$$\begin{aligned} \frac{\partial^2 H}{\partial S \partial P} &= \frac{\partial}{\partial S} \left(\frac{\partial H}{\partial P} \Big|_S \right) \Big|_P = \frac{\partial}{\partial P} \left(\frac{\partial H}{\partial S} \Big|_P \right) \Big|_S, \\ &\frac{\partial T}{\partial P} \Big|_S = \frac{\partial}{\partial S} \left(\frac{1}{\rho} \right) \Big|_P. \end{aligned} \quad (\text{B.14})$$

Then by taking the second derivative to be zero we get,

$$\frac{\partial \ln \rho}{\partial S} \Big|_P = -\frac{\rho T}{P} \nabla_{\text{ad}}. \quad (\text{B.15})$$

To obtain $dS/d \ln P$ we take entropy to be a function of pressure and temperature such that the full derivative becomes,

$$\frac{dS}{d \ln P} = \frac{\partial S}{\partial \ln P} \Big|_T + \frac{\partial S}{\partial \ln T} \Big|_P \frac{d \ln T}{d \ln P}. \quad (\text{B.16})$$

We then use the cyclic relationship of,

$$\left(\frac{\partial S}{\partial \ln P}\right)_T \left(\frac{\partial \ln T}{\partial S}\right)_P \left(\frac{\partial \ln P}{\partial \ln T}\right)_S = -1, \quad (\text{B.17})$$

and recognize,

$$c_P = \frac{\partial S}{\partial \ln T}\bigg|_P, \quad (\text{B.18})$$

to obtain,

$$\frac{dS}{d \ln P} = c_P (\nabla - \nabla_{\text{ad}}). \quad (\text{B.19})$$

Using the definition,

$$\frac{\partial \ln T}{\partial \ln \rho}\bigg|_S = \frac{\chi_T}{\chi_\rho} \frac{P}{\rho T}, \quad (\text{B.20})$$

and a similar cyclic relation as above using entropy, density, and temperature, we may obtain,

$$\frac{\partial S}{\partial \ln P}\bigg|_T = \frac{\chi_T}{\chi_\rho} \frac{P}{\rho T}, \quad (\text{B.21})$$

where we have defined the following compressibilities,

$$\chi_\rho \equiv \frac{\partial \ln P}{\partial \ln \rho}\bigg|_{T, \{X_i\}}, \quad (\text{B.22})$$

$$\chi_T \equiv \frac{\partial \ln P}{\partial \ln T}\bigg|_{\rho, \{X_i\}}. \quad (\text{B.23})$$

Then by using Equations (B.15), (B.19) and (B.21) we obtain,

$$\frac{\partial \ln \rho}{\partial S}\bigg|_P \frac{dS}{d \ln P} = \frac{\chi_T}{\chi_\rho} (\nabla - \nabla_{\text{ad}}), \quad (\text{B.24})$$

which by plugging into Equation (B.12) gives us our final expression for the Brunt-Väisälä frequency,

$$N^2 = \frac{g}{\lambda_P} \left[\frac{\chi_T}{\chi_\rho} (\nabla_{\text{ad}} - \nabla) + B \right], \quad (\text{B.25})$$

where we have also defined the compositionally dependent Ledoux term,

$$B = \sum_{i=1}^{I-1} \left. \frac{\partial \ln \rho}{\partial X_i} \right|_{T, P, \{X_{j \neq i}\}} \frac{dX_i}{d \ln P}. \quad (\text{B.26})$$

B.3 Linearized Fluid Equations

We now have three fluid equations:

$$\text{Momentum} : \rho \left(\frac{\partial \vec{u}}{\partial t} + \vec{u} \cdot \nabla \vec{u} \right) = -\vec{\nabla} P - \rho \vec{\nabla} \phi, \quad (\text{B.27})$$

$$\text{Mass} : \frac{\partial \rho}{\partial t} + \vec{\nabla} \cdot (\rho \vec{u}) = 0, \quad (\text{B.28})$$

$$\text{Energy} : \frac{d\rho}{\rho} = \frac{1}{\Gamma_1} \frac{dP}{P} + \left. \frac{\partial \ln \rho}{\partial S} \right|_P dS \quad (\text{B.29})$$

Equation (B.29) has already been simplified.

We proceed in linearizing the equations by inserting:

$$\rho(\vec{x}) \rightarrow \rho_0(\vec{x}) + \delta\rho(\vec{x}, t),$$

$$P(\vec{x}) \rightarrow P_0(\vec{x}) + \delta P(\vec{x}, t),$$

$$T(\vec{x}) \rightarrow T_0(\vec{x}) + \delta T(\vec{x}, t),$$

$$\vec{u}(\vec{x}) \rightarrow \delta \vec{u}(\vec{x}, t),$$

$$\phi(\vec{x}) \rightarrow \phi_0(\vec{x}) + \delta\phi(\vec{x}, t),$$

note $\vec{u}(\vec{x})$ has no background component as we assume our star to be in hydrostatic equilibrium with no net velocity. Therefore, the linearized fluid equations are,

$$\rho_0 \frac{\partial \delta \vec{u}}{\partial t} = -\nabla \delta P - \rho_0 \nabla \delta \phi - \delta \rho \nabla \vec{\phi}_0, \quad (\text{B.30})$$

$$0 = \delta \rho + \vec{\nabla} \cdot (\rho_0 \vec{\xi}), \quad (\text{B.31})$$

$$\delta \rho = \frac{\delta P}{c_s^2} + \frac{\rho_0}{g} N^2 \xi_r,$$

note that we have used $\vec{u} = \partial \vec{\xi} / \partial t$ and have performed a time integral on the mass equation.

The ϕ field is, of course, the gravitational field. Since, the background star is assumed to be in hydrostatic equilibrium, we need only be concerned with the perturbations on the gravitational field, $\delta \phi$. As our models are absolutely spherically symmetric (we will neglect any possible spin effects), we expand in spherical harmonics the gravitational potential perturbations,

$$\delta \phi(\vec{x}, t) = \delta \phi(r, t) Y_{\ell m}(\theta, \varphi).$$

Taking the Laplacian of $\delta \phi$ we get,

$$\nabla^2 (\delta \phi(r, t) Y_{\ell m}(\theta, \varphi)) = \frac{1}{r^2} \frac{d}{dr} \left(r^2 \frac{d \delta \phi(\vec{x}, t)}{dr} \right) - \frac{\ell(\ell+1)}{r^2} \delta \phi(\vec{x}, t),$$

where we have used the eigenfunctional properties of the spherical harmonics and the Laplacian, $\nabla^2 Y_{\ell m}(\theta, \varphi) = -\ell(\ell+1) Y_{\ell m}(\theta, \varphi) / r^2$. Therefore, the gravitational field perturbation becomes, via Poisson's Equation,

$$4\pi G \delta \rho = \frac{1}{r^2} \frac{d}{dr} \left(r^2 \frac{d \delta \phi}{dr} \right) - \frac{\ell(\ell+1)}{r^2} \delta \phi. \quad (\text{B.32})$$

If we make the further assumption that all perturbations are small and in phase across all state variables, then we may assume the the perturbations separate into the form of $\delta X(\vec{x}, t) = X(\vec{x}) \exp(-i\omega t)$. Therefore, the momentum equation may be separated into two components, a radial component and an angular component with arbitrary angle (the value of which is unimportant to this discussion),

$$\text{Radial} : -\omega^2 \rho_0 \xi_r = -\frac{d\delta P}{dr} - \rho_0 \frac{d\delta\phi}{dr} - \delta\rho g, \quad (\text{B.33})$$

$$\text{Angular} : -\omega^2 \rho_0 \xi_h = -\frac{\delta P}{r} - \rho_0 \frac{\delta\phi}{r}. \quad (\text{B.34})$$

Where we have made use of the following relations,

$$\begin{aligned} \nabla\vec{\phi}_0 &= -\frac{Gm}{r^2} \hat{r} = -g\hat{r}, \\ \vec{\xi}(\vec{x}, t) &= \xi_r(r, t)Y_{\ell m}(\theta, \varphi)\hat{r} + \xi_h(r, t)r\nabla Y_{\ell m}(\theta, \varphi). \end{aligned}$$

By making the same approximations and expanding in spherical harmonics we may do the same to the mass equation. Using Equation (B.31) and working a lot of algebra with the help of Equation (B.34) and the energy equation, Equation (B.7), we obtain,

$$\frac{\delta P}{\rho_0} \left(\frac{1}{c_s^2} - \frac{\ell(\ell+1)}{\omega^2 r^2} \right) + \left(\frac{2}{r} - \frac{g}{c_s^2} \right) \xi_r + \frac{d\xi_r}{dr} - \frac{\ell(\ell+1)}{\omega^2 r^2} \delta\phi = 0$$

Finally, we may clean up the radial part of the momentum equation in a similar fashion and produce our final set of linearized fluid equations assuming

small amplitude oscillations:

$$(N^2 - \omega^2) \xi_r = -\frac{d\psi}{dr} + \frac{N^2}{g}\psi - \frac{d\delta\phi}{dr}, \quad (\text{B.35})$$

$$0 = \psi \left(\frac{1}{c_s^2} - \frac{k_h^2}{\omega^2} \right) + \frac{d\xi_r}{dr} + \xi_r \left(\frac{2}{r} - \frac{g}{c_s^2} \right) - \frac{k_h^2}{\omega^2} \delta\phi, \quad (\text{B.36})$$

$$4\pi G\rho_0 \left(\frac{\psi}{c_s^2} + \frac{N^2}{g}\xi_r \right) = \frac{1}{r^2} \frac{d}{dr} \left(r^2 \frac{d\delta\phi}{dr} \right) - k_h^2 \delta\phi, \quad (\text{B.37})$$

where ξ_r , $\delta\phi$ and $\psi = \delta P/\rho_0$ are all independent functions of r . The above equations make use of the following definitions.

$$\begin{aligned} N^2 &\equiv g \left(\frac{1}{\Gamma_1} \frac{d \ln P_0}{dr} - \frac{d \ln \rho_0}{dr} \right), \\ k_h^2 &\equiv \frac{\ell(\ell+1)}{r^2}, \\ c_s^2 &\equiv \frac{\Gamma_1 P_0}{\rho_0}, \end{aligned}$$

where N is the Brunt-Väisälä frequency and is discussed in great detail in Section B.2.1, k_h is the horizontal (perpendicular to radial) wave-number, and c_s is the adiabatic sound speed.

B.4 Boundary Conditions

At the center of the star, requiring the variables to be finite leads to the scalings $\psi \propto r^\ell$ and $\xi_r \propto r^{\ell-1}$. Placing these scalings into Equations (B.35), (B.36), and

(B.37) leads to the central boundary conditions,

$$\omega^2 \xi_r = \ell \frac{\psi + \delta\phi}{r}, \quad (\text{B.38})$$

$$\ell \frac{\delta\phi}{r} = \frac{d\delta\phi}{dr}, \quad (\text{B.39})$$

at a nonzero, but small, radius r .

At the surface, we require the perturbations to be both finite and upwardly evanescent with no pressure acting from outside the star and surface density being approximately zero. This leads to the surface scaling of $\phi \propto r^{-(\ell+1)}$ and the implication that $\vec{\nabla} \cdot \vec{\xi} \approx 0$. Placing these into Equations (B.37) and (B.36) leads to the outer boundary conditions,

$$\psi = g\xi_r, \quad (\text{B.40})$$

$$-(\ell + 1) \frac{\delta\phi}{r} = \frac{d\delta\phi}{dr}, \quad (\text{B.41})$$

at $r = R_{\text{surf}}$ of the star.

We solve Equations (B.35), (B.36), and (B.37) with the boundary conditions in Equations (B.38), (B.39), (B.40), and (B.41) using the shooting method to obtain all mode periods.

B.5 The WKB Approximation

If our modes mostly live in a region where $k_r r \ll 1$ and $k_r \lambda_P \ll 1$, then we may apply the WKB ansatz. Namely that all of our independent variables

have the same radial dependence of $\exp\left(i \int^{r'} dr k_r\right)$. This is useful as it reduces our coupled differential equations problem to an algebra problem. Further, under these conditions, $N^2 \sim g/\lambda_P$ and $c_s^2 \sim g\lambda_P$. Upon inspection of the gravity equation, Equation (B.37), with these assumptions, we obtain,

$$\begin{aligned} -(k_r^2 + k_h^2) \delta\phi &= 4\pi G\rho_0 \frac{\psi}{c_s^2}, \\ -\frac{\delta\phi}{\psi} &\sim \frac{4\pi G\rho_0}{c_s^2 k^2} \ll 1; \quad \text{For large } k. \end{aligned}$$

Therefore, we safely ignore any gravity perturbations in our WKB approximation.

Under these new approximations we simplify Equations (B.35) and (B.36) even further,

$$(N^2 - \omega^2) \xi_r \approx -ik_r \psi, \tag{B.42}$$

$$\left(\frac{1}{c_s^2} - \frac{k_h^2}{\omega^2}\right) \psi \approx -ik_r \xi_r. \tag{B.43}$$

Combining these together we produce the dispersion relation for the radial wave-number,

$$k_r^2 = \frac{(N^2 - \omega^2)(c_s^2 k_h^2 - \omega^2)}{\omega^2 c_s^2}. \tag{B.44}$$

This gives us two forms of propagating waves, p -modes, $\omega^2 > N^2$, $c_s^2 k_h^2$, and g -modes, $\omega^2 < N^2$, $c_s^2 k_h^2$.

Bibliography

Agol, E. 2002, *ApJ*, 579, 430

Agüeros, M. A., Camilo, F., Silvestri, N. M., Kleinman, S. J., Anderson, S. F., & Liebert, J. W. 2009, *ApJ*, 697, 283

Alberts, F., Savonije, G. J., & van den Heuvel, E. P. J. 1996, *Nature*, 380, 676

Allard, N. F., Kielkopf, J. F., & Loeillet, B. 2004, *A&A*, 424, 347

Althaus, L. G., & Benvenuto, O. G. 1997, *ApJ*, 477, 313

—. 1998, *MNRAS*, 296, 206

Althaus, L. G., Córscico, A. H., Gautschy, A., Han, Z., Serenelli, A. M., & Panei, J. A. 2004, *MNRAS*, 347, 125

Althaus, L. G., Serenelli, A. M., & Benvenuto, O. G. 2001, *MNRAS*, 323, 471

Arras, P., Townsley, D. M., & Bildsten, L. 2006, *ApJ*, 643, L119

Badenes, C., Mullally, F., Thompson, S. E., & Lupton, R. H. 2009, *ApJ*, 707, 971

- Baraffe, I., Chabrier, G., Allard, F., & Hauschildt, P. H. 1998, *A&A*, 337, 403
- Barklem, P. S., Piskunov, N., & O'Mara, B. J. 2000, *A&A*, 363, 1091
- Bassa, C. G., van Kerkwijk, M. H., Koester, D., & Verbunt, F. 2006a, *A&A*, 456, 295
- Bassa, C. G., van Kerkwijk, M. H., & Kulkarni, S. R. 2006b, *A&A*, 450, 295
- Bayless, A. J., & Orosz, J. A. 2006, *ApJ*, 651, 1155
- Bedin, L. R., King, I. R., Anderson, J., Piotto, G., Salaris, M., Cassisi, S., & Serenelli, A. 2008a, *ApJ*, 678, 1279
- Bedin, L. R., Salaris, M., Piotto, G., Cassisi, S., Milone, A. P., Anderson, J., & King, I. R. 2008b, *ApJ*, 679, L29
- Bedin, L. R., Salaris, M., Piotto, G., King, I. R., Anderson, J., Cassisi, S., & Momany, Y. 2005, *ApJ*, 624, L45
- Bergeron, P., Fontaine, G., Billères, M., Boudreault, S., & Green, E. M. 2004, *ApJ*, 600, 404
- Bergeron, P., Saffer, R. A., & Liebert, J. 1992, *ApJ*, 394, 228
- Bergeron, P., Wesemael, F., Lamontagne, R., Fontaine, G., Saffer, R. A., & Allard, N. F. 1995, *ApJ*, 449, 258
- Bildsten, L., & Hall, D. M. 2001, *ApJ*, 549, L219

- Bochanski, J. J., West, A. A., Hawley, S. L., & Covey, K. R. 2007, *AJ*, 133, 531
- Bradley, P. A. 1998, *ApJS*, 116, 307
- Brassard, P., & Fontaine, G. 1997, in *Astrophysics and Space Science Library*,
Vol. 214, *White dwarfs*, ed. J. Isern, M. Hernanz, & E. Garcia-Berro, 451
- Brassard, P., Fontaine, G., Wesemael, F., Kawaler, S. D., & Tassoul, M. 1991,
ApJ, 367, 601
- Brickhill, A. J. 1983, *MNRAS*, 204, 537
- . 1991, *MNRAS*, 251, 673
- Brown, J. M., Kilic, M., Brown, W. R., & Kenyon, S. J. 2011, *ArXiv e-prints*
- Brown, W. R., Geller, M. J., Kenyon, S. J., & Kurtz, M. J. 2006, *ApJ*, 647, 303
- Brown, W. R., Kilic, M., Allende Prieto, C., & Kenyon, S. J. 2010, *ApJ*, 723, 1072
- Callanan, P. J., Garnavich, P. M., & Koester, D. 1998, *MNRAS*, 298, 207
- Casewell, S. L., Dobbie, P. D., Napiwotzki, R., Burleigh, M. R., Barstow, M. A.,
& Jameson, R. F. 2009, *MNRAS*, 395, 1795
- Cassisi, S., Potekhin, A. Y., Pietrinferni, A., Catelan, M., & Salaris, M. 2007,
ApJ, 661, 1094
- Castanheira, B. G., & Kepler, S. O. 2008, *MNRAS*, 385, 430

- Castanheira, B. G. et al. 2007, *A&A*, 462, 989
- . 2006, *A&A*, 450, 227
- Catelan, M. 2000, *ApJ*, 531, 826
- Cenko, S. B. et al. 2006, *PASP*, 118, 1396
- Chabrier, G., Brassard, P., Fontaine, G., & Saumon, D. 2000, *ApJ*, 543, 216
- Chang, P., & Bildsten, L. 2003, *ApJ*, 585, 464
- Córsico, A. H., & Benvenuto, O. G. 2002, *Ap&SS*, 279, 281
- Córsico, A. H., García-Berro, E., Althaus, L. G., & Isern, J. 2004, *A&A*, 427, 923
- D’Cruz, N. L., Dorman, B., Rood, R. T., & O’Connell, R. W. 1996, *ApJ*, 466, 359
- Deeg, H. J., & Doyle, L. R. 2001, in *Third Workshop on Photometry*, ed. W. J. Borucki & L. E. Lasher, 85
- Deloye, C. J., & Bildsten, L. 2002, *ApJ*, 580, 1077
- Deloye, C. J., & Taam, R. E. 2010, *ApJ*, 719, L28
- Devor, J., Charbonneau, D., O’Donovan, F. T., Mandushev, G., & Torres, G. 2008, *AJ*, 135, 850
- Dolez, N., & Vauclair, G. 1981, *A&A*, 102, 375
- Dolez, N. et al. 2006, *A&A*, 446, 237

- Dominguez, I., Chieffi, A., Limongi, M., & Straniero, O. 1999, *ApJ*, 524, 226
- Drake, A. J. et al. 2009, *ApJ*, 696, 870
- Driebe, T., Blöcker, T., Schönberner, D., & Herwig, F. 1999, *A&A*, 350, 89
- Dziembowski, W. 1977, *Acta Astronomica*, 27, 1
- Dziembowski, W., & Koester, D. 1981, *A&A*, 97, 16
- Eggleton, P. P. 1983, *ApJ*, 268, 368
- Eisenstein, D. J. et al. 2006, *ApJS*, 167, 40
- Ferguson, J. W., Alexander, D. R., Allard, F., Barman, T., Bodnarik, J. G.,
Hauschildt, P. H., Heffner-Wong, A., & Tamanai, A. 2005, *ApJ*, 623, 585
- Finley, D. S., Koester, D., & Basri, G. 1997, *ApJ*, 488, 375
- Fontaine, G., & Brassard, P. 2008, *PASP*, 120, 1043
- Fontaine, G., Brassard, P., & Charpinet, S. 2003, *Ap&SS*, 284, 257
- Fontaine, G., Lacombe, P., McGraw, J. T., Dearborn, D. S. P., & Gustafson, J.
1982, *ApJ*, 258, 651
- García-Berro, E. et al. 2010, *Nature*, 465, 194
- Ge, H., Hjellming, M. S., Webbink, R. F., Chen, X., & Han, Z. 2010, *ApJ*, 717,
724

- Gianninas, A., Bergeron, P., & Fontaine, G. 2005, ApJ, 631, 1100
- . 2006, AJ, 132, 831
- Gianninas, A., Bergeron, P., & Fontaine, G. 2007, in Astronomical Society of the Pacific Conference Series, Vol. 372, 15th European Workshop on White Dwarfs, ed. R. Napiwotzki & M. R. Burleigh, 577
- Gilliland, R. L., & Brown, T. M. 1988, PASP, 100, 754
- Hansen, B. M. S. 2005, ApJ, 635, 522
- Hansen, C. J., Kawaler, S. D., & Trimble, V. 2004, Stellar interiors : physical principles, structure, and evolution (New York: Springer-Verlag)
- Hebb, L., Wyse, R. F. G., Gilmore, G., & Holtzman, J. 2006, AJ, 131, 555
- Heller, R., Homeier, D., Dreizler, S., & Østensen, R. 2009, A&A, 496, 191
- Hjellming, M. S., & Webbink, R. F. 1987, ApJ, 318, 794
- Hogg, D. W., Blanton, M. R., Roweis, S. T., & Johnston, K. V. 2005, ApJ, 629, 268
- Holberg, J. B., & Bergeron, P. 2006, AJ, 132, 1221
- Horne, J. H., & Baliunas, S. L. 1986, ApJ, 302, 757
- Howell, S. B. 2006, Handbook of CCD astronomy (Cambridge University Press)

- Howell, S. B., Everett, M. E., Tonry, J. L., Pickles, A., & Dain, C. 2003, *PASP*, 115, 1340
- Iben, Jr., I., & Livio, M. 1993, *PASP*, 105, 1373
- Iben, Jr., I., & Tutukov, A. V. 1984, *ApJS*, 54, 335
- Iglesias, C. A., & Rogers, F. J. 1993, *ApJ*, 412, 752
- . 1996, *ApJ*, 464, 943
- Jacoby, B. A., Bailes, M., van Kerkwijk, M. H., Ord, S., Hotan, A., Kulkarni, S. R., & Anderson, S. B. 2003, *ApJ*, 599, L99
- Jacoby, B. A., Hotan, A., Bailes, M., Ord, S., & Kulkarni, S. R. 2005, *ApJ*, 629, L113
- Kalirai, J. S., Bergeron, P., Hansen, B. M. S., Kelson, D. D., Reitzel, D. B., Rich, R. M., & Richer, H. B. 2007, *ApJ*, 671, 748
- Kanaan, A. et al. 2005, *A&A*, 432, 219
- Kaspi, V. M., Taylor, J. H., & Ryba, M. F. 1994, *ApJ*, 428, 713
- Kawaler, S. D. 1988, *ApJ*, 334, 220
- Kawka, A., & Vennes, S. 2009, *A&A*, 506, L25
- Kawka, A., Vennes, S., Oswalt, T. D., Smith, J. A., & Silvestri, N. M. 2006, *ApJ*, 643, L123

- Kepler, S. O., Castanheira, B. G., Saraiva, M. F. O., Nitta, A., Kleinman, S. J., Mullally, F., Winget, D. E., & Eisenstein, D. J. 2005a, *A&A*, 442, 629
- Kepler, S. O. et al. 2005b, *ApJ*, 634, 1311
- Kepler, S. O., Kleinman, S. J., Nitta, A., Koester, D., Castanheira, B. G., Giovannini, O., Costa, A. F. M., & Althaus, L. 2007, *MNRAS*, 375, 1315
- Kepler, S. O., Mukadam, A., Winget, D. E., Nather, R. E., Metcalfe, T. S., Reed, M. D., Kawaler, S. D., & Bradley, P. A. 2000, *ApJ*, 534, L185
- Kepler, S. O. et al. 1991, *ApJ*, 378, L45
- . 1995, *Baltic Astronomy*, 4, 221
- Kilic, M., Allende Prieto, C., Brown, W. R., Agüeros, M. A., Kenyon, S. J., & Camilo, F. 2010a, *ApJ*, 721, L158
- Kilic, M., Allende Prieto, C., Brown, W. R., & Koester, D. 2007a, *ApJ*, 660, 1451
- Kilic, M., Brown, W. R., Allende Prieto, C., Kenyon, S. J., & Panei, J. A. 2010b, *ApJ*, 716, 122
- Kilic, M., Stanek, K. Z., & Pinsonneault, M. H. 2007b, *ApJ*, 671, 761
- Kleinman, S. J. et al. 1998, *ApJ*, 495, 424
- Knigge, C. 2006, *MNRAS*, 373, 484
- Koester, D., & Chanmugam, G. 1990, *Reports on Progress in Physics*, 53, 837

- Kulkarni, S. R., & van Kerkwijk, M. H. 2010, *ApJ*, 719, 1123
- Kwee, K. K., & van Woerden, H. 1956, *Bull. Astron. Inst. Netherlands*, 12, 327
- Lee, Y., Demarque, P., & Zinn, R. 1994, *ApJ*, 423, 248
- Lewis, F., Street, R., Roche, P., Stroud, V., & Russell, D. M. 2010, *Advances in Astronomy*, 2010
- Littlefair, S. P., Dhillon, V. S., Marsh, T. R., & Gänsicke, B. T. 2006a, *MNRAS*, 371, 1435
- Littlefair, S. P., Dhillon, V. S., Marsh, T. R., Gänsicke, B. T., Baraffe, I., & Watson, C. A. 2007, *MNRAS*, 381, 827
- Littlefair, S. P., Dhillon, V. S., Marsh, T. R., Gänsicke, B. T., Southworth, J., & Watson, C. A. 2006b, *Science*, 314, 1578
- López-Morales, M., & Shaw, J. S. 2007, in *Astronomical Society of the Pacific Conference Series*, Vol. 362, *The Seventh Pacific Rim Conference on Stellar Astrophysics*, ed. Y. W. Kang, H.-W. Lee, K.-C. Leung, & K.-S. Cheng, 26
- Mandel, K., & Agol, E. 2002, *ApJ*, 580, L171
- Marsh, T. R. 2001, *MNRAS*, 324, 547
- Marsh, T. R., Dhillon, V. S., & Duck, S. R. 1995, *MNRAS*, 275, 828

- Marsh, T. R., Gaensicke, B. T., Steeghs, D., Southworth, J., Koester, D., Harris, V., & Merry, L. 2010, ArXiv e-prints
- Marsh, T. R., Nelemans, G., & Steeghs, D. 2004, MNRAS, 350, 113
- Maxted, P. F. L., O'Donoghue, D., Morales-Rueda, L., Napiwotzki, R., & Smalley, B. 2007, MNRAS, 376, 919
- Mukadam, A. S., Kepler, S. O., Winget, D. E., & Bergeron, P. 2002, ApJ, 580, 429
- Mukadam, A. S. et al. 2003, ApJ, 594, 961
- Mukadam, A. S., Montgomery, M. H., Winget, D. E., Kepler, S. O., & Clemens, J. C. 2006, ApJ, 640, 956
- Mukadam, A. S. et al. 2004a, ApJ, 607, 982
- Mukadam, A. S., Winget, D. E., von Hippel, T., Montgomery, M. H., Kepler, S. O., & Costa, A. F. M. 2004b, ApJ, 612, 1052
- Mullally, F., Badenes, C., Thompson, S. E., & Lupton, R. 2009, ApJ, 707, L51
- Mullally, F., Thompson, S. E., Castanheira, B. G., Winget, D. E., Kepler, S. O., Eisenstein, D. J., Kleinman, S. J., & Nitta, A. 2005, ApJ, 625, 966
- Nelemans, G. 2009, Classical and Quantum Gravity, 26, 094030
- Nelemans, G., & Tauris, T. M. 1998, A&A, 335, L85

- Nelemans, G., Yungelson, L. R., Portegies Zwart, S. F., & Verbunt, F. 2001, *A&A*, 365, 491
- Oswalt, T. D., Smith, J. A., Shufelt, S., Hintzen, P. M., Leggett, S. K., Liebert, J., & Sion, E. M. 1993, in *NATO ASIC Proc. 403: White Dwarfs: Advances in Observation and Theory*, ed. M. A. Barstow, 419
- Paczynski, B. 1976, in *IAU Symposium, Vol. 73, Structure and Evolution of Close Binary Systems*, ed. P. Eggleton, S. Mitton, & J. Whelan, 75
- Panei, J. A., Althaus, L. G., Chen, X., & Han, Z. 2007, *MNRAS*, 382, 779
- Papaloizou, J. C. B., Pringle, J. E., & MacDonald, J. 1982, *MNRAS*, 198, 215
- Parsons, S. G., Marsh, T. R., Copperwheat, C. M., Dhillon, V. S., Littlefair, S. P., Gänsicke, B. T., & Hickman, R. 2010, *MNRAS*, 402, 2591
- Paxton, B., Bildsten, L., Dotter, A., Herwig, F., Lesaffre, P., & Timmes, F. 2011, *ApJS*, 192, 3
- Pech, D., Vauclair, G., & Dolez, N. 2006, *A&A*, 446, 223
- Pietrinferni, A., Cassisi, S., Salaris, M., & Castelli, F. 2004, *ApJ*, 612, 168
- Provencal, J. L., Shipman, H. L., Hog, E., & Thejll, P. 1998, *ApJ*, 494, 759
- Provencal, J. L., Shipman, H. L., Koester, D., Wesemael, F., & Bergeron, P. 2002, *ApJ*, 568, 324

- Pylyser, E. H. P., & Savonije, G. J. 1989, *A&A*, 208, 52
- Pyrzas, S. et al. 2009, *MNRAS*, 394, 978
- Quirion, P., Fontaine, G., & Brassard, P. 2007, *ApJS*, 171, 219
- Rebassa-Mansergas, A., Gänsicke, B. T., Rodríguez-Gil, P., Schreiber, M. R., & Koester, D. 2007, *MNRAS*, 382, 1377
- Rebassa-Mansergas, A., Gänsicke, B. T., Schreiber, M. R., Koester, D., & Rodríguez-Gil, P. 2010, *MNRAS*, 402, 620
- Reiger, S. H. 1963, *AJ*, 68, 395
- Ribas, I. 2006, *Ap&SS*, 304, 89
- Robinson, E. L., Kepler, S. O., & Nather, R. E. 1982, *ApJ*, 259, 219
- Robinson, E. L. et al. 1995, *ApJ*, 438, 908
- Roelofs, G. H. A., Groot, P. J., Benedict, G. F., McArthur, B. E., Steeghs, D., Morales-Rueda, L., Marsh, T. R., & Nelemans, G. 2007, *ApJ*, 666, 1174
- Rogers, F. J., & Nayfonov, A. 2002, *ApJ*, 576, 1064
- Saumon, D., Chabrier, G., & van Horn, H. M. 1995, *ApJS*, 99, 713
- Scargle, J. D. 1982, *ApJ*, 263, 835
- Schmidt, H. 1996, *A&A*, 311, 852

- Schreiber, M. R., & Gänsicke, B. T. 2003, *A&A*, 406, 305
- Segretain, L., Chabrier, G., Hernanz, M., Garcia-Berro, E., Isern, J., & Mochkovitch, R. 1994, *ApJ*, 434, 641
- Serenelli, A. M., Althaus, L. G., Rohrmann, R. D., & Benvenuto, O. G. 2002, *MNRAS*, 337, 1091
- Shapiro, S. L., & Teukolsky, S. A. 1983, *Black holes, white dwarfs, and neutron stars: The physics of compact objects* (New York: Wiley-Interscience)
- Shaw, J. S., & López-Morales, M. 2007, in *Astronomical Society of the Pacific Conference Series*, Vol. 362, *The Seventh Pacific Rim Conference on Stellar Astrophysics*, ed. Y. W. Kang, H.-W. Lee, K.-C. Leung, & K.-S. Cheng, 15
- Siess, L., Forestini, M., & Dougados, C. 1997, *A&A*, 324, 556
- Silvestri, N. M. et al. 2006, *AJ*, 131, 1674
- Silvotti, R., Voss, B., Bruni, I., Koester, D., Reimers, D., Napiwotzki, R., & Homeier, D. 2005, *A&A*, 443, 195
- Sokoloski, J. L., Bildsten, L., & Ho, W. C. G. 2001, *MNRAS*, 326, 553
- Steinfadt, J. D. R., Bildsten, L., & Arras, P. 2010a, *ApJ*, 718, 441
- Steinfadt, J. D. R., Bildsten, L., & Howell, S. B. 2008a, *ApJ*, 677, L113

- Steinfadt, J. D. R., Bildsten, L., Ofek, E. O., & Kulkarni, S. R. 2008b, *PASP*, 120, 1103
- Steinfadt, J. D. R., Kaplan, D. L., Shporer, A., Bildsten, L., & Howell, S. B. 2010b, *ApJ*, 716, L146
- Taam, R. E., & Sandquist, E. L. 2000, *ARA&A*, 38, 113
- Timmes, F. X. 1999, *ApJS*, 124, 241
- Timmes, F. X., & Swesty, F. D. 2000, *ApJS*, 126, 501
- Timpano, S. E., Rubbo, L. J., & Cornish, N. J. 2006, *Phys. Rev. D*, 73, 122001
- Tremblay, P., & Bergeron, P. 2009, *ApJ*, 696, 1755
- Tremblay, P., Bergeron, P., Kalirai, J. S., & Gianninas, A. 2010, *ApJ*, 712, 1345
- Unno, W., Osaki, Y., Ando, H., Saio, H., & Shibahashi, H. 1989, *Nonradial oscillations of stars* (Tokyo: University of Tokyo Press)
- van Hamme, W. 1993, *AJ*, 106, 2096
- van Kerkwijk, M. H., Bassa, C. G., Jacoby, B. A., & Jonker, P. G. 2005, in *Astronomical Society of the Pacific Conference Series*, Vol. 328, *Binary Radio Pulsars*, ed. F. A. Rasio & I. H. Stairs, 357
- van Kerkwijk, M. H., Bergeron, P., & Kulkarni, S. R. 1996, *ApJ*, 467, L89+

- van Straten, W., Bailes, M., Britton, M., Kulkarni, S. R., Anderson, S. B., Manchester, R. N., & Sarkissian, J. 2001, *Nature*, 412, 158
- VandenBerg, D. A., Bergbusch, P. A., & Dowler, P. D. 2006, *ApJS*, 162, 375
- Vauclair, G., Dolez, N., Fu, J., Homeier, D., Roques, S., Chevreton, M., & Koester, D. 2000, *A&A*, 355, 291
- Vogt, S. S. et al. 1994, in *Society of Photo-Optical Instrumentation Engineers (SPIE) Conference Series*, Vol. 2198, *Society of Photo-Optical Instrumentation Engineers (SPIE) Conference Series*, ed. D. L. Crawford & E. R. Craine, 362
- Voss, B., Koester, D., Østensen, R., Kepler, S. O., Napiwotzki, R., Homeier, D., & Reimers, D. 2006, *A&A*, 450, 1061
- Voss, B., Koester, D., Østensen, R., Napiwotzki, R., Homeier, D., & Reimers, D. 2007, in *Astronomical Society of the Pacific Conference Series*, Vol. 372, 15th European Workshop on White Dwarfs, ed. R. Napiwotzki & M. R. Burleigh, 583
- Warner, B., & Robinson, E. L. 1972, *Nature*, 239, 2
- Webbink, R. F. 1975, *MNRAS*, 171, 555
- . 1984, *ApJ*, 277, 355
- Wesemael, F., Bergeron, P., Fontaine, G., & Lamontagne, R. 1991, in *NATO ASIC Proc. 336: White Dwarfs*, ed. G. Vauclair & E. Sion, 159

- Winget, D. E., & Kepler, S. O. 2008, ARA&A, 46, 157
- Winget, D. E., Robinson, E. L., Nather, R. D., & Fontaine, G. 1982a, ApJ, 262,
L11
- Winget, D. E., van Horn, H. M., Tassoul, M., Fontaine, G., Hansen, C. J., &
Carroll, B. W. 1982b, ApJ, 252, L65
- Wu, Y., & Goldreich, P. 1999, ApJ, 519, 783
- Yi, S., Demarque, P., Kim, Y., Lee, Y., Ree, C. H., Lejeune, T., & Barnes, S.
2001, ApJS, 136, 417
- York, D. G. et al. 2000, AJ, 120, 1579
- Young, A. T. 1967, AJ, 72, 747
- Young, T. B., Hidas, M. G., Webb, J. K., Ashley, M. C. B., Christiansen, J. L.,
Derekas, A., & Nutto, C. 2006, MNRAS, 370, 1529